



**UNIVERSITÀ DEGLI STUDI DI TORINO**

**Doctoral School in Life and Health Sciences**

**PhD Program in Complex System for Life Sciences**

**XXXIV Cycle**

**MAGNETICALLY DRIVABLE METAL CHELATORS  
LOADED NANOCARRIERS: A NEW THERAPEUTIC  
APPROACH IN NEUROLOGICAL DISORDER  
ASSOCIATED WITH TRACE METAL IMBALANCE**

**SHOEB ANWAR MOHAMMED KHAWJA ANSARI**

Supervisor: Prof. ssa Caterina Guiot

Coordinator. Prof. Enzo Medico

DEDICATED TO MY  
PARENTS

# ACKNOWLEDGEMENTS

First of all, I am thankful to Almighty Allah for giving me health and the courage to do all my activities with vigor.

On completing three emotionally charged years of my life I would like to take a journey back in time we have a close look on all milestones crossed people visited and to see if there are any footprints left on the shifting sands of time...

My stay in the Department of neuroscience and Department of Drug Science and Technology, University of Turin, and particularly this piece of work has been made possible by some 'significant others' who have influenced me and helped me throughout and chose to stay on my mind forever...

It is my pleasure to express my deep sense of gratitude to my Supervisor **Prof. ssa Caterina Guiot** Professor, Department of Neuroscience "Rita Levi Montalcini, University of Turin for the unflinching support and encouragement bestowed by her always...I feel privileged for getting an opportunity to work under her valuable guidance. Her intelligence, motivation, and active involvement in research work have not only made me understand the various aspects but have also helped me develop independent thinking. I shall be deeply and eternally indebted for the advice and guidance she gave me during the part of my research work.

It is a genuine please to express my deep sense of thanks to my mentor, philosopher, and guide **Prof. ssa Roberta Cavalli**, Professor, Department of Drug Science and Technology, University of Turin. Her dedication and keen interest above all her overwhelming attitude to help her student had been solely and mainly responsible for completing my work. Her timely advice, meticulous scrutiny, scholarly advice, scientific advice, and scientific approach have helped me to a very great extent to accomplish this task.

I owe a deep sense of gratitude to **Prof. ssa Ornella Abollino**, Department of Drug Science and Technology, University of Turin for her keen interest in me at every stage of research. Her prompt inspiration, timely suggestions with kindness, enthusiasm, and dynamism have enabled me to complete my thesis.

Also, I am thankful to Coordinator **Prof. Enzo Medico** and **Prof. Michele Debortoli**, for ensuring smooth working conditions.

I would also like to express my deep gratitude towards **Rita Spagnolo** for providing chemicals and invaluable technical support for carrying out my current dissertation.

I extend my sincere word of thanks to **Monica Argenziano, Federico D'Agata** who has always been there, more as a friend than a senior. I would never be able to pay back the love and affection showered upon by them. The work done with them as a Junior has taught me how a person can succeed in achieving what seems impossible, to begin with. Thank you, Monica and Federico, for everything.

My acknowledgment will never be complete without the special mention of my collaborators who have taught me the new lab techniques and have lived by example to make me understand the hard facts of life. I would like to acknowledge **Prof. Franca Albertini, Prof. Lucia Nasi** (Consiglio Nazionale delle Ricerche, Istituto dei Materiali per l'Elettronica ed il Magnetismo, Parma, Italy), **Silvia Gazzin and Sri Jayanti** (Fondazione Italiana Fegato Onlus, Trieste Italy).

I would like to acknowledge my labmates, **Federica Bessone, Silvia Appleton, Davide Rossi, Zunaira Munir, Irfan Ansari, Johanna Rodriguez, and Andrea Valperga** for always being there and bearing with me the good and bad times during my wonderful days of Ph.D.

My special thanks to my colleague, **Eleonora Ficiarà** you should know that your support and encouragement were worth more than I can express on paper.

It is my privilege to thank my wife, **Ayesha Siddiqua** who has stood by me through all my travails, for her love and constant support, for all the late nights and early mornings, and for keeping me sane over the past few months. She gave me support and help, discussed ideas, and prevented several wrong turns.

Finally, I would like to acknowledge the people who mean the world to me, my parents, my brothers, and sisters. I don't imagine a life without their love and blessings. Thank you, Mummy, Papa, for showing faith in me and giving me the liberty to choose what I desired. I consider myself the luckiest in the world to have such a supportive family, standing behind me with their love and support.

Thank you....

Ansari Shoeb Anwar

## **Declaration**

I hereby declare that except where specific reference is made to the work of others, the contents of this dissertation are original and have not been submitted in whole or in part for consideration for any other degree or qualification in this, or any other university. This dissertation is my work and contains nothing which is the outcome of work done in collaboration with others, except as specified in the text and Acknowledgements. This dissertation contains fewer than 50000 words including appendices, bibliography, footnotes, tables, and equations, and has fewer than 275 figures.

**Shoeb Anwar Ansari**

**January 2022**

## Abstract

Human health is severely hampered by many neurological disorders such as brain tumors, degenerative Alzheimer's disease (AD), Parkinson's disease (PD), and those involving inflammatory components. The brain is the central organ of the body and it is protected by multiple barriers such as the blood-cerebrospinal fluid (CSF) barrier and blood-brain barrier (BBB). The challenge for effective therapy is to cross the BBB and extensive research has been carried out in the field of nanotechnology e.g., nanoparticles (NPs) and nanobubbles. Due to their specific physical and chemical properties, magnetic nanovectors are the ideal agent for drug delivery to the CNS. Disturbed iron homeostasis and mitochondrial dysfunction play important roles in the development of a large number of neurodegenerative diseases. Although the etiology of Alzheimer's disease is still largely unknown, oxidative damage mediated by metals is a likely significant contributor since metals such as iron, aluminum, zinc, and copper are dysregulated and/or increased in AD brain tissue and create a pro-oxidative environment. This role of metal ion-induced free radical formation in AD makes chelation therapy an attractive approach for dampening the oxidative stress burden in neurons. In recent years, growing evidence indicates that iron accumulation in the brain plays an important role in AD onset and progression and therefore, iron-chelation agents have been suggested as a new potential drug able to counteract the neuronal deterioration in AD. Their systemic administration, however, critically reduces their effectiveness in the brain's intracellular fluid. Here, we propose a novel system of chelation therapy through the use of nanocarriers conjugated to chelators, which show a unique ability to cross the blood-brain barrier (BBB), to chelate metals, and to escape across the BBB with their corresponding complexed metal ions. This method may provide a safer and more effective means of reducing the metal load in neural tissue, thus attenuating the harmful effects of oxidative damage and its sequelae. We prepared and characterized the physicochemical properties and cytotoxicity of Magnetic oxygen-loaded nanobubbles functionalizing by different polymers shells such as Chitosan, Dextran Sulphate, Glycol-chitosan-EDTA and Glycol-chitosan Deferoxamine, and perfluoropentane-cored nanobubbles with superparamagnetic iron oxide nanoparticles. Magnetic oxygen-loaded nanobubbles with sizes of about 380 nm were manufactured, able to store oxygen and

chelate excess iron. Their toxicity was evaluated on organotypic brain cultures (substantia nigra). Finally, the possibility of magnetic driving by static external magnetic fields was investigated on physical models using ultrasound.

# Index

<b>List of Figures.....</b>	<b>1</b>
<b>List of Tables.....</b>	<b>5</b>
<b>Chapter 1: Introduction.....</b>	<b>6</b>
<b>1.1. Introduction .....</b>	<b>7</b>
<b>1.1.1. Neurodegenerative disorder .....</b>	<b>7</b>
<b>1.1.2. What are the causes of neurodegenerative disease? .....</b>	<b>7</b>
<b>1.1.3. Type of neurodegenerative disorder .....</b>	<b>8</b>
<b>1.1.3.1. Alzheimer’s.....</b>	<b>8</b>
<b>1.1.3.1.1. Epidemiology.....</b>	<b>8</b>
<b>1.1.3.1.2. Etiology.....</b>	<b>9</b>
<b>1.1.3.1.3. Pathophysiology.....</b>	<b>9</b>
<b>1.1.3.1.4. Diagnosis .....</b>	<b>9</b>
<b>1.1.3.2. Treatment (Drug therapy) .....</b>	<b>10</b>
<b>1.1.3.3. Parkinson’s Disease .....</b>	<b>10</b>
<b>1.1.3.3.1. Epidemiology.....</b>	<b>10</b>
<b>1.1.3.3.2. Etiology.....</b>	<b>11</b>
<b>1.1.3.3.3. Diagnosis .....</b>	<b>11</b>
<b>1.1.3.3.4. Treatment.....</b>	<b>11</b>
<b>1.1.4. Iron and neurodegenerative disorder .....</b>	<b>13</b>
<b>1.1.4.1. Iron deficiency in the brain.....</b>	<b>13</b>
<b>1.1.4.2. Excess brain iron .....</b>	<b>14</b>
<b>1.1.4.3. Neurodegenerative mechanisms involving iron .....</b>	<b>15</b>
<b>1.1.4.4. Iron and Alzheimer’s Disease .....</b>	<b>15</b>
<b>1.1.4.5. Iron and Parkinson’s disease .....</b>	<b>16</b>
<b>1.1.4.6. Iron Toxicity.....</b>	<b>17</b>
<b>1.1.5. Iron chelation: a novel approach to reduce iron burden .....</b>	<b>18</b>
<b>1.1.5.1. Chelating agents.....</b>	<b>18</b>
<b>1.1.5.1.1. Desferoxamine, Deferasirox and Deferiprone.....</b>	<b>18</b>
<b>1.1.5.1.2. Clioquinol .....</b>	<b>20</b>
<b>1.1.6. Nanomedicine for a neurological disorder .....</b>	<b>20</b>
<b>1.1.7. Blood-brain barriers.....</b>	<b>20</b>
<b>1.1.8. Nanotechnology for brain drug delivery .....</b>	<b>21</b>
<b>1.1.8.1. Characteristics of NPs for drug delivery to the brain .....</b>	<b>21</b>



1.1.8.2.	Nano systems for drug delivery to the brain .....	22
1.1.8.2.	Polymeric nanoparticles .....	23
1.1.8.3.	Liposome .....	25
1.1.8.4.	Dendrimers.....	25
1.1.8.5.	Magnetic nanoparticles .....	26
1.1.8.5.1.	Magnetic nanoparticles design .....	26
1.1.8.5.2.	Chemical design .....	26
1.1.8.5.3.	Synthesis of magnetic nanoparticle .....	27
1.1.8.5.4.	Design workflow for magnetic nanoparticles.....	27
1.1.8.5.5.	Application of magnetic nanoparticles .....	28
1.1.8.6.	Nanobubbles .....	28
1.1.8.7.	Magnetic oxygen loaded nanobubbles (MOLNBs) .....	29
1.1.9.	Polymers.....	30
1.1.9.1.	Natural polysaccharides .....	30
1.1.9.1.2.	Chitosan.....	31
1.1.9.1.2.1.	Physico-chemical properties of chitosan .....	32
1.1.9.1.2.2.	Production of chitosan.....	32
1.1.9.1.2.3.	Degree of deacetylation .....	32
1.1.9.1.2.4.	Crystallography .....	32
1.1.9.1.2.5.	Molecular weight .....	33
1.1.9.1.2.6.	Solubility.....	33
1.1.9.1.2.7.	Viscosity and Colour.....	33
1.1.9.1.2.8.	Pharmaceutical applications .....	33
1.1.9.1.3.	Glycol Chitosan .....	34
1.1.9.1.4.	Dextran sulfate Sodium salt .....	34
1.1.9.1.3.1.	Characteristics.....	35
1.1.9.1.3.2.	Pharmaceutical Application.....	35

## **Chapter 2: Magnetic Iron Oxide Nanoparticles: Synthesis, Characterization and Functionalization for Biomedical Applications in the Central Nervous System ..... 36**

2.1.	Introduction .....	37
2.2.	Synthesis of IONPs .....	38
2.2.1.	Co-precipitation method .....	38
2.2.2.	Thermal decomposition method.....	39
2.2.3.	Microemulsion method .....	40

2.2.4.	Hydrothermal method.....	40
2.2.5.	Polyol method.....	41
2.2.6.	Sol-gel method.....	41
2.3.	Characterization of IONPs .....	43
2.3.1.	Microscopic Techniques .....	43
2.3.2.	Spectroscopic Techniques.....	43
2.4.	Application to CNS .....	45
2.5.	Functionalization of IONPs for CNS applications.....	46
2.5.1.	Ligand addition .....	47
2.5.2.	Ligand exchange.....	47
2.5.3.	Silica coating.....	47
2.5.4.	Aminosilane coating .....	48
2.5.5.	Polymer coating .....	48
2.6.	Application to CNS .....	50
2.7.	Conclusions and Future Perspectives.....	50

## **Chapter 3: Superparamagnetic Oxygen-Loaded Nanobubbles to Enhance Tumor Oxygenation During Hyperthermia ..... 52**

3.1.	Introduction .....	53
3.2.	Materials and Methods .....	54
3.2.1.	Materials .....	54
3.2.2.	Synthesis of SPIONs .....	55
3.2.3.	Preparation of MOLNB formulations .....	55
3.2.4.	Physicochemical Characterization of NB Formulations.....	56
3.2.5.	Determination of NB Physical Stability Over Time.....	56
3.2.6.	Ultrasound Imaging Evaluation .....	56
3.2.7.	Hyperthermic and Magnetic Measurements.....	57
3.2.8.	<i>In Vitro</i> Oxygen Release Studies.....	57
3.2.9.	Cell Internalization.....	58
3.2.10.	Statistical Analysis .....	58
3.4.	Results .....	58
3.4.1.	Physicochemical Characterization of NB Formulations.....	58
3.4.2.	Ultrasound Imaging Evaluation .....	60
3.4.3.	Hyperthermic and Magnetic Measurements.....	61
3.4.5.	<i>In Vitro</i> Oxygen Release.....	62
3.4.6.	Cell Internalization.....	63

3.5.	Discussion.....	64
3.6.	Conclusions .....	66
<b>Chapter 4: Beyond Oncological Hyperthermia: Physically Drivable Magnetic Nanobubbles as Novel Multipurpose Theranostic Carriers in the Central Nervous System ..... 67</b>		
4.1.	Introduction .....	68
4.1.	Materials and Methods .....	69
4.1.1.	Materials .....	69
4.1.2.	Methods .....	69
4.1.2.1.	Synthesis of SPIONs .....	69
4.1.2.2.	Preparation of MOLNBs Formulations .....	70
4.1.2.3.	Physicochemical Characterization of MOLNBs .....	70
4.1.2.4.	Physical Stability of MOLNBs.....	71
4.1.2.5.	Determination of Haemolytic Activity .....	71
4.1.2.6.	Evaluation of MOLNBs Internalization by Human Brain Microvascular Endothelial Cells.....	71
4.1.2.7.	In Vitro Cytotoxicity Study.....	72
4.1.2.8.	US Imaging Monitoring.....	72
4.2.	Results .....	73
4.2.1.	Physicochemical Characterization of MOLNBs Formulations .....	73
4.2.2.	Haemolytic Activity.....	74
4.2.3.	Evaluation of MOLNBs Internalization and Toxicity .....	74
4.2.4.	US Monitoring of MOLNBs in the Magnetic Field.....	76
4.5.	Discussion.....	77
4.6.	Conclusions .....	79
<b>Chapter 5: Step-by-Step Design of New Theranostic Nanoformulations: Multifunctional Nanovectors for Radio-Chemo-Hyperthermic Therapy under Physical Targeting..... 80</b>		
5.1.	Introduction .....	81
5.1.1.	Loading and Delivery of Oxygen to Hypoxic Tissues .....	81
5.1.2.	Loading and Delivery of Anticancer Drugs .....	82
5.1.3.	Magnetic Physical Targeting and Hyperthermia.....	83
5.2.	Materials and Methods .....	83
5.2.1.	Materials .....	83
5.2.2.	Methods .....	84

5.2.2.1.	Preparation of Chitosan Oxygen-Carrying Nanobubbles .....	84
5.2.2.2.	Dextran and Dextran sulfate oxygen loaded nanodroplets .....	84
5.2.2.3.	Synthesis of SPIONs .....	84
5.2.2.4.	Preparation of MOLNB Formulations.....	85
5.2.2.5.	In Vitro Oxygen Release Study .....	85
5.2.2.6.	Physicochemical Characterization of OLNBS, OLNDs, and MOLNBs .....	86
5.2.2.7.	Morphological Evaluation.....	86
5.2.2.8.	Magnetic Measurements and Hyperthermic Properties.....	86
5.2.2.9.	Evaluation of Antitumor Effect of Doxorubicin and Curcumin-Loaded OLNDs.....	87
5.2.2.10.	Curcumin Release during HT.....	87
5.2.2.11.	MRI Testing .....	87
5.2.2.12.	Magnetic Field and US Imaging Monitoring.....	88
5.3.	Results .....	88
5.3.1.	Oxygen- Loaded Nanosystems: Loading and Delivery of Oxygen to Hypoxic Tissues .....	88
5.3.2.	Drug-Loaded Oxygen-Loaded Nanosystems: Loading and Delivery of Anticancer Drugs .....	90
5.3.3.	SPION-decorated OLNBS: Manufacturing and Physicochemical characterization of MOLNBs .....	92
5.3.4.	Magnetic Characterization of MOLNBs.....	94
5.3.5.	Magnetic and Hyperthermic Properties of MOLNBs .....	95
5.3.6.	Drivability by the Application of Weak Static Magnetic Fields of MOLNBs.....	97
5.4.	Discussion.....	97

## **Chapter 6: Magnetically drivable metal chelators loaded Nanocarriers: A new therapeutic approach in neurological disorder associated with trace metal imbalance. .... 101**

6.1.	Introduction .....	102
6.1.1.	Polymeric nanobubbles for Iron chelation .....	103
6.1.2.	Bilirubin loaded GC-DFO nanobubbles.....	105
6.2.	Materials and Methods .....	105
6.2.1.	Materials .....	105
6.2.2.	Methods .....	106
6.2.2.1.	Synthesis of Glycol Chitosan-Deferoxamines derivative.....	106
6.2.2.2.	Synthesis of Glycol chitosan-EDTA Conjugation .....	106
6.2.2.3.	Synthesis of superparamagnetic iron oxide nanoparticles .....	106
6.2.2.4.	Preparation of nanobubbles with different polymer shells for iron chelation.....	107

6.2.2.5.	Superparamagnetic iron oxide nanoparticles loaded Nanobubbles (MNBs)	107
6.2.2.6.	Bilirubin loaded Glycol chitosan Deferoxamine nanobubbles	107
6.2.2.7.	Structural characterization of the synthesized derivative of Glycol-Chitosan+ Deferoxamine	107
6.2.2.8.	Physicochemical analysis	108
6.2.2.9.	Iron chelation Studies	108
6.2.2.9.1.	Ferrozine assay	109
6.2.2.9.2.	Deferoxamine assay	109
6.2.2.10.	Haemolytic activity	109
6.2.2.11.	Evaluation of antioxidant activity	110
6.2.2.12.	Quantitative determination of Bilirubin by HPLC method	110
6.2.2.13.	In Vitro Cytotoxicity Study	110
6.3.	Results	111
6.3.1.	Structural characterization of the synthesized derivative of Glycol-Chitosan+ Deferoxamine	111
6.3.1.2.	Structure conformation of GC-DFO from NMR	111
6.3.2.	Physicochemical Characterization of Formulations	112
6.3.3.	Iron Chelation	113
6.3.4.	Hemolytic Activity	114
6.3.5.	Antioxidant activity	115
6.3.6.	Quantitative determination of Bilirubin by HPLC method	115
6.3.7.	In-vitro cytotoxicity	116
6.4.	Discussion	116
6.5.	Conclusion	117
<b>Chapter 7: Conclusions</b>		<b>118</b>
7.1.	Conclusion	119
7.2.	What's next	121
8.	References	122

## List of Figures

Figure.no	Title of figure
1.1	A hypothesis to explain neurodegenerative disease
1.2	Iron deposits in the aging brain
1.3	Characteristic of NPs for drug delivery to the brain
1.4	The type of NPs
1.5	Possible modification and functionalization of magnetic particles
1.6	Sketch of MOLNBs
1.7	Chemical structure of Chitosan
1.8	Structure of Dextran Sulphate
2.1	A comparison among the prevalence of the main methods currently existing for the synthesis of IONPs, with the detailed chemical methods prevalence
2.2	Flowchart for the synthesis of IONPs by co-precipitation
2.3	Flowchart for the synthesis of IONPs by microemulsion
2.4	Flowchart for the synthesis of IONPs by polyol method
2.5	Flowchart for the synthesis of IONPs by sol-gel method
2.6	Flowchart of classification of organic and inorganic materials used for the functionalization of IONPs
2.7	Surface modification of IONPs by ligand addition
3.1	Sketch of MOLNB structure [dextran NBs covered by Fe <sub>3</sub> O <sub>4</sub> nanoparticles]
3.2	Experimental setup used for US imaging
3.3	<b>(A)</b> HRTEM image of SPIONs; <b>(B, C)</b> TEM images of blank-shelled OLNBs at different magnifications
3.4	<b>(A)</b> TEM image of an MOLNB; <b>(B)</b> HRTEM image of the square region in <b>(A)</b> ; <b>(C)</b> HRTEM image of the square region in <b>(A)</b> showing the (311) lattice planes of a Fe <sub>3</sub> O <sub>4</sub> nanoparticle

- 3.5 Snapshots of the B-mode cineloops of control experiment (demineralized water only), OLNBs, and MOLNBs at MI = 1.1 (i.e., maximum acoustic power) and different temperatures. Red arrows indicate the focus of the US probe
- 3.6 Variation of temperature as a function of time under exposure of RF magnetic field for two different AC field amplitudes
- 3.7 RT magnetization curve for MOLNBs
- 3.8 In vitro oxygen release from MOLNBs at different temperatures (i.e., 25°C, 37°C, and 41°C)
- 3.9 OLNb internalization by TUBO cell line. Cell nuclei after DAPI staining (in blue; OLNb, in green). Magnification ×63
- 4.1 Sketch of MOLNBs (dextran NB covered with Fe<sub>3</sub>O<sub>4</sub> nanoparticles, not to scale) and relative multifunctional applications as theranostic system in CNS
- 4.2 **(a)** A sketch of the setup used for the imaging of MOLNBs in absence and presence of the magnetic field produced by the cuboid magnet. **(b)** Projection of magnetic field lines in the XZ plane assessed by the z-direction of the magnetic field
- 4.3 **(a)** TEM images of MOLNBs at different magnification. **(b)** TEM images of SPIONs
- 4.4 Confocal images of different formulations of nanocarriers internalized by hBMECs after 4 h of incubation
- 4.5 Percentage of viable cells after 72 h of incubation. The horizontal axis indicates the dilution (1:100 and 1:200) of NB. Red = MOLNBs; Green = SPIONs; Blue = OLNb
- 4.6 Snapshots from US imaging of MOLNBs in the absence **(a)** and presence **(b)** of the magnetic field. Images were recorded at different time frames (5, 15, 25, 55 sec) from the injection
- 5.1 Structure of the oxygen-loaded nanosystem
- 5.2 TEM **(a)**, optical fluorescence **(b)**, and US **(c)** imaging of OLNb
- 5.3 Examples of passive oxygen release in fluids: **(a)** oxygen concentration in different liquids, saline, and Perfadex, in normoxic and hypoxic bulk at 4° C; **(b)** Sketch of the device for measuring oxygen diffusion from the donor compartment to the bathing medium. Data are measured with an accuracy of ± 1.5% of the nominal value
- 5.4 DOX in OLND promotes synergistic antitumor effects. Cell viability was evaluated by MTT assay. Data are expressed as percentage vs control. TUBO cells were left untreated or incubated for 48 h with DOX (0.005

$\mu\text{M}$ ), OLNDs (2.5% v/v), or DOX-loaded OLNDs (0.005  $\mu\text{M}$ /2.5% v/v). Results are shown as means  $\pm$  SD from three independent experiments. Significance of the differences: \*  $p < 0.05$ ; \*\*  $p < 0.005$ ; \*\*\*  $p < 0.001$

- 5.5 Percentage of inhibition of viability: **(a)** PC-3 tumor cells; **(b)** DU-145 tumor cells
- 5.6 Physicochemical characteristics of nanocarrier formulations: **(a)** average diameter (nm); **(b)** polydispersity index; **(c)**  $\zeta$  potential (mV) for OLNBs (blue), SPIONs (red) and MOLNBs (green)
- 5.7 Illustration of MOLNBs (negatively charged dextran shell NBs decorated with positively charged SPIONs by electrostatic interaction)
- 5.8 HAADF-STEM images of the MOLNBs decorated with SPIONs taken at different magnifications (**(a)** = 500 nm, **(b)** = 200 nm, **(c)** = 20 nm).
- 5.9 Oxygen release study performed by passive diffusion in saline solution at different temperatures over 24 h. Data of oxygen concentration were measured with an accuracy of  $\pm 1.5\%$  of the nominal value
- 5.10 **(a)** Signal intensities of blank OLNBs at different TE value and **(b)** signal intensity of 0.5, 1, 2.0 and 2.5 mg/mL. SPIONs concentration on MOLNBs at different TE values as a function of echo delay time.  $T_2$  is inversely proportional to the concentration of SPIONs loaded on MOLNBs, increased concentration shows a sharp reduction in the signal intensity. The error bars show SD
- 5.11 **(a)** Magnetization cycle of SPIONs; **(b)** Magnetization cycle of MOLNBs. In the insets, a zoom of the measurements is reported, highlighting the superparamagnetic behavior of the samples (i.e., absence of magnetic hysteresis and remanence)
- 5.12 Magnetic hyperthermia measurements under an alternating ( $f = 429$  kHz) magnetic field of 300 Oe for 30 min: temperature increase as a function of time of the curcumin-loaded dextran MOLNBs at different concentrations of SPIONs (1 mg/mL and 0.5 mg/mL)
- 5.13 US imaging snapshot of MOLNBs in the absence **(a)** and the presence **(b)** of the magnetic field generated by two magnets (distance 4 cm from each other). Images were recorded at different time frames (5, 15, 30 s) from the injection
- 6.1 Bilirubin loaded magnetic oxygen loaded nanobubbles
- 6.2 FTIR Spectra of GC, DFO, and Gc-DFO
- 6.3  $^1\text{H}$  NMR Spectra of GC-DFO
- 6.4 Structure of GC-DFO



- 6.5 Standard plot for  $\text{Fe}^{+2}$
- 6.6 Standard plot for  $\text{Fe}^{+3}$
- 6.7 Antioxidant activity
- 6.8 Viability of cell after 24 hours treatment, MTT, LDH, and DOPAn count

## List of Tables

<b>Table.no</b>	<b>Title of table</b>
1.1	Pharmacological therapies for Parkinson's disease
2.1	IONP synthesis techniques and comparison with respect to their different parameters
2.2	Different characterization techniques used to assess the physicochemical properties of IONPs
2.3	Polymers used for functionalized IONPs in biomedical applications
3.1	Physicochemical characteristics of NB formulations
4.1	Physicochemical characteristics of different nanocarriers formulations. Data reported as Mean $\pm$ Standard Deviation
5.1	Different oxygen-loaded nanosystems. OLNb: oxygen-loaded nanobubbles; OLND: oxygen loaded nanodroplets
5.2	T2 signal values obtained from curve fitting
6.1	Principal IR peaks for GC-DFO
6.2	Physicochemical characteristics of different nanocarriers formulations. Data reported as Mean $\pm$ Standard Deviation
6.3	UV absorbance for Fe <sup>+2</sup>
6.4	UV absorbance for Fe <sup>+3</sup>
6.5	Iron chelation
6.6	Iron Chelation with different iron concentration
6.7	Bilirubin concentration

## Chapter 1: Introduction

## 1.1. Introduction

### 1.1.1. Neurodegenerative disorder

Neurodegenerative disorders are a serious hazard to people's health. These age-related illnesses are becoming more common, because of the increasing elderly population in recent years<sup>1</sup>. Neurons are small units of the nervous system because neurons do not ordinarily multiply or replenish themselves, they cannot be replaced by the body when they are injured or die. Neurodegenerative diseases are incurable and devastating illnesses that cause nerve cells to degenerate and/or die over time. This affects a person's ability to move, speak, and breathe and creates problems with movement (ataxias) and mental functioning (dementias). In 2019, around 50 million people worldwide were living with a neurodegenerative disease that commonly resulted in dementia, with that figure anticipated to climb to 152 million by 2060<sup>2</sup>. The overall prevalence of neurodegenerative illness leading to dementia is 1.6% and 1% for males and females, respectively, in the 65-69 age group, rising to 11% and 12.6% in the 85-89 age group, according to the European dementia meta-analysis (EURDEM) of all European research<sup>3</sup>.

#### 1.1.2. What are the causes of neurodegenerative disease?

The pathophysiology of the neurodegenerative disorder is built around seven main propositions: 1) neurodegenerative disease is associated with multiple risk factors, 2) age is the most important of the risk factors, 3) aging differentially affects neuroanatomical pathways, 4) degeneration of these pathways results in the formation of pathogenic proteins, 5) pathogenic proteins spread along anatomical pathways, 6) the phenotypes of familial and sporadic forms of the disease are similar and 7) neurodegenerative disease is characterized by heterogeneity, overlapping phenotypes, and multiple pathology<sup>4</sup>.

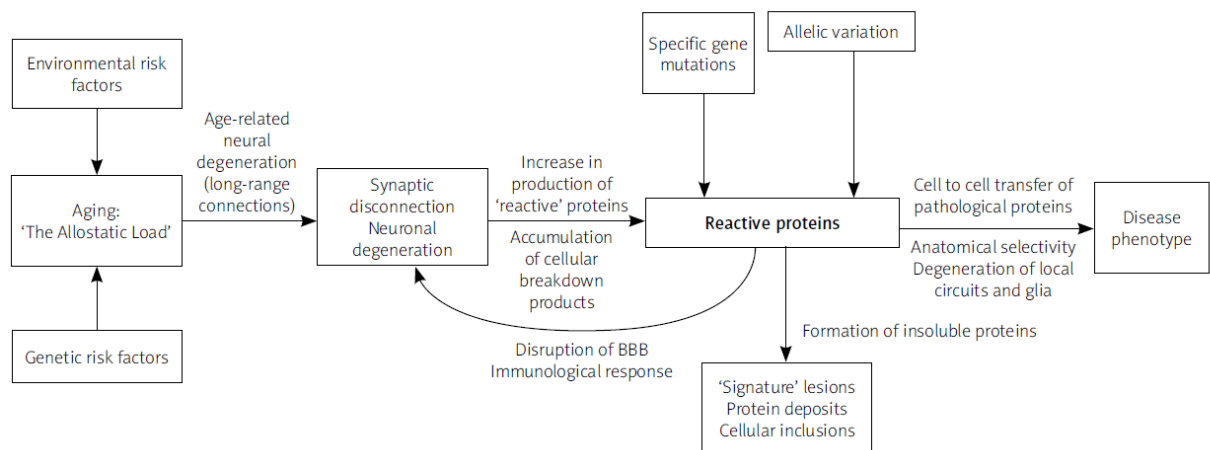


**Figure 1.1:** A hypothesis to explain neurodegenerative disease

### 1.1.3. Type of neurodegenerative disorder

#### 1.1.3.1. Alzheimer's

Alzheimer's disease (AD) is the most common neurological cause of dementia, accounting for an estimated 60% to 80% of cases, with high individual morbidity and death, as well as a significant financial burden on the healthcare system. Extra neuronal toxic amyloid oligomers and proteins, intraneuronal neurofibrillary tangles composed of hyperphosphorylated tau, region-specific diminished cerebral glucose metabolism, synaptic dysfunction, and mitochondrial dysfunction are all linked to neurodegeneration (including neuronal atrophy and/or loss)<sup>5</sup>. Alzheimer's disease was discovered more than a century ago, but it took another 70 years for it to be recognized as the most frequent cause of dementia and a leading cause of death<sup>6</sup>. The World Health Organization has designated AD as a global public health priority. Despite significant advances in our understanding of AD pathophysiology and how we think about the disease since Alois Alzheimer reported the first case in 1907, no disease-modifying medications exist<sup>7</sup>.

##### 1.1.3.1.1. Epidemiology

According to current estimates, 44 million individuals worldwide suffer from dementia. As the population ages, this is expected to more than triple by 2050, Dementia is the top cause of death in England and Wales, accounting for 11.6 percent of deaths recorded in 2015. Recent studies imply that the incidence of dementia in Western countries is

dropping, particularly in men; however, it is unclear which causes of dementia are declining, and this could be attributed to better vascular risk management<sup>7</sup>.

#### 1.1.3.1.2. Etiology

In the development of Alzheimer's disease, both hereditary and environmental risk factors play a role. The most significant risk factor is one's age. At 65, the chance of developing Alzheimer's disease is roughly 3%, rising to almost 30% by 85. The incidence of Alzheimer's disease among people under the age of 65 is unknown, however, estimates imply that this age group accounts for about 3% of all cases. Early-onset Alzheimer's disease (EOAD) develops before the age of 65, whereas late-onset Alzheimer's disease (LOAD) manifests after the age of 65 and accounts for almost 95 %<sup>8</sup>

#### 1.1.3.1.3. Pathophysiology

Many theories have been presented to explain the pathophysiology of Alzheimer's disease (AD), which is marked by neurodegeneration, neuronal loss, and atrophy, especially in the temporal and parietal lobes of the brain. Extraneuronal toxic amyloid oligomers and proteins, intraneuronal neurofibrillary tangles composed of hyperphosphorylated tau, region-specific decreased cerebral glucose metabolism, synaptic dysfunction, and mitochondrial dysfunction are the pathological hallmarks of Alzheimer's disease. Several concepts have been proposed in recent years to explain the aberrant processes that lead to the deposition of pathologic forms of amyloid and tau. Importantly, the concept of pure AD may be more theoretical than reality in older age groups. Dementia that appears later in life is more likely to be caused by a combination of age-related brain alterations, the most prevalent of which are vascular abnormalities, Alzheimer's pathology, and  $\alpha$ -synuclein pathology<sup>5</sup>.

#### 1.1.3.1.4. Diagnosis

Neuropsychological testing is currently used to diagnose Alzheimer's disease. Neuroimaging and monitoring of established biomarkers, such as A $\beta$ peptide concentrations (A $\beta$ 1–42: A $\beta$ 1–40 ratio) and total and hyperphosphorylated  $\tau$  (Thr181 and Thr231) proteins in the CSF, are required for a clinical diagnosis of AD. Although 18F-florbetapir (or alternatively 11C Pittsburgh compound B) positron emission tomography (PET) can be used to image amyloid oligomers and plaque accumulation, the nonlinear

relationship between A $\beta$  concentration in CSF and PET scans remains a source of concern<sup>9</sup>. Another noninvasive method for detecting functional abnormalities is magnetic resonance imaging (MRI) with increasing field strength and resolution. To make detection and identification of amyloid plaques more efficient, MRI is used with iron oxide nanoparticles as contrast agents or linked with fluorescent probes<sup>10</sup>.

#### 1.1.3.2. Treatment (Drug therapy)

However, much of the research on Alzheimer's disease over the last decade has focused on disease-modifying therapies that alter the course of the disease rather than treating symptoms alone. Due to a dearth of effective disease-modifying medications these studies show the difficulties that come with producing a new product. A drug that has the potential to change the course of a disease an illness as complex as Alzheimer's<sup>11</sup>

#### 1.1.3.3. Parkinson's Disease

Parkinson's disease is the second most prevalent progressive neurodegenerative ailment affecting older persons in the United States, and its incidence is expected to rise as the population of the country ages. Idiopathic Parkinson's Disease is caused by a pathophysiologic loss or degeneration of dopaminergic neurons in the substantia nigra of the midbrain and the development of neuronal Lewy Bodies. It is linked to risk factors such as aging, family history, pesticide exposure, and environmental chemicals (e.g., synthetic heroin use). Its underlying causes are unclear. Rest tremor, stiffness, bradykinesia, and other motors and non-motor symptoms are common in people with Parkinson's disease. Neurobehavioral problems (depression, anxiety), cognitive impairment (dementia), and autonomic dysfunction are all linked to Parkinson's disease (e.g., orthostasis and hyperhidrosis). In recent decades, both pharmacologic therapy and novel surgical techniques such as deep brain stimulation (DBS) have proliferated<sup>12</sup>.

Parkinson's Disease has been known since the early 1800s when the disease was originally characterized by the physician who bears his name.

##### 1.1.3.3.1. Epidemiology

Parkinson's disease, people of all ethnic backgrounds can be impacted, with men being slightly more susceptible. In one study, the annual incidence of Parkinson's disease was estimated to be around 13 cases per 100,000 people. The average age of onset of this

disorder was formerly predicted to be in the late 50, but it is now believed to be in the early to mid-60s. The first symptom of young-onset Parkinson's disease might appear between the ages of 21 and 40 (occasionally 50), whereas the first symptom of juvenile-onset Parkinson's disease appears before the age of 20<sup>13</sup>.

#### 1.1.3.3.2. Etiology

PD is a complex illness that involves both hereditary and environmental variables. The most important risk factor for Parkinson's disease is age, with the median age of onset being 60 years old. The disease's incidence climbs with age, reaching 93.1 (per 100,000 person-years) in those aged 70 to 79. There are also cross-cultural differences, with higher prevalence observed in Europe, North America, and South America when compared to Africa, Asia, and other countries.

#### 1.1.3.3.3. Diagnosis

Parkinson's disease is not considered a single disease entity, and the term has different meanings for different physicians and researchers. Some people use the term as a clinical diagnosis and accept a variety of pathological substrates as the cause of the illness. Others will reserve the name for idiopathic parkinsonism with Lewy body inclusions in nigra cells and other brain cells<sup>14,15</sup>. Although a diagnosis of Parkinson's disease, as defined above, can be a simple clinical exercise in patients with typical presentations of cardinal signs and excellent response to levodopa treatment, differentiating Parkinson's disease from other forms of parkinsonism can be difficult, especially early in the disease when signs and symptoms of different forms of parkinsonism are more similar. Even though the majority of the patients in these trials had been treated by movement disorder specialists, error rates in clinicopathological series have been as high as 24%<sup>16</sup>.

#### 1.1.3.3.4. Treatment

Medical therapies are the cornerstone of PD treatment. Pharmacotherapy and nonpharmacological alternatives like exercise, education, support groups, speech treatment, and diet are among them. Treatment options are determined by the patient's age, illness stage, troublesome symptoms, and treatment benefit/risk ratios. Since the number of possibilities for PD medication has grown significantly.



**Table 1.1:** Pharmacological therapies for Parkinson's disease<sup>17</sup>

<b>Group</b>	<b>Name of drug</b>	<b>Mechanism of action</b>
Dopamine	Carbidopa/Levodopa (Sinemet)	A dopamine precursor; crosses the blood-brain barrier (BBB) and is converted to dopamine in dopaminergic terminals by dopa-decarboxylase
Dopamine Agonists Non-Ergot	Pramipexole (Mirapex) Ropinirole (Requip)	Stimulates D2, D3, D4 Receptors; weak stimulation of 5-HT2 and Alpha 2 – adrenergic receptors
Dopamine Agonists Ergot	Bromocriptine (Parlodel) Pergolide	Stimulates D2 receptors Stimulates 5HT1 and 5HT2 and NA Receptors Blockades D1 Receptors
Injectable Dopamine Agonists	Apomorphine (Apokyn)	Stimulates D2-D5 receptors Antagonizes 5HT1 and 5HT2 receptors Antagonizes Alpha-1 and Alpha-2 adrenergic receptors
Monoamine Oxidase-B Inhibitors	Selegiline (Eldepryl) Rasagiline (Azilect)	Selective Irreversible inhibition of MAO-B. Inhibition of presynaptic dopamine receptors and dopamine uptake
CatecholO–Methyltransferase (COMT) Inhibitors	Entacapone (Comtan) Tolcapone (Tasmar)	Reversible inhibition of COMT
N-Methyl-D-Aspartate (NMDA) Receptor Inhibitor	Amantadine	Increase synthesis and release of dopamine; blocks NMDA Glutamatergic receptors
Anticholinergics	Benzotropine Trihexyphenidyl	Blockade of muscarinic cholinergic receptors and possible inhibition of cholinergic transmission in striatal interneurons

#### 1.1.4. Iron and neurodegenerative disorder

Iron is the most important element in the body since practically all cell types, including brain cells, require it. Iron deficiency and excess have been linked to the development of a variety of brain diseases. Iron deficiency has been linked to both brain development and the pathophysiology of restless legs syndrome. Iron accumulation has been associated with some neurologic illnesses, including Alzheimer's disease, Parkinson's disease, type I neurodegeneration with brain iron accumulation, and others. Women have less than 4 grams of total body iron than men. The majority of iron is heme iron, which is found in hemoglobin, myoglobin, and iron-containing enzymes (such as catalase and the cytochromes). The balance of total body iron is made up of nonheme iron, which comprises plasma iron, iron connected to transferrin, and iron stored in ferritin and hemosiderin.<sup>18</sup>

As people age, iron deposits in numerous regions of the brain may impair normal cognitive function and behavior. Abnormal iron metabolism generates hydroxyl radicals, damages cell lipids, protein, and DNA structure and function, and eventually leads to cell death by inducing oxidative stress events. There is an imbalance in iron homeostasis in Alzheimer's disease (AD). Excess iron promotes the deposition of  $\beta$ -amyloid and the formation of neurofibrillary tangles, which accelerates the progression of Alzheimer's disease. As a result, iron-targeted therapeutic techniques have emerged as an innovative treatment option. Desferrioxamine, deferiprone, deferasirox, and clioquinol are iron chelators that have received a lot of attention and positive results in scientific study and clinical studies<sup>19</sup>.

##### 1.1.4.1. Iron deficiency in the brain

Iron deficiency has been linked to impaired brain function in newborns and young children, resulting in cognitive and learning difficulties<sup>20,21</sup>. Brain-related problems with iron insufficiency, the severity, and the duration of iron shortage are key markers. Iron and transferrin insufficiency have been postulated as possible causes of degeneration in the C1 and C2 sections of the hippocampus. Unfortunately, iron supplementation is not beneficial, particularly when the iron deficit occurs during a critical period of brain development and neural differentiation (when changes are irreversible). Some of the behavioral and developmental changes observed in human infants could be explained by

changes in neurotransmitters such as noradrenaline, serotonin, and dopamine during an iron deficiency<sup>22</sup>.

#### 1.1.4.2. Excess brain iron

In the typical aging brain, iron accumulates, and in higher amounts in older people's brains. In the context of many neurologic disorders<sup>23</sup>. Hemochromatosis, for example, causes an excess of extracellular iron. Serum transferrin's iron-carrying capacity grows. The increased iron-carrying capacity of transferrin and increased rate of iron transportation across the blood-brain barrier result in the accumulation of iron in the brain cells<sup>24</sup>.

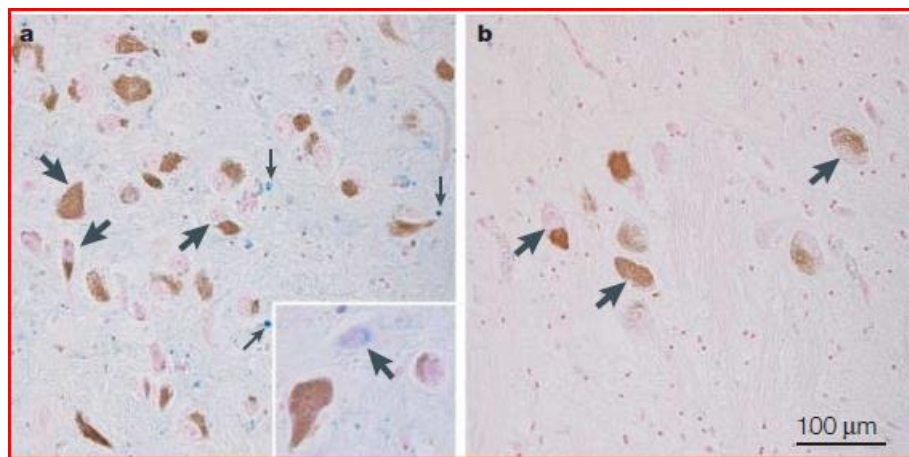


**Figure 1.2:** Iron deposits in the aging brain<sup>25</sup>. Iron histochemistry with modified Perls' staining of human substantia nigra (**a**) and locus coeruleus (**b**) from a normal male subject aged 88. Neuromelanin in dopaminergic neurons of the substantia nigra and noradrenaline neurons of the locus coeruleus is seen as brown granules, and iron deposits are stained blue. Neuromelanin-containing neurons in both the substantia nigra (large arrows in **a**) and locus coeruleus (large arrows in **b**) do not stain blue for iron. In the substantia nigra, there are many iron-positive cells, most of which are oligodendrocytes with cytoplasmic iron deposits (small arrows), and in the locus coeruleus, there are very few oligodendrocytes with light iron staining. Iron deposits are also present in the cytoplasm of non-pigmented neurons of the substantia nigra, as shown at higher magnification in the inset in panel **a** (arrow). Iron deposits can be observed in the whole substantia nigra parenchyma, except pigmented neurons, but are completely absent in locus coeruleus parenchyma.

#### 1.1.4.3. Neurodegenerative mechanisms involving iron

To avoid harmful effects, iron deposition in brain cells must be strictly controlled. By producing reactive oxygen species (ROS), such as the hydroxyl radical, excess iron can cause oxidative stress. ROS can oxidize proteins and damage DNA and mtDNA. They can also influence DNA expression through epigenetic processes. Peroxidation of polyunsaturated fatty acids in membrane lipids by reactive oxygen species (ROS) can produce highly reactive aldehydes as 4-hydroxynonenal, which carbonylated proteins irreversibly. ROS can cause the release of iron from the respiratory chain mitochondrial iron-sulfur cluster proteins and other iron storage proteins, resulting in further ROS formation via Fenton's reaction. Iron homeostasis disruption can interfere with mitochondrial processes, accelerating the progression of neurodegenerative mechanisms<sup>26,27</sup>. Increased iron levels can trigger neurodegenerative processes via mechanisms other than Fenton's reaction. Catecholamines, such as dopamine, can be oxidized to extremely reactive or poisonous quinones by ferric iron reduction or enzymatically. 1-methyl-4-phenyl-1,2,3,6-tetrahydropyridine (a neurotoxin known to cause Parkinson's disease-like symptoms) has been demonstrated to be converted into the hazardous metabolite 1-methyl-4-phenylpyridinium ion by ferric iron. Furthermore, iron and alterations in iron metabolism are likely to be involved in the neurodegenerative pathways that lead to cell death caused by the 1-methyl-4-phenylpyridinium ion<sup>28</sup>.

#### 1.1.4.4. Iron and Alzheimer's Disease

Iron's biological activity is primarily determined by its efficient electron transfer capabilities, which allow it to take or donate electrons throughout the transition between divalent ferric, and trivalent iron forms, allowing it to function as a catalytic cofactor in a wide range of metabolic reactions. When iron is in the form of iron-sulfur clusters, it increases the activity of various biological enzymes involved in DNA replication and repair (Fe-S). Iron is found in hemoglobin and myoglobin, which are important in the transport of oxygen and carbon dioxide in living organisms.<sup>29</sup>.

Iron is significantly complexed with ferritin and concentrated in amyloid plaque-associated neurotic processes in Alzheimer's disease. The effects of iron on amyloid precursor protein (APP) processing via  $\beta$ -secretase, amyloid deposition, and oxidative stress may have a direct effect on plaque development. The finding of an iron-responsive

region in the APP mRNA could help to solidify the link between iron metabolism and Alzheimer's disease. Specific iron-management protein mutations, such as HFE1 mutations (related to congenital hemochromatosis) or transferrin subtype C2 mutations, may increase the risk of Alzheimer's disease<sup>30</sup>.

Amyloid- ( $A\beta$ ) plaques in the brain, which are generated by the breakdown of amyloid precursor protein (APP), are the hallmark pathologic features of Alzheimer's disease. The deposition of fibrillar aggregates of  $A\beta$  in the brain parenchyma, which is caused by  $A\beta$  overproduction, poor clearance, or both, is thought to be the etiology of AD. By lowering iron, high quantities of iron may interact with the  $A\beta$  peptide, resulting in the reduction of molecular oxygen to superoxide and then to  $H_2O_2$ . Overexpression of the carboxyl terminus portion of APP ( $A\beta$ ) has also been shown to drastically reduce copper and iron levels in the transgenic mouse brain. This shows that APP and  $A\beta$  play a role in physiologic metal regulation in Alzheimer's disease.

Iron's role in the etiology of Alzheimer's disease is assumed to be linked to increased oxidative stress caused by free iron. Neurodegeneration has also been linked to transferrin, ferritin, and iron regulatory protein in Alzheimer's disease. The latter could be to blame for the disruption in brain iron homeostasis and total decompartmentalization of iron, as well as the oxidative processes that occur, which are symptomatic of Alzheimer's disease<sup>31</sup>.

#### 1.1.4.5. Iron and Parkinson's disease

Parkinson's disease is characterized by iron buildup in dopaminergic neurons of the substantia nigra. Free cytosolic iron can produce oxidative stress and increase  $\alpha$ -synuclein aggregation, leading to the formation of Lewy bodies. Neuromelanin may have neuroprotective qualities in the early stages of PD because it lowers free iron accumulation and, as a result, hydroxyl radical generation and the creation of neurotoxic dopamine quinones. In advanced phases, however, extravasation of neuromelanin granules from dying neurons may attract and activate microglia, resulting in the release of neurotoxic chemicals and cell destruction. Iron chelation and overexpression of iron-sequestering ferritin both have been demonstrated to be protective in animal models<sup>30</sup>.

Some authors have documented an increase in total iron concentration in the substantia nigra in the most severe instances of PD, but no changes in milder cases. Other studies

have observed no increase in total iron concentration in the substantia nigra of PD patients, most likely due to methodological challenges and the patients' varying stages of the disease. The lateral globus pallidus had a higher iron concentration than the medial globus pallidus, which could imply retrograde dopaminergic neuron loss in Parkinson's disease. There is a significant inverse relationship between dopamine and iron concentrations in the putamen of patients with PD, but not in the substantia nigra, supporting the concept of a retrograde degenerative process.

In living individuals with PD, MRI can detect an increased brain iron concentration that correlates with post-mortem tissue measurements. Transcranial sonography, a newly developed technology that allows two-dimensional viewing of the brain parenchyma via an intact skull, reveals an increased intensity region of echogenicity in the substantia nigra of individuals with Parkinson's disease, which is related to iron content<sup>32</sup>.

#### 1.1.4.6. Iron Toxicity

Iron overload's impact on the brain is poorly understood. According to the Fenton reaction, the most important process is the creation of free radicals:



ROS, such as the hydroxyl radical OH, which is produced when iron reacts with hydrogen peroxide, are normally removed by reduced glutathione or superoxide dismutase; however, in high enough concentrations, they can attack structural proteins, lipids, RNA, and DNA, causing severe oxidative damage and apoptosis. The inner mitochondrial membrane, whose penetration signals the point of no return for programmed cell death, plays a vital function in apoptosis signalling<sup>33</sup>.

ROS can cause apoptosis through a complex mitochondria-to-nucleus signaling cascade oxidation of hippocampus potassium channels, and disruption of normal myelin production, in addition to their direct effects on the cell. While there are various theories about how iron causes neurodegeneration, the mechanism is currently being investigated<sup>34</sup>.

### 1.1.5. Iron chelation: a novel approach to reduce iron burden

Iron chelators have attracted a lot of attention for their possible therapeutic value in eliminating excess iron from certain brain regions afflicted by neurodegenerative disorders. To be effective, an iron chelator must be able to penetrate both cellular membranes and the blood-brain barrier, target the region of iron accumulation without depleting transferrin-bound iron in the plasma, and remove chelatable iron from the site of accumulation or transfer it to other biological proteins like circulating transferrin<sup>35</sup>. Because the majority of patients with neurodegenerative illnesses have normal systemic iron homeostasis, the chelator must be given in very small doses to avoid side effects. Furthermore, it is unknown whether iron chelators can remove iron from conjugated iron-containing proteins and molecules like neuromelanin; the current chelators were designed to remove iron from ferritin and haemosiderin in grossly iron-overloaded tissues like the liver and spleen and to a lesser extent the heart. Although the type and molecular distribution (e.g., cluster size and oxidation state) of iron may affect the quantitative accuracy of MRI, it is a promising approach for assessing therapy efficacy<sup>36/28</sup>.

To effectively exert chelation, a metal chelator must have the following characteristics: (1) passes through cell membranes and the blood-brain barrier (BBB); (2) targets iron-rich areas without depleting transferrin-bound iron in plasma; (3) removes chelated iron from iron accumulation sites or transfers it to other biological proteins, such as circulating transferrin; and (4) has no or minor side effects on the body<sup>29</sup>.

#### 1.1.5.1. Chelating agents

A chelating agent which has all the quality as indicated above to bind the excess iron is as follows.

##### 1.1.5.1.1. Desferoxamine, Deferasirox and Deferiprone

Desferrioxamine (DFO) is a well-established iron chelator that decreases the toxicity of iron and aluminum, as well as the reactive oxygen species (ROS) that they generate in the body. DFO was once thought to be a chelating agent for aluminum ions, and aluminum was thought to be a separate risk factor for Alzheimer's disease. Crapper McLachlan et al. (1991) discovered that intramuscular injections of DFO decreased the degree of loss in daily living abilities in Alzheimer's disease patients compared to placebo-treated Alzheimer's patients. In vitro, DFO has been found to inhibit the formation of A $\beta$ 1-42 $\beta$  -

sheets and disintegrate pre-existing plaque-like amyloid plaques. DFO has also been shown in experiments to inhibit the translation of APP mRNA, the expression of APP complete protein, and the release of A $\beta$  peptides<sup>37</sup>.

Although DFO has demonstrated promising in a variety of experimental animal models and has been approved by the FDA for the treatment of iron overload sickness, there are several difficulties with its clinical application. DFO has a limited bioavailability due to its molecular size and hydrophilicity, which prevents it from freely crossing the BBB, limiting its availability in the central nervous system; second, DFO cannot be taken orally and must be supplied through injection. A single injection can take up to ten hours, and injections are administered often (5–7 times per week), resulting in low patient compliance<sup>38</sup>.

Deferasirox is the first FDA-approved oral iron repellent that can be used daily. A typical treatment for thalassemia iron overload is 4-[3,5-bis(2-hydroxyphenyl)-1,2,4-tris Oxazol-1-yl] benzoic acid. Deferasirox has a limited ability to bind iron. This drug can only bind a little amount of iron and distribute it to extracellular and intracellular iron receptors. Iron deficiency is difficult to produce, and the effectiveness of decreasing iron buildup is also restricted. According to current studies, deferasirox appears to play a role in reducing brain iron buildup. Deferasirox, on the other hand, has been shown to not affect brain iron buildup or toxicity in several studies. This could be due to deferasirox's low ability to bind iron and difficulty passing through the BBB. Because each molecule of deferasirox is required to bind one molecule of iron, higher doses are required<sup>29</sup>.

Deferiprone's chemical name is 3-hydroxyl,2-dimethyl-4-(1H)-pyridone. Deferiprone is approved for the treatment of thalassemia iron excess in patients, just like deferasirox. Deferiprone can bind almost all of the iron in the body, preventing it from producing additional ROS generation, as well as delivering the bound iron to iron receptors both inside and outside the cell. Deferiprone has a high iron-binding capacity, therefore it only requires two molecules to bind one molecule of iron, effectively minimizing iron aggregation<sup>38</sup>. DFO, deferasirox, and deferiprone are currently suggested as first-line iron chelators for iron overload<sup>39</sup>.



#### 1.1.5.1.2. Clioquinol

Clioquinol (CQ) is a metal chelating agent (iron, copper, and zinc) having the chemical formula 5-chloro-7-iodo-8-hydroxyquinoline. CQ treatment of animal models of Alzheimer's disease has been proven to reduce amyloid buildup in the brain and improve memory impairment. This occurrence is hypothesized to be caused by CQ's great binding affinity for iron, zinc, and copper ions, which allows it to compete with A $\beta$  for these metals, preventing A $\beta$  from aggregating<sup>29</sup>.

#### 1.1.6. Nanomedicine for a neurological disorder

Academics and drug designers are quickly adopting new nanotechnology to improve medicine transport to the central nervous system (CNS). Nanotechnology has the potential to change the way neurological disorders are treated, including Alzheimer's disease, Parkinson's disease, brain tumors, and stroke. In the case of neurodegeneration, multiple studies have shown that nanomaterials can be employed to treat CNS illnesses successfully. In this field, nanocarriers have aided in the targeted delivery of chemotherapeutics, resulting in efficient disease progression inhibition in malignant brain tumors. Drug diffusion over the blood-brain barrier (BBB) is the most important stage in the treatment of neurological disorders. The safe, appropriate, and targeted delivery of pharmaceutical molecules to the CNS is an ideal goal for achieving optimal therapeutic outcomes in neurological diseases<sup>40</sup>. The BBB membrane protects the human brain, which is the most sensitive and sophisticated organ in the body. This barrier is perfect for protecting brain neurons from the potentially harmful and poisonous compounds found in the blood. The BBB is a barrier that separates the circulation from the brain. There are around 100 billion neurons in the human brain. The capillaries in the brain can be as small as 7–10micron in diameter<sup>41</sup>. The BBB is devoid of intracellular and valvar gaps, limiting the transfer of information from the environment to the brain<sup>42</sup>.

#### 1.1.7. Blood-brain barriers

The BBB (blood-brain barrier) is a special structure in neurons that separates the extracellular fluid from blood circulation. In his research in 1885, Paul Ehrlich provided the first proof for the occurrence of BBB. The BBB serves as a barrier between blood circulation and the fluid inside the CNS, preventing nerve cells from being damaged by foreign substances and pathogens that enter through the blood. Furthermore, the BBB

prohibits water-soluble compounds, proteins, peptides, genes, and antibiotics with molecular weights greater than 500 Da from reaching the brain, even though NPs with such molecular weights can pass through it due to their aspect ratio and spatial geometry. This unique barrier is made up of various cell types. The BBB's 3D structure includes endothelial cells, pericytes, astrocytes, and microglia<sup>43,44</sup>.

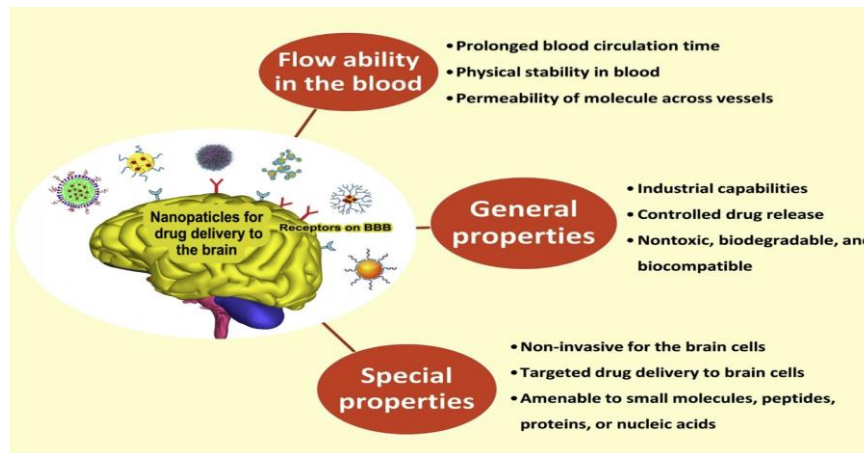
Pharmaceutical molecules may not be able to reach the brain when circulating in the blood due to the presence of the BBB, which inhibits entry into the brain and protects it from infections and hazardous substances. The barrier prevents even small chemicals from entering the brain. Many essential compounds can cross over this barrier, however therapeutic drugs are typically excluded due to their particular properties. The inability of drugs to pass across the BBB stresses the significance of developing NPs-based drug delivery strategies. The NPs break down the tight connections between endothelial cells in the vessel, allowing the drug to get over the BBB<sup>45</sup>.

#### 1.1.8. Nanotechnology for brain drug delivery

The challenge is to cross the BBB to solve the unmet need, extensive research has been carried out in the field of nanotechnology e.g., nanoparticles (NPs). NPs and MNPs are in the range of 1 to 100 nm that work as a whole unit in terms of transport and properties.

##### 1.1.8.1. Characteristics of NPs for drug delivery to the brain

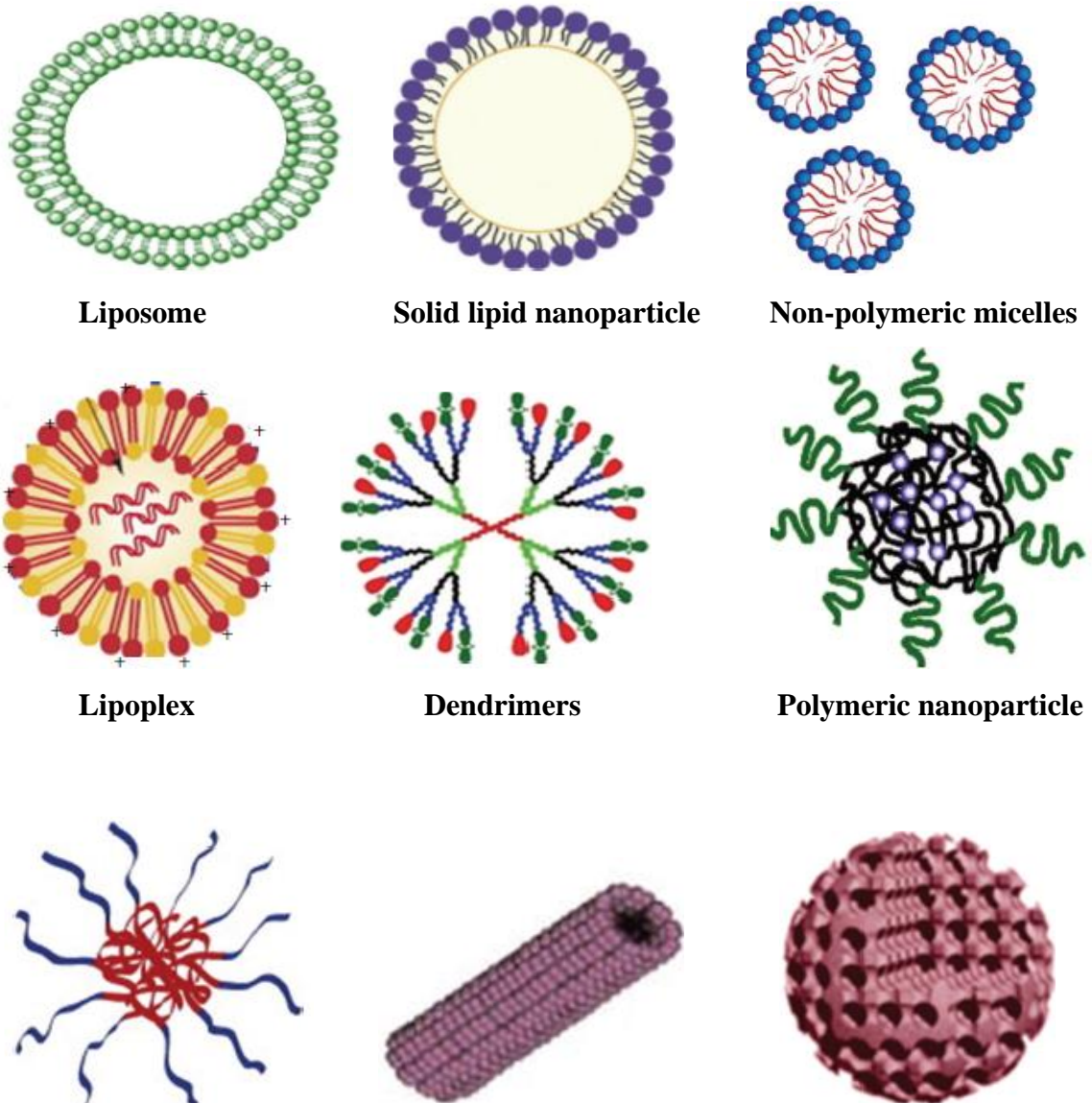
The passive passage is possible for molecules with high lipophilicity and small size. Lipophilicity is intimately linked to the permeability and solubility of a chemical. Lipophilicity, on the other hand, is a double-edged sword. Lipophilicity has an impact on some medication characteristics. High lipophilicity can result in molecules with a fast metabolism, low solubility, and poor absorption. Nanotechnology can be utilized to deliver drugs in certain situations. To be employed for medication delivery to the CNS, NPs, and nanostructures must have particular features<sup>46,47</sup>.



**Figure 1.3:** Characteristic of NPs for drug delivery to the brain<sup>45</sup>

### 1.1.8.2. Nano systems for drug delivery to the brain

Different type of nanosystems is listed below which are used for drug delivery to the brain.



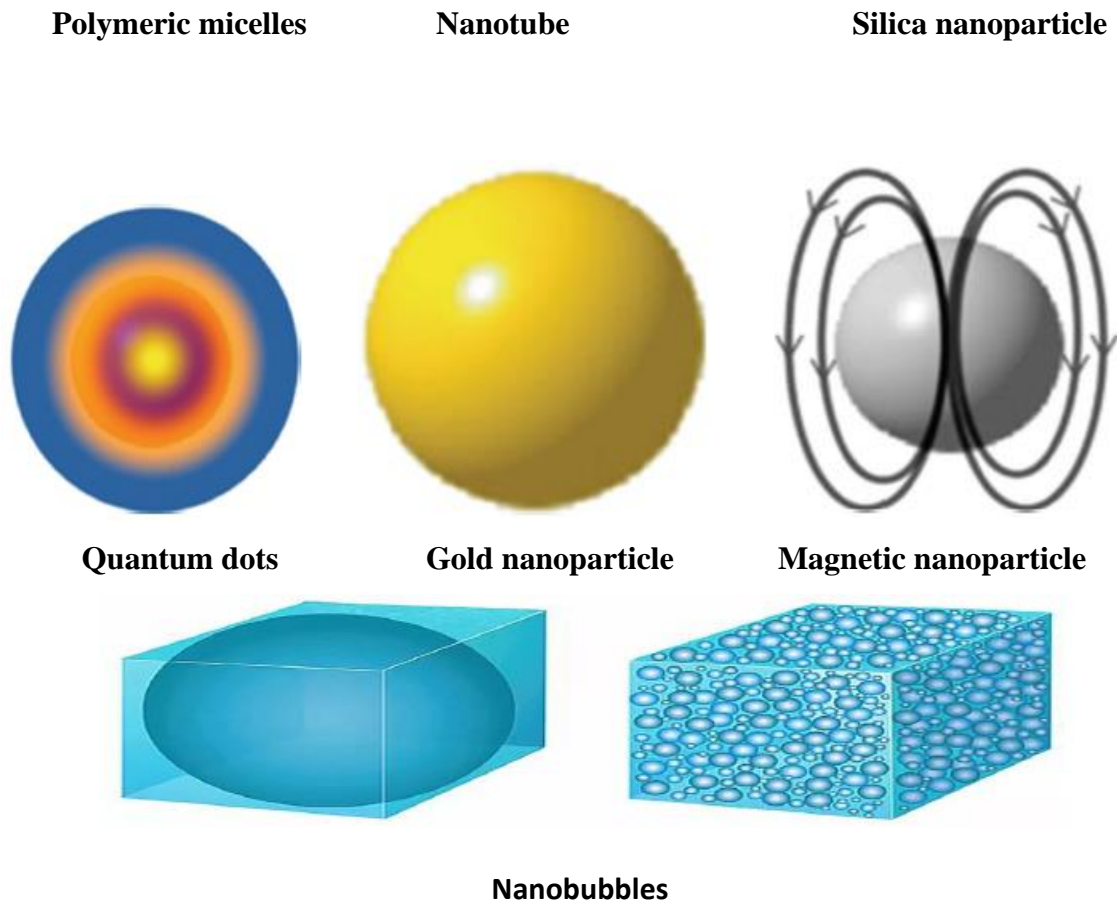


**Figure 1.4:** The type of NPs

#### 1.1.8.2. Polymeric nanoparticles

Advances in polymeric nanomaterials engineering and their applications in nanomedicine are enabling novel tactics that have the potential to improve our knowledge and treatment of brain disorders. Nanomedicine has progressed to an astounding point, with the potential to undertake targeted delivery with temporal and spatial control, based on unique polymeric materials. For many pharmaceutical companies, developing unique and effective tactics for treating brain illnesses is one of the most difficult and costly market positions. For example, the price of getting a novel medicine to phase I clinical trials might be as high as \$100 million and as high as \$1 billion before it reaches the customer<sup>48</sup>. Unfortunately, although a vast number of free medications (e.g., chemotherapeutic agents, peptides, proteins, and genes) have been published in an attempt to tackle brain diseases, a large percentage of those drugs be unsuccessful in vivo. Poor biological fluid stability, fast enzymatic breakdown, insufficient release, and adverse pharmacokinetic qualities could be the main reasons for clinical efficacy failure<sup>49</sup>. Nanomaterials are rapidly

being developed to protect and transport medications, both small molecules, and biomacromolecules, which are ineffective on their own, to overcome these obstacles.

Adsorption, dissolution, encapsulation, and covalent coupling of drugs with polymeric nanoparticles are all common<sup>50</sup>. These polymeric nanoparticles can benefit nanomedicine. (1) improved solubility of poorly water-soluble (hydrophobic) medications, (2) prolonged drug half-life by lowering immunogenicity, (3) transcytosis across strong epithelial and endothelial barriers (e.g., blood-brain barrier), (4) intracellular delivery and (5) tissue targeting (6) regulated release of pharmaceuticals encapsulated in nanoparticles at a steady rate or in response to a specific environment, (7) co-delivery of two or more therapeutic agents for combination therapy, and (8) high visibility and precision with imaging modalities.

The potential of polymeric nanoparticles to carry a variety of medications, as well as their easy surface modification, makes them an appealing choice for drug transport over the BBB. The majority of polymeric nanoparticles that show some efficacy for drug administration across the BBB in vivo follow the principles outlined below. The perfect polymeric nanoparticle will have all of the following characteristics<sup>51</sup>:

- Biocompatible, nontoxic, and biodegradable
- Particle size less than 100 nm (unless transported by monocytes or macrophages, in which case vesicle size can be up to 1  $\mu$ m)
- Blood stability (limited aggregation and dissociation)
- Longer blood circulation time and non-immunogenic (doesn't get absorbed by immune cells)
- Parent drug stability (chemical degradation and protein denaturation) is well-maintained
- Tunable drug release profiles
- BBB-targeted moiety (receptor- or adsorptive-mediated mechanism or absorption by monocytes or macrophages)
- A process that is both scalable and cost-effective

### 1.1.8.3. Liposome

Many research has focused on the use of liposomes with polyethylene glycol-modified surfaces (PEG), which lowers their plasma opsonization. Drug encapsulation in lipid NPs prolongs drug dispersion in the bloodstream, decreases medication side effects, and increases CNS disease therapeutic benefits. Because of these characteristics, lipid NPs are particularly useful for delivering medications to the CNS. Liposomes are swiftly absorbed in the CNS by macrophages, microglia, and steroids, and can be adsorbed to the cell surface in a specific or non-specific manner, releasing their contents into the cytoplasm.

### 1.1.8.4. Dendrimers

Dendrimers are three-dimensional molecules with a complex structure that contains an initial core, multiple internal layers, repeating units, and various active surface groups at the end. As the number of dendrimer generations (represented by G) increases, so does the number of dendrimer branches and surface groups<sup>52</sup>. Dendrimers have a reputation for high performance and low dispersion. The generated polyamidoamine (PAMAM) dendrimer nanocarriers are appropriate for CNS medication delivery. The mechanism of noncarriers is as follows<sup>45</sup>:

Stage 1: dendrimers are changed with distance or surface linkages to increase biocompatibility, storage capacity, drug release rate, and kinetics.

Stage 2: special ligands are attached to dendrimers that have been superficially changed to target the BBB or tumor and improve drug delivery through it.

Stage 3: Drugs and genes are delivered via modified dendrimers, which form complex biological junctions.

Stage IV: Imaging agents can be covalently bound to dendritic nanocarriers, making it impossible to track their biological dispersion. As a result, they employ imaging and in vivo diagnostic methods.

It should be mentioned that depending on the circumstances, phases 2 and 3 can be adjusted.

#### 1.1.8.5. Magnetic nanoparticles

Magnetic nanoparticles are a type of NP that can be manipulated by applying magnetic fields to them. MNPs are made up of two parts: a magnetic material such as iron, nickel, or cobalt, and a functional chemical component. Magnetic particles and magnetic composites are used as medication carriers, contrast agents for magnetic resonance imaging (MRI), and in magnetic hyperthermia due to the diverse features of MNPs in the biomedical area<sup>53</sup>. The nanoparticles demonstrate potential transport possibilities to the brain, despite the various ways used to breach BBB. There is a lot of interest in the utilization of MNPs because of their physical and chemical properties. Magnetoporation is the capacity of MNPs to create temporary gaps in cell membranes, as in the case of the BBB endothelium, to increase targeting and distribution.

##### 1.1.8.5.1. Magnetic nanoparticles design

The synthesis of MNPs is extremely important, and various parameters should be considered at each step of the process. These variables can have a substantial impact on the desired outcome and can be optimized during the early stages of design. Particle qualities, both physical and chemical, can be tweaked to suit a variety of purposes. Magnetic nanoparticles are used in nanomedicine in general, and notably in cancer treatment<sup>54</sup>. Magnetic nanoparticles or magnetic composites are appealing for drug delivery because they allow for magnetic field modification<sup>55</sup>. This opens up the possibility of customizing the medication release profile. The physical and chemical design of MNPs will be examined in light of the breadth of chemical design.

##### 1.1.8.5.2. Chemical design

For magnetic particle functionalization, two primary techniques have been reported. The first includes using biomaterials like antibodies and oligonucleotides to modify the inorganic materials, while the second combines them with other nanocomponents like quantum dots. The key problem in approaches such as magnetic particle hyperthermia is to have a homogeneous dispersion of nanoparticles and consequently a well-controlled temperature increase in tumor tissue. This can be accomplished by using antibody-conjugated magnetic nanoparticles to target tumors.<sup>56</sup>

### 1.1.8.5.3. Synthesis of magnetic nanoparticle

Materials commonly utilized in the manufacture of MNPs are categorized into compounds (usually oxides) of iron, cobalt, nickel, and other elements combining several metals<sup>57</sup>. Materials based on copper, zinc, strontium, and barium are among the combination materials. Metallic nanoparticles and nanoalloys are also classified as magnetic nanoparticles. The methods for synthesis MNPs are listed below<sup>58</sup>.

- Chemical synthesis
  - a. Co-precipitation
  - b. Thermal decomposition
  - c. Microemulsion
  - d. Hydrothermal
- Microwave-assisted synthesis
- Template assisted fabrication
- Assembly of magnetic nanostructures
- Guided and template-assisted assembly

### 1.1.8.5.4. Design workflow for magnetic nanoparticles

Synthesis of the magnetic nanoparticle by using different precursors such as nitrate, chloride and organometallic compound, etc. Functionalization of MNPs by using drugs peptide and antibody.

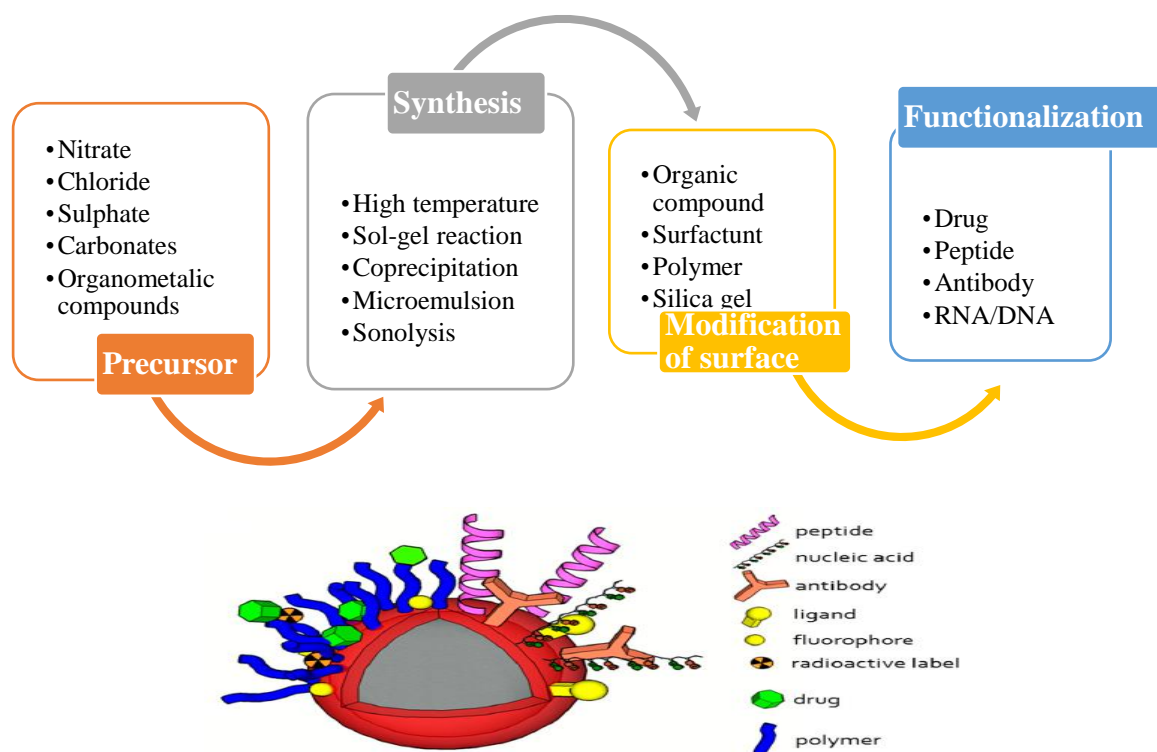




**Figure 1.5:** Possible modification and functionalization of magnetic particles.

#### 1.1.8.5.5. Application of magnetic nanoparticles

Magnetic nanoparticles have shown promising in many biomedical applications

- Increasing BBB Permeability and Drug Delivery
- Magnetic hyperthermia
- Enhancing magnetic resonance imaging (MRI) data
- Improve the delivery of bactericidal compounds to restricted microinches
- MNPs can be helpful also in anti-HIV therapy
- Used in stroke to deliver neural stem cells
- Used to target the hidden latent virus in the brain
- Also used to treat the neurological disorders caused by HIV damage to the CNS (neuro AIDS)

#### 1.1.8.6. Nanobubbles

An accurate definition for NBs: NBs are defined as nanoscopic gaseous cavities, which diameter is less than 1 micrometer. An equivalent term that can also be found in the literature is “ultrafine bubbles.” The international standards organization (ISO) has evaluated standards for submicrometer bubbles. As has already been mentioned, NBs can exist both on surfaces (surface or interfacial NBs) and as a dispersed phase in a liquid bulk phase (bulk NBs). Nowadays, NBs have drawn the attention of the scientific community due to their extraordinary longevity which ranges up to several weeks and even months<sup>59</sup>.

Nanobubbles (NBs) are small bubble-like structures that form at the interface of hydrophobic and hydrophilic surfaces in liquids. At room temperature, NBs are stable, but when heated to physiological temperatures in the body, they may combine to create microbubbles. The development of NBs is dependent on the nucleation of gas from a supersaturated solution at the hydrophobic surface, which traps ambient gases. Bulk, interfacial, plasmonic, and oscillating nanobubbles are the four types of nanobubbles<sup>60</sup>.

A lipid, protein, or biodegradable polymeric shell structure frequently surrounds microbubbles and nanobubbles. Microbubbles are 1 to 8 micrometers in size, whereas nanobubbles are submicron in size. Microbubbles are useful for molecular imaging of vascular targets because they are too large to extravasate and accumulate in the

perivascular zone. Microbubbles, on the other hand, appear to have difficulty reaching deep tissue layers, but nanobubbles have the ability to reach deep tissue layers via blood vessels. Microbubbles have recently been challenged by nanodroplets, which have been offered as a potential alternative. Nanodroplets have a perfluorocarbon or perfluoropentane core that is stabilized by albumin, lipid, or polymer shells. Because the cores have low boiling temperatures, the nanodroplets remain liquid at body temperature. As a result, nanodroplets could enter the perivascular area, such as the interstitial space of a tumor, through the leaky microvasculature. Ultrasound with a high acoustic pressure might then evaporate nanodroplets and convert them to microbubbles. Nanodroplets and ultrasound have been suggested as potential tools for imaging, thermal ablation, and medication and gene delivery <sup>61</sup>.

In the past few years, more and more attention has been given to the potential applications of the MBs and NBs. The applications are speeded to many sectors including the mining industry, medical applications, wastewater treatment, surface cleaning, and agriculture. Some of the most prominent applications are mentioned and discussed in this section.

#### 1.1.8.7. Magnetic oxygen loaded nanobubbles (MOLNBs)

MOLNBs (Magnetic Oxygen-Loaded Nanobubbles) are being investigated as theranostic carriers for delivering oxygen and treatment to brain tumors. MOLNBs are created by covering polymeric nanobubbles with superparamagnetic iron oxide nanoparticles (SPIONs). MOLNBs are oxygen-loaded vectors that can pass through brain membranes and deliver cargo to specific areas of interest via the Central Nervous System (CNS)<sup>62</sup>.

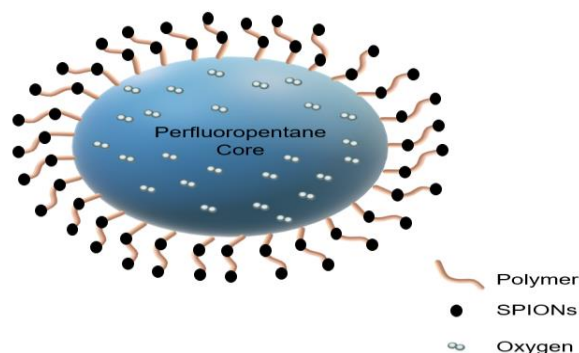


**Figure 1.6:** Sketch of MOLNBs

### 1.1.9. Polymers

A polymer is a substance with a molecular structure made up primarily or entirely of bound together similar units. Any of the following categories can be used to classify polymers: (1) Polymer source (natural, semi-natural, synthetic); (2) Polymer structure (linear, branched-chain, crosslinked, or network polymers); (3) Polymerization method (addition, condensation polymers); Molecular forces (elastomers, fibers, thermoplastics, and thermosetting); (5) Polymerization of chain development (free radical driven); (6) Degradability (biodegradable, non-biodegradable)<sup>63</sup>. Biopolymers are polymers that can be found in nature. Monomeric units are covalently linked together to form bigger structures. Based on the monomeric units employed and the structure of the biopolymer generated, there are three primary kinds of biopolymers. Polynucleotides are lengthy polymers made up of 13 nucleotide monomers or more. Polypeptides are short polymers of amino acids, and polysaccharides are polymeric carbohydrate structures that are often linearly connected.

The science and technology of biopolymers have led to the development of novel delivery systems, research interest, and investment by industry in recent decades. These polymers have been widely used in pharmaceutical industries as solubilizers, stabilizers, and mechanical supports for the sustained release of drugs. But over a period, the functionalities of polymers have changed. The polymers have been synthesized to suit specific needs or rather solve specific problems to widen their scope of applications. So, there is a need to understand the role of polymers<sup>64</sup>.

#### 1.1.9.1. Natural polysaccharides

Natural polysaccharides are the most abundant macromolecules found in the biosphere. The complex carbohydrates are constituted of monosaccharides joined together by glycosidic bonds. The natural polysaccharides are the main structural elements of plants and animals' exoskeleton (cellulose, carrageenan, chitosan, chitin, etc.) and play a key role in energy storage (starch, paramylon, etc.). Polysaccharides have many reactive groups, a wide range of molecular weight, varying chemical compositions and are therefore considered as promising biopolymers for developing desirable advanced functions. The amphiphilic nature imparted upon polysaccharides after modification gives them a wide and interesting application spectrum, for instance as rheology modifiers, emulsion

stabilizers, surface modifiers for liposomes and nanoparticles, and as drug delivery vehicles. Recently, the hydrophobic modification of polysaccharides has been receiving increasing attention because they can form self-assembled nanoparticles for biomedical uses. In nature, polysaccharides have various resources from algal, plant, microbial and animal origin. Starch, chitosan, dextran, cyclodextrin, cellulose, and pullulan are natural polysaccharides that have been modified with various reactants and are widely explored. Among numerous polysaccharides, cellulose and chitin are produced in the largest amounts and are the most abundant organic compounds on earth.

However, the fundamental biological and physicochemical features of chitin and its deacetylated form, chitosan, are attracting greater interest recently. The (acetyl)- amino groups on the polysaccharide backbone are undeniably important in demonstrating a variety of distinct characteristics. Non-toxicity, film- and fiber-forming properties, adsorption of metal ions, coagulation of suspensions or solutes, and different biological activities are some of the remarkable qualities of chitin and chitosan. Chitin and chitosan are thus considered bio-functional polymers with far more promise in a variety of disciplines, and they are important not only as abundant resources but also as a novel type of polymer<sup>65</sup>.

#### 1.1.9.1.2. Chitosan

Chitin (polymer of  $\beta$ -(1,4)-linked 2-acetamido-2-deoxy D- glucopyranose) is one of the most abundant organic materials/marine polysaccharides easily obtained from natural sources, e.g., the shells of crustaceans (lobster, shrimps, crabs, etc.) or the broth from the industrial fungal processes. Chitosan (poly- $\beta$ -(1 $\rightarrow$ 4)-2-amino-2-deoxy-D-glucose) is a nitrogenous (amino-based) polysaccharide, which is produced in large quantities by N-deacetylation of chitin. The following major characteristics of chitosan make this polymer beneficial for numerous applications: (1) it has a defined chemical structure; (2) it can be chemically and enzymatically modified; (3) it is physically and biologically functional; (4) it is biodegradable and biocompatible with many organs, tissues, and cells; (5) it can be processed into several products including flakes, fine powders, beads, membranes, sponges, cotton, fibers etc<sup>66</sup>.

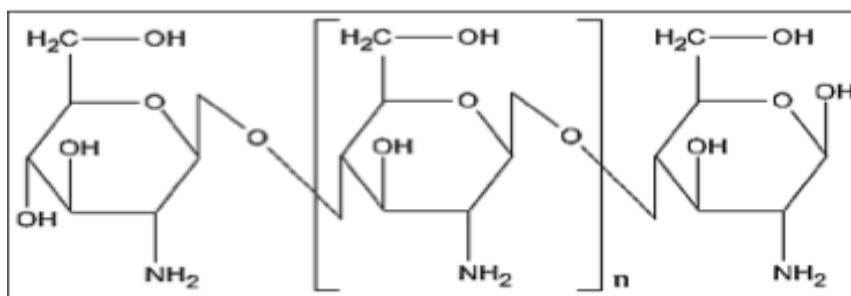


**Figure 1.7:** Chemical structure of Chitosan

#### 1.1.9.1.2.1. Physico-chemical properties of chitosan

#### 1.1.9.1.2.2. Production of chitosan

Chitosan is prepared by deacetylation of chitin. It is manufactured commercially by chemically treating the shells of crustaceans such as shrimps and crabs. The shells are initially deproteinized by treatment with aqueous sodium hydroxide solution (3-5%). The resulting product is neutralized, and calcium is removed by treatment with an aqueous hydrochloric acid solution (3-5%) at room temperature to precipitate chitin. *N*-deacetylation of chitin is achieved by treatment with aqueous sodium hydroxide solution (40-45%) at 110°C, and the precipitate is washed with water. The crude sample is dissolved in acetic acid (2%) and the insoluble material is removed. The resulting clear supernatant solution is neutralized with an aqueous sodium hydroxide solution to give a purified white precipitate of chitosan <sup>65,66</sup>.

#### 1.1.9.1.2.3. Degree of deacetylation

The extent of acetylation is one of the most important factors influencing the properties of chitin and chitosan. The *N*-acetyl content in both chitin and chitosan depends on their origin and isolation procedure. In chitin, the acetylated units prevail (DA≥90%), whereas chitosan is fully or partially *N*-deacetylated derivative with a DA of less than 30%. The degree of deacetylation determines the content of free amino groups in the polysaccharide. For assessing the degree of acetylation, methods such as infrared and *H*-nuclear magnetic resonance spectroscopies, titration, gel permeation chromatography are employed.

#### 1.1.9.1.2.4. Crystallography

The study of the crystalline structure of chitin/chitosan samples revealed that the partially deacetylated material was less crystalline and less anhydrous than pure chitosan. Crystallinity depends on the factors such as secondary treatment (reprecipitation, drying,

and freeze-drying), origin (affects residual crystallinity), diffusion properties, and deacetylation procedures that may affect the solid-state structure of chitosan.

#### 1.1.9.1.2.5. Molecular weight

Chitosan obtained from deacetylation of crustacean chitin may have an MW of over 100,000 Da. The MW of chitosan depends on its source and deacetylation conditions (time, temperature, and concentration of alkali). Evaluation of molecular weight of the polymeric chain is done using Viscometric and GPC techniques.

#### 1.1.9.1.2.6. Solubility

Chitosan, being a cationic polysaccharide in neutral or basic pH conditions, contains free amino groups hence, is insoluble in water. In acidic pH, amino groups can undergo protonation thus, making them soluble in water. Therefore, the solubility of chitosan depends on the distribution of free amino and *N*-acetyl groups. Chitosan is soluble in organic acids (formic, lactic, pyruvic, acetic, and oxalic acids). The extent of solubility also depends on the concentration and type of acid chosen for dissolution.

#### 1.1.9.1.2.7. Viscosity and Colour

Higher MW chitosan often renders highly viscous solutions, which may not be desirable for industrial handling. However, lower viscosity chitosan may facilitate easy handling. The solution viscosity of chitosan depends on its molecular size, cationic character, and concentration as well as the pH and ionic strength of the solvent. Chitosan occurs as flakes or fluffy powder and its colour varies from pale yellow to white.

#### 1.1.9.1.2.8. Pharmaceutical applications

##### **i. As antimicrobial agent against plant pathogens:**

Chitosan and chitosan derivatives have become a postharvest promising treatment for fruits and vegetables due to their natural character, antimicrobial activity, and elicitation of defense responses<sup>67</sup>.

##### **ii. Improvement in dissolution:**

Chitosan and its glutamate and hydrochloride salts were evaluated for their efficacy in improving the dissolution behavior of naproxen and its transport in-vitro across Caco-2 cell monolayers<sup>68</sup>.

**iii. Tissue engineering:**

Novel PLLA-chitosan hybrid scaffolds were proposed as tissue engineering scaffolds and simultaneously drug release carriers<sup>69</sup>.

**iv. Targeted drug delivery:**

Novel dendrimer nanoparticles were used as targeted drug-delivery carriers to cover a wide range of applications that involve the efficient intracellular delivery of biological agents to modulate the behavior of cells. (e.g., PAMAM dendrimer core with grafted CMC chitosan, dexamethasone (loaded nanoparticles).)

**v. Controlled drug delivery:**

Chitosan nanoparticles have been investigated for controlled delivery of doxorubicin<sup>70</sup>.

**vi. Dye removal:**

Chitosan grafted with cyclodextrins, cyclodextrin derivatives can form complexes with a variety of other appropriate compounds and are very promising materials for developing novel sorbent matrices. Adsorption of textile dyes from the effluent can be carried out with -CD-g- chitosan derivatives<sup>71,72</sup>.

**vii. Adsorption of metal ions:**

A great number of chitosan derivatives have been obtained to absorb metal ions by including new functional groups onto chitosan back-bone<sup>73</sup>.

**viii. Carrier for peptide:**

Recent studies have shown that chitosan as the mucoadhesive polymer is a useful carrier for oral delivery of peptide drugs<sup>74</sup>.

**1.1.9.1.3. Glycol Chitosan**

Glycol chitosan is a carbohydrate derivative that increases membrane permeability in Glycine max Harosoy 63W cells. A chitosan derivative, Glycol chitosan has hydrophilic ethylene glycol branches. Glycol chitosan is non-cytotoxic. Due to its biocompatibility, Glycol chitosan is used for targeted drug delivery. Glycol chitosan is water-soluble. Glycol chitosan has been observed to inhibit E. coli, S. aureus, and S. enteritidis growths.

**1.1.9.1.4. Dextran sulfate Sodium salt**

Dextran is a complex branched glucan (polysaccharide derived from the condensation of glucose), originally derived from wine. IUPAC defines dextran's as "Branched poly- $\alpha$ -d-

glucosides of microbial origin having glycosidic bonds predominantly C-1 → C-6". The polymer main chain consists of  $\alpha$ -1,6 glycosidic linkages between glucose monomers, with branches from  $\alpha$ -1,3 linkages. This characteristic branching distinguishes a dextran from a dextransin, which is a straight-chain glucose polymer tethered by  $\alpha$ -1,4 or  $\alpha$ -1,6 linkages<sup>75</sup>. Dextran sulfate sodium salt, or DSS, is a synthetic sulfated branched polysaccharide derivative of dextran that has multiple uses in biomedical and clinical research. Dextran sulfate sodium (DSS) is one of the most common and effective compounds used for inducing ulcerative colitis in animals. The DSS colitis model has also been used extensively to study colon cancer development to colonic inflammation, such as that occurring in patients with long-standing ulcerative colitis.

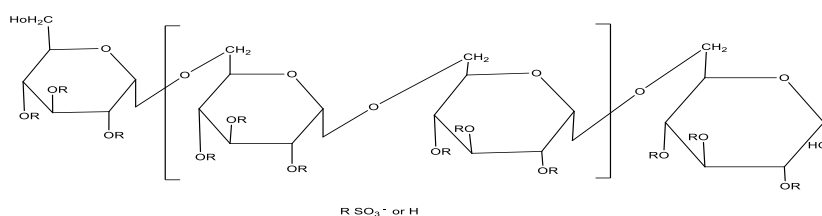


**Figure 1.8:** Structure of Dextran Sulphate

#### 1.1.9.1.3.1. Characteristics

Parameters	
Molecular weight	36,000 - 100,000 Da
Boiling Point	310 °C
Melting Point	92 °C
pH	5-7
Solubility	100/mL in water

#### 1.1.9.1.3.2. Pharmaceutical Application

- Dextran is used in some eye drops as a lubricant<sup>76</sup>. and in certain intravenous fluids to solubilize other factors, such as iron (in a solution known as Iron Dextran).
- Intravenous solutions with dextran function both as volume expanders and means of parenteral nutrition. Such a solution provides an osmotically neutral fluid that once in the body is digested by cells into glucose and free water. It is occasionally used to replace lost blood in emergencies, when replacement blood is not available<sup>77</sup>, but must be used with caution as it does not provide necessary electrolytes and can cause hyponatremia or other electrolyte disturbances.
- Dextran can be used in an ATPS for PEGylation





Chapter 2:



*Review*

# Magnetic Iron Oxide Nanoparticles: Synthesis, Characterization and Functionalization for Biomedical Applications in the Central Nervous System

Shoeb Anwar Mohammed Khawja Ansari <sup>1,†</sup>, Eleonora Ficiarà <sup>1,†</sup>, Federico Alessandro Ruffinatti <sup>2</sup> , Ilaria Stura <sup>3</sup>, Monica Argenziano <sup>4</sup>, Ornella Abollino <sup>5</sup>, Roberta Cavalli <sup>4</sup>, Caterina Guiot <sup>1</sup> and Federico D'Agata <sup>1,\*</sup> 

## 2.1. Introduction

In the last decades, the power of nanotechnology in numerous fields including biomedical sciences has been exploited. Nanoparticles (NPs) are solid colloidal particles ranging in size from 1 to 100 nm. Due to their dimensions comparable with those of cells, viruses, proteins, and genes, they opened the potentiality of interacting with fundamental biological processes<sup>78</sup>. In recent years, much attention has been paid to the synthesis of different kinds of NPs as nano-medical materials. Among them, engineered Magnetic Nanoparticles (MNPs) made of iron, cobalt, or nickel oxides exhibit special properties, including high surface-to-volume ratio and high magnetic moment, allowing potential manipulation by an external magnetic field<sup>79</sup>. Especially, MNPs manufactured with a ferromagnetic material, i.e., Iron Oxide Nanoparticles (IONPs), made of magnetite ( $\text{Fe}_3\text{O}_4$ ) and maghemite ( $\text{Fe}_2\text{O}_3$ ) combine ideal biocompatibility with superparamagnetic properties allowing widespread biomedical<sup>80,81</sup>. The enhancement of effective drug delivery by magnetic driving of sensitive MNPs has been especially explored to treat diseases of the Central Nervous System (CNS). In fact, due to the aging of the population, CNS pathologies such as neurodegenerative diseases are increasingly becoming a relevant medical and social issue<sup>82</sup>. Current pharmacological treatments are mainly based on the systemic delivery of active substances into the CNS, whose effectiveness is seriously limited due to the presence of blood-brain-barrier (BBB). MNPs are therefore considered powerful tools to cross BBB by means of physical mechanisms and properly deliver the drug cargo in the brain. There are many in vitro and in vivo evidence of BBB trespassing by MNPs under magnetic fields to deliver therapeutic agents in the CNS<sup>83,84</sup>.

Several steps have to be taken into account to design MNPs suitable for magnetic drug delivery in CNS. Currently, many methods of synthesis are available making it possible to produce a wide spectrum of different MNPs, by optimizing protocols, to obtain the best physicochemical properties<sup>85</sup>. Focusing on IONPs, they are usually made of a crystalline core and a surface coating (e.g., dextran, citrate, chitosan, polyethylene glycol, albumin, etc.), whose dimensions are tunable to improve their stability, enhance their biocompatibility, and optimize their bio-distribution. NP coating may be modified with specific targeting molecules or drugs. This variety of physical features and coatings characterizes IONP action mechanisms and toxicity patterns<sup>86</sup>. Moreover, since the synthesis methods affect the IONP size distribution, the degree of structural defects, the surface chemistry, and the magnetic

behavior, they finally also determine the interaction with biological barriers such as BBB and lipid bilayer of a cell membrane and the consequent biocompatibility in the living organisms<sup>87,88</sup>. Furthermore, the iron content in IONPs has a key role in the general iron homeostasis of the body and the CNS environment, highly sensitive to iron imbalance, especially in neurodegenerative diseases.

## 2.2. Synthesis of IONPs

oxides) The most commonly used material for the synthesis of MNPs consists of compounds (usually oxides) of iron, cobalt, or nickel in combination with other metals such as copper, zinc, strontium, and barium. However as already mentioned, this review focused only on those procedures and precursor compounds suitable for the production of iron oxide MNPs. In general, the synthesis of MNPs is a very critical multistep procedure, which must be optimized since its early design phase given that even a small variation in the production process can significantly change the outcome<sup>89</sup>. For this reason, both the physical and chemical properties of the particles need to be strictly controlled to fit a number of different applications. Specifically, depending on the desired features and the final field of application, three main routes for IONPs preparation have been developed during the last decades: Chemical, physical, and biological, the former comparing about 90% of all synthesis methods<sup>90,91</sup>.

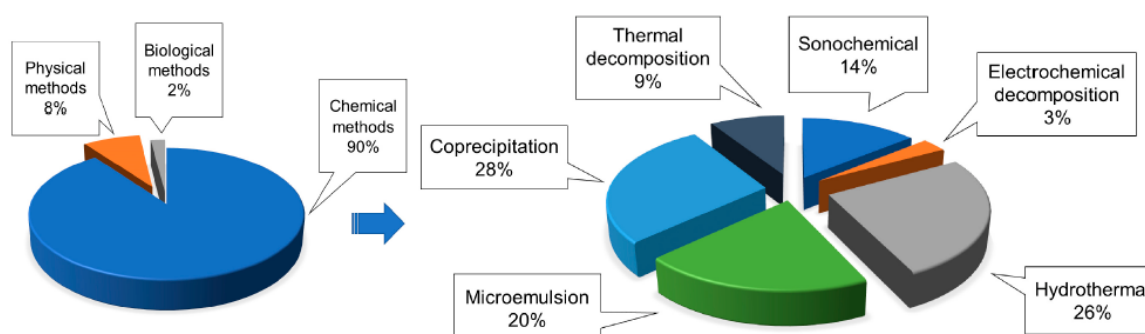


**Figure 2.1.** A comparison among the prevalence of the main methods currently existing for the synthesis of IONPs, with the detailed chemical methods prevalence.

### 2.2.1. Co-precipitation method

The co-precipitation method is probably the most popular method for IONP synthesis. In particular, it is widely used in biomedical applications, because of the non-toxic nature of the materials usually employed<sup>92</sup>. The term “co-precipitation” refers to the phenomenon by

which a precipitate can carry down one or more substances normally soluble in those particular conditions through nucleation and grain growth. This method allows MNPs to be synthesized in an inert nitrogen atmosphere at room temperature [17]. For a schematic representation of such a synthesis technique, see Figure 2.2, where a typical procedure for the production of spherical IONPs is shown. Through the co-precipitation synthesis, it is possible to obtain MNPs broadly distributed around a mean diameter value ranging from 5 to 40 nm (Table 2.1)<sup>93</sup>. More generally, the size, shape, and magnetic properties of the resulting IONPs depend on reaction conditions such as the type of salts used [19], pH, and ionic strength<sup>94,95</sup>.



**Figure 2.2.** Flowchart for the synthesis of IONPs by co-precipitation<sup>96</sup>. In this example, Fe<sub>3</sub>O<sub>4</sub> NPs are prepared from a mixture of FeSO<sub>4</sub> and FeCl<sub>3</sub> in the molar ratio of 1:2. Magnetic phase and particle size can be adjusted by varying Fe<sup>2+</sup>/Fe<sup>3+</sup> ratio, temperature, pH, and the type of base used.

### 2.2.2. Thermal decomposition method

Thermal decomposition is one of the most efficient methods for the generation of small size MNPs, often allowing fine-tuning of the average particulate diameter<sup>97</sup>. In particular, thermal decomposition can be achieved by two different protocols, namely “heating-up” and “hot-injection”. The heating-up process implies the continuous heating of a pre-mixed solution of precursor compounds, surfactants, and solvent, up to a given temperature at which NPs start clustering and growing<sup>98,99</sup>. On the contrary, the hot-injection method induces fast and homogeneous nucleation by injecting reagents into a hot surfactant solution followed by a controlled growth phase. In any case, both the processes are based on the same principle consisting of heating a non-magnetic organometallic precursor compound in the presence of organic solvents and surfactants<sup>100</sup>. The non-magnetic precursors are usually iron carbonyls and acetyl acetates, whilst the fatty acids generally are used instead of oleic acid as surfactants. Especially in the inert atmosphere, argon plays an important role. The optimal

temperature necessary for this response is 100 °C to 350 °C, which means crystalline MNPs are forming, ranging from 4 to 30 nm in diameter (Table 2.1) and have a high degree of evenness (i.e., a narrow distribution of size)<sup>101</sup>. Temperature and time of reaction are important factors for the control of particle size.

### 2.2.3. Microemulsion method

In the presence of a surfactant, the microemulsion consists of two non-mixable liquids that form a monolayer at the interface of oil and water and potentially display an ultra-low interface tension<sup>102</sup>. This is a thermodynamic stable distribution. The physicochemical properties of NPs produced by such a technique rely on the preference of surfactant. In general, the IONPs are synthesized with intracellular nucleation and growth in microemulsion. Sphere forming nanoparticles with a median diameter between 10 and 25 nm<sup>103,104</sup> are nearly monodispersed.

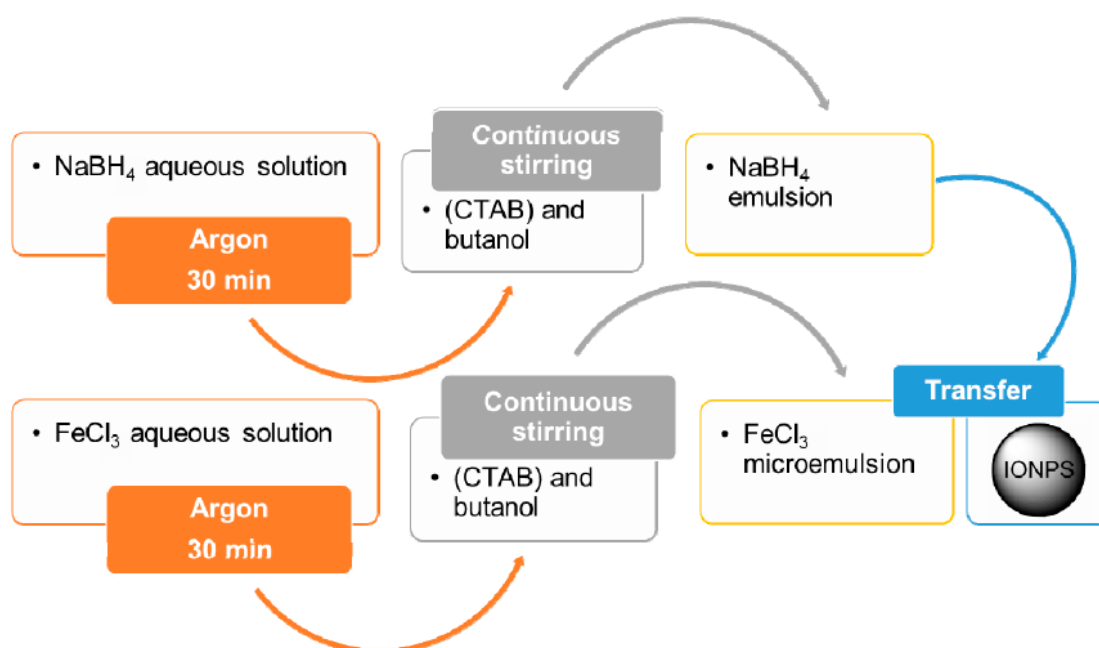


**Figure 2.3.** Flowchart for the synthesis of IONPs by microemulsion. Two W/O microemulsions (respectively with FeCl<sub>3</sub> and NaBH<sub>4</sub> in aqueous solution) are used for the preparation of MNPs with an iron core coated by a Fe<sub>3</sub>O<sub>4</sub> shell<sup>104</sup>. Abbreviation: CTAB = cetyltrimethylammonium bromide.

### 2.2.4. Hydrothermal method

A broad range of crystalline IONPs can be synthesized by using the hydrothermal method. The general system consists of (solid) metal linoleate, an ethanol-linoleic acid liquid phase, and

water-ethanol solution kept under hydrothermal (i.e., high-temperature and high-pressure) conditions<sup>105</sup>. Specifically, the typical reaction temperature to perform hydrothermal synthesis is around 220 °C, while the required pressure is above 107 Pa, for a total reaction time of about 72 hours<sup>106</sup>. Usually, a temperature gradient is created within a Teflon-lined stainless-steel autoclave whose cooler end will host the deposition of the mineral solute, finally growing the desired crystal. Through this technique, the shape and size of the resulting NPs are generally very uniform, with the possibility of tuning NP size from a few nanometers to several hundred (see Table 2.1)<sup>107,108</sup>. The distribution of particles and the size of the particles depend on the concentration of the precursor, total response time, and temperature. Furthermore, hydrothermal synthesis is eco-friendly and flexible, since organic or post-treatment solvents are not needed.

### 2.2.5. Polyol method

The polyol method allows synthesizing uniform MNPs at a relatively low temperature and it is based on precursor compounds such as oxides, acetates, and nitrates dissolved or suspended in diols (Figure 2.4). It is a versatile and up-scalable method suitable for the production of large batches of IONPs, encompassing a wide range of possible size, from ultra-small spheres of 4 nm in diameter to larger ones up to 100 nm, depending on reaction conditions (e.g., temperature, reaction time, heating profile, nature of the polyol solvent, or organometallic precursors). The polyol method is also a useful technique for the synthesis of nanocrystalline alloys and bio-metallic clusters. Table 2.1 shows the typical time and temperature required to obtain NPs through this procedure<sup>109</sup>.

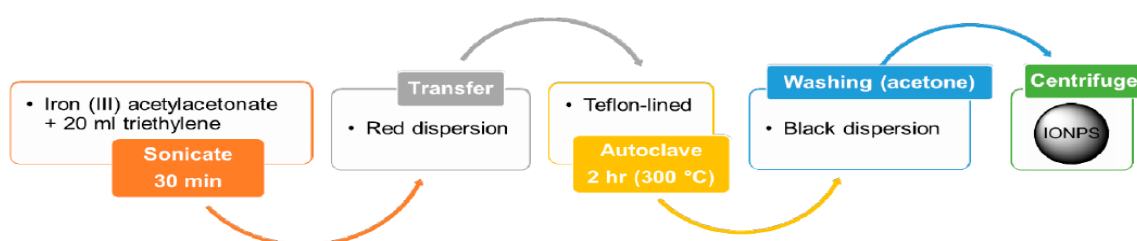


**Figure 2.4.** Flowchart for the synthesis of IONPs by polyol method. IONPs are here prepared from a reaction between a metal acetylacetonate (precursor compound) and triethylene (diol solvent).

### 2.2.6. Sol-gel method

This method for IONP production consists of the hydroxylation and condensation of some iron precursors forming a “sol” (i.e., a colloidal solution) of nanoparticles that are then dried—

“gelled”—by solvent removal until an iron oxide 3D network is obtained (see Figure 2.5)<sup>110</sup>. In this method, water is generally used as a solvent; alternatively, precursors may also be hydrolyzed by acids or bases. The reaction can be conducted at room temperature and can be tuned between 15 and 50 nm for the size of the resulting spherical IONPs.

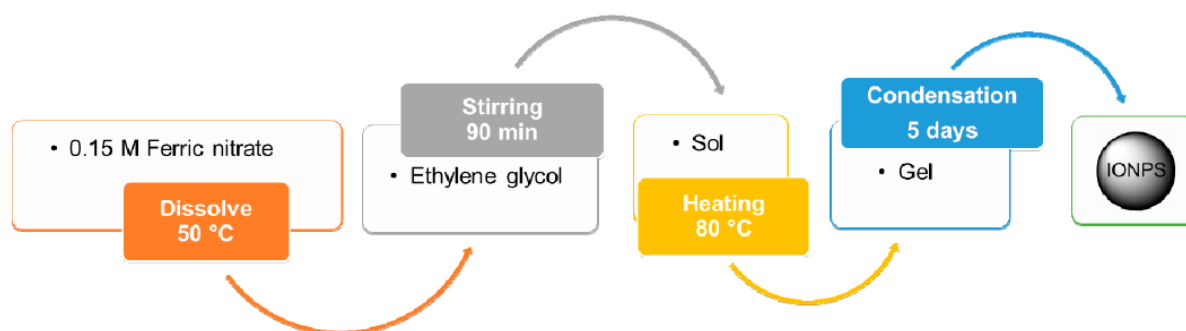


**Figure 2.5.** Flowchart for the synthesis of IONPs by sol-gel method [41,42]. Ferric nitrate is directly dissolved in ethylene glycol at 50 °C. The resulting sol is then dried by heating to get the gel and, finally, the IONPs of interest.

**Table 2.1.** IONP synthesis techniques and comparison with respect to their different parameters

Methods	Temperature	Time	Size
<b>Co-precipitation</b>	20–150 °C	Minutes	5-40 nm
<b>Thermal decomposition</b>	100–350 °C	hours- days	4-30 nm
<b>Microemulsion</b>	20–80 °C	Hours	10-25 nm
<b>Hydrothermal</b>	150–280 °C	hours- days	10-800 nm
<b>Polyol</b>	130-220 °C	Hours	4-100 nm
<b>Sol-gel</b>	25–200 °C	Hours	15-50 nm

Compared with other nanoparticle synthesis methods, the IONPs prepared by the above methods such as co-precipitation, thermal decomposition, microemulsion, and sol-gel, etc. have superior targeting abilities. In the event of neurological disease, IONPs are supposed to have advantages beyond the improved permeability and retention effects, which is a common technique. IONPs are the chosen carrier to cross the blood-brain barrier. Due to the proper form, size, and stability of NPs, the IONPs prepared using these synthesis techniques have the

potential to cross the BBB the main advantage of these techniques is that the preparation of IONPs does not require hazardous solvents. To decrease the toxic effect of IONPs on neurons, water is the most widely used solvent. Dextran-coated IONPs prepared by the co-precipitation method are typically used because of the non-toxic quality of the materials usually used for MRI comparison of the central nervous system. Via high localization at the target site under the magnetic field, nanoparticles can provide targeted drug delivery and boost imaging and therapeutics. Synergistically, under alternating magnetic fields, these nanoparticles often induce tumor cell death through localized hyperthermia. In a rapidly growing number of applications, such as cell labeling, separation, and monitoring, IONPs are used for cancer and neurological disease therapeutic agents. The tailored properties of nanoparticles, such as unique sizes, shapes, surface features, and magnetism, are necessary for these applications.

### 2.3. Characterization of IONPs

After the synthesis of IONPs, the characterization of their physicochemical properties can be provided by using several sophisticated techniques (see Table 2.2). In the next sections, the focus will be on the techniques used to investigate the shape, size, size distribution, and magnetic properties of IONPs.

#### 2.3.1. Microscopic Techniques

Due to the very high resolution achieved by electron microscopy (<1 nm), both Scanning Electron Microscopy (SEM) and Transmission Electron Microscopy (TEM) are widely used to determine, respectively, the surface morphology and the inner structure of NPs. Unlike SEM which produces images making use of reflected (or knocked-off) electrons, TEM indeed works by detecting transmitted electrons that may carry valuable information on the IONP inner structure (e.g., crystal structure, stress state, and more)<sup>111</sup>. Moreover, nanometric investigation of shape heterogeneity, average size, and dispersion can be accomplished by using scanning tunneling microscopy and atomic force microscopy.

#### 2.3.2. Spectroscopic Techniques

Many spectroscopic techniques are used for IONPs characterization. X-ray diffraction allows collecting information about the crystalline structure of the particles (i.e., angle, width), while structure characterization and functional group determination, are commonly performed by Fourier-Transform Infrared (FTIR) spectroscopy<sup>112</sup>, thanks to the presence of molecules



absorbing light in the region from 2.5  $\mu\text{m}$  to 15  $\mu\text{m}$ (wavenumber from 4000  $\text{cm}^{-1}$  to 660  $\text{cm}^{-1}$ ). Alternatively, NMR (Nuclear Magnetic Resonance) techniques can be used to study the structure of a compound. The ability of NMR to provide information regarding the specific bonding structure and stereochemistry of molecules of pharmaceutical interest has made it a powerful analytical instrument for structural determination<sup>113</sup>. Furthermore, the thermal stability of IONPs can be determined by using the thermogravimetry analysis<sup>114</sup>. Dynamic Light Scattering (DLS) has several advantages for sizing MNPs and it has been widely used to determine the hydrodynamic diameter of IONPs (typically ranging between 30 to 190 nm) via the Stokes-Einstein equation<sup>115</sup>. Moreover, IONPs can be electrostatically characterized by using Zeta potential measurement to determine their surface charge (see Table 2.2). In general, surface charge, and in turn, the Zeta potential can be modified by using polymer coating<sup>116</sup>. Mass spectroscopy requires a very small amount of sample to determine molecular weight and surface properties with high accuracy and precision. Fluorescence correlation spectroscopy (using visible and UV radiation) is normally employed for studying concentration effects, molecular diffusion, and chemical kinetics. Surface-enhanced Raman spectroscopy and circular dichroism make it possible to determine IONP structural conformation; Raman spectroscopy, in particular, offers the unique possibility to record spectra directly in an aqueous solution, without the need for any sophisticated sample preparation (see Table 2.2).

**Table 2.2.** Different characterization techniques used to assess the physicochemical properties of IONPs

<b>Techniques</b>	<b>Evaluation</b>
<b>Infrared spectroscopy (IR)</b>	Nature of surface functionalization
<b>Nuclear magnetic resonance spectroscopy (NMR)</b>	Longitudinal and transverse relaxivity; Structure conformation
<b>Superconducting quantum interference device (SQUID); Vibrating sample magnetometry (VSM)</b>	Magnetic properties
<b>Electron microscopy (transmission, TEM; scanning, SEM)</b>	Morphology, crystallinity, size distribution, composition

<b>X-ray diffraction (XRD)</b>	Crystal structure, size
<b>Dynamic light scattering (DLS)</b>	Hydrodynamic diameter
<b>Zeta potential measurement</b>	Surface charge
<b>Thermal analysis (differential scanning calorimetry, thermogravimetric analysis, etc.)</b>	Surface coverage, thermal stability, nature of surface functionalization, carrier-drug interaction
<b>Mass spectroscopy</b>	Molecular weight
<b>Fluorescence correlation spectroscopy</b>	Dimension, binding kinetics of hydrodynamic
<b>Surface-enhanced Raman scattering</b>	Size distribution, electronic characteristics
<b>Circular dichroism</b>	Thermal constancy
<b>Scanning tunneling microscopy.</b>	Shape heterogeneity,
<b>Small-angle X-ray scattering</b>	Size and size navigation
<b>Atomic force microscopy</b>	Shape heterogeneity

---

#### 2.4. Application to CNS

Focusing on CNS applications, the characterization of IONPs is essential to elucidate phenomena such as magnetic field interaction and agglomeration. In the presence of a magnetic field, the main uses of IONPs concern contrast agents for MRI, hyperthermia, and crossing BBB to reach the target brain region. For example, octopod SPIONs, characterized by TEM analysis and SQUID, showed a more effective MR contrast effect compared to spherical ones, allowing for accurate cancer detection<sup>117</sup>. This novel strategy could also be useful for the treatment of hyperthermia and magnetic-guided delivery of drugs to the CNS. Accumulation of NPs in tumor cells was evaluated through histological studies and these SPIONs also showed enhanced properties for targeted chemotherapy and brain tumor delineation. In addition, the strategy for synthesis in (IONPs stabilized SiO<sub>2</sub> matrix) avoided agglomeration phenomena and SQUID characterization revealed effective magnetic excitation to produce hyperthermia. Finally, the magnetic properties indicate the passage of

IONPs through the endothelial monolayer. Static magnetic fields can make it easier for IONPs to enter the brain and deliver the drug product properly. Alternating magnetic fields may increase the permeability of BBB by magnetic heating. The uniform distribution was evaluated using in situ TEM and SEM in ultra-thin sections of the brain mice with minimal agglomeration<sup>118</sup>.

## 2.5. Functionalization of IONPs for CNS applications

The most important limitation to drug delivery in the brain is the presence of the BBB, which virtually inhibits the diffusion of the majority of substances to neurons. IONPs can be used to overcome this limitation, but attention has to be posed to possible induced neurotoxicity caused by their oxidation and to mechanisms for enhancing and/or controlling the barrier trespassing. Naked IONPs without coating face many problems such as aggregation in water, chemical instability in the air, poor biodegradability in the physiological environment, and non-specific interaction with serum protein<sup>119</sup>. To prevent iron oxidation and to minimize the direct exposure of the biological surfaces to IONPs, coating with a biocompatible shell is required. The interaction with cells and functionalized NPs strongly depends on the inorganic or organic materials used<sup>120</sup>. The principal objectives of the IONPs surface modification are as follows:

1. Improving or modifying tissue dispersion.
2. improve the operation on the surface.
3. Improving mechanical and physicochemical properties.
4. Biocompatibility enhancement.

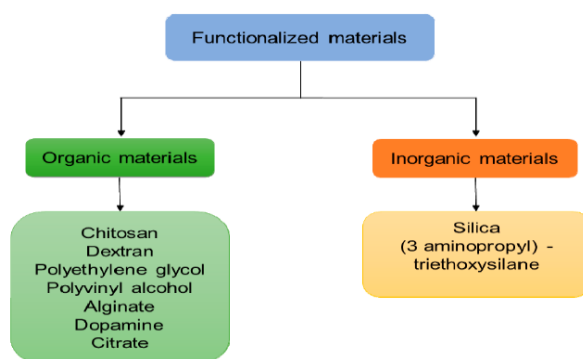


**Figure 2.6.** Flowchart of classification of organic and inorganic materials used for the functionalization of IONPs.

### 2.5.1. Ligand addition

The main premise of this approach is to introduce a ligand molecule to the IONPs external surface without removing any previously applied ligand. Many functional groups can bind to the surface of IONPs, including hydroxyl, carbohydrate, thiol, and phosphonate (Figure 2.7)

121

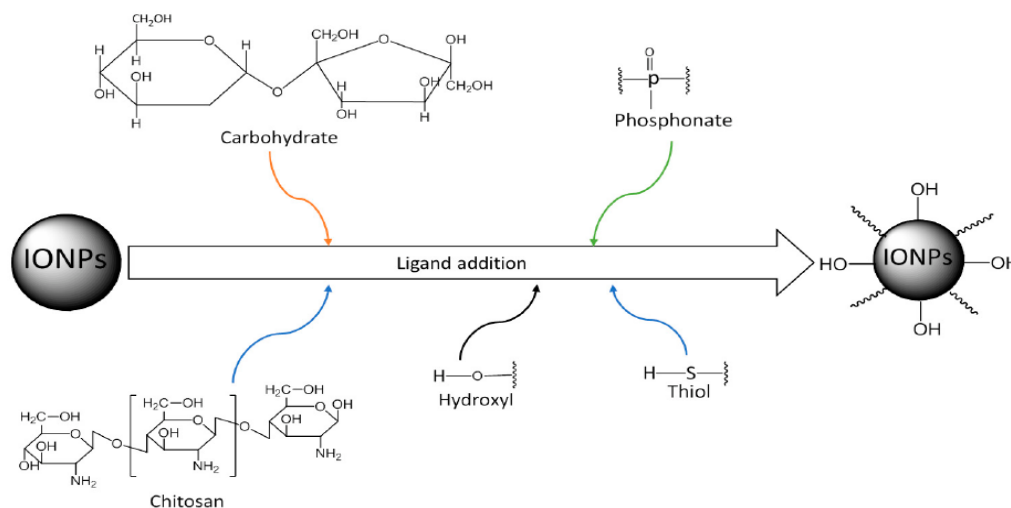


**Figure 2.7.** Surface modification of IONPs by ligand addition

### 2.5.2. Ligand exchange

Ligand exchange is the most commonly used method for controlling the surface properties of IONPs<sup>122</sup>. Ligand exchange can convert the hydrophobic character of IONPs to hydrophilic<sup>119</sup>. In the ligand exchange, a new type of functional group replaces the initial hydrocarbon layer directly. The new ligand contains two different kinds of functional groups: 1) Functional groups, which can directly link to the surface of the IONPs tightly by the effect of their chemical bonding; and 2) other functional groups that help particles dissolve in water solution.

### 2.5.3. Silica coating

Silica is the most used compound for surface coating of IONPs to reduce the toxicity<sup>120</sup>. Silica coating is widely applied to the surface functionalization of NPs and also to improve stability in water and it protects them in an acidic environment. In general, silica coating increases the particle size and modifies the magnetic properties of IONPs. It helps in binding with the various ligands at the surface and provides a protective layer for drug molecules and IONP itself<sup>123</sup>. Moreover, when forming a silica shell, small molecules such as dyes, drugs, and even quantum dots may be consolidated. Due to these points of interest, SiO<sub>2</sub> coating is prominent

in attractive IONPs, and silica surfaces can be joined by antibody-antigen recognition to target organs by covalent application with various ligands and biomolecules. It improves colloidal stability by controlling the coating process relatively easy and is considered highly biocompatible and open to multiple surface biological conjugation. Above all, photoacoustic imagery appropriate. Some silica coatings help reduce the toxicity of IONPs as well.

#### 2.5.4. Aminosilane coating

Nanoparticles Aminosilane (AmS) coated IONPs are widely used as a multifunctional drug delivery system. Surface modification of IONPs by AmS can indeed prevent aggregation and allows the addition of specific functionalities to IONPs. As for their biocompatibility, it has been shown that AmS-coated particles affected cell metabolic activity only at high concentrations (around 200 µg/mL) while leaving the membrane intact. On the other hand, AmS-IONPs at concentrations above 200 µg/mL has been shown to reduce neuron viability by 50%, both in the presence or absence of a magnetic field.

#### 2.5.5. Polymer coating

Polymer functionalized IONPs have been extensively investigated for their unique physical and chemical properties. The polymer-coated iron oxide nanoparticles (PIONPs) are used in various biomedical applications such as PET imaging or fluorescent imaging (Table 2.3). Recently, PIONPs have been used to treat anaemia and neurological disorder<sup>124</sup>.

**Table 2.3.** Polymers used for functionalized IONPs in biomedical applications.

Polymers	Advantage	Application
Chitosan	Biocompatible, hydrophilic	MRI contrast agent, Drug delivery agent
Dextran	Enhance blood circulation, stabilizes colloidal suspension	MRI contrast agent, Molecular diagnostic agent
Gelatin	Gelling agent,	Magnetic resonance imaging

biocompatible emulsifier

<b>Polyethylene glycol</b>	Internalization efficiency of the NPs	Magnetic hyperthermia agent, MRI theranostics
<b>Polyvinyl alcohol</b>	Prevents particles coagulation	Drug delivery agents, cytotoxicity studies

---

During the last years, IONPs have shown the best performance in the treatment of CNS pathologies, especially through various coating forms. Another important feature of their surface modifications is the enhancement of biocompatibility of naked IONPs. Silica-coated SPIONs showed strong biocompatibility and a successful magnetic guiding delivery in a cerebral region with diseases. In this respect, alternatively, organic coating SPIONs have shown their exceptional protection, which makes it possible to use them more extensively for current and potential CNS applications. For example, Dextran-stability SPION's storage analysis has been conducted for different MRI application temperature conditions. Show strong stability and lack of sedimentation or agglomeration. Chitosan is another natural polymer used in different applications of the CNS, such as the delivery of drugs. The benefits of Chitosan IONPs are their medicinal support functions, which do not affect the properties of NPs. In contrast, due to the reduced solubility in the water physiological pH, Chitosan has certain limitations that lead to the chemical changes required for better water solubility. Interestingly chitosan-dextran hybrid SPIONS have improved the internalization of glioblastoma cells and demonstrated the challenge of enhancing cellular uptake by using new formulations. Furthermore, antibody-conjugated polyethylene glycol-coated IONPs promote the internalization of biologically healthy brain tumor cells<sup>125</sup>. In the in-vitro BBB model, Ivask and his colleagues compared uptakes and transcytosis of various functionalized SPIONs. These results also show that polymer coating is one of the best strategies to enhance the internalizations of IONPs via endothelial cells forming BBB and the subsequent release into

the CNS. The best candidates for the optimized formulations of coated IONPs for improved targeted transport of drugs over the BBB are Dextran, Chitosan, and Polyethylene Glycol.

## 2.6. Application to CNS

In recent years, IONPs functionalized by utilizing different types of the coating were investigated for the treatment of important CNS pathologies. The improvement of biocompatibility with respect to naked IONPs is a crucial point of their surface modifications. In this regard, silica-coated SPIONs showed good biocompatibility and effective magnetic-guided deliverability into the diseased brain regions<sup>126</sup>. Alternatively, the coating of SPIONs by using organic materials also provided high safety levels, allowing more extensive use of these agents in the current and future CNS applications. For example, the stability of dextran-SPIONs for MRI application following storage at different temperatures was monitored in Reference<sup>127</sup>, showing good stability and the lack of agglomeration or sedimentation. Chitosan is another natural polymer used in various CNS applications, such as drug delivery. The main benefit deriving from chitosan coating consists in the support function it can provide for a different types of drugs, without impairing the NP properties. Unfortunately, chitosan presents also some limitations due to its reduced solubility in water at physiological pH, thus making chemical changes for improving water-solubility necessary<sup>128</sup>. For this purpose, an interesting hybrid chitosan-dextran SPION system can enhance the internalization inside glioblastoma cells, revealing how new formulations can improve cellular uptake. Similarly, antibody-conjugated polyethylene glycol-coated IONPs were shown to promote the internalization in brain tumor cells with a high stability degree when suspended in biological media<sup>129</sup>. Ivask and colleagues compared uptake and transcytosis of different functionalized SPIONs in an in vitro BBB model<sup>129</sup>. Overall, these findings point out that polymeric coating is one of the most powerful strategies for improving the internalization of IONPs by the endothelial cells of the BBB and the consequent release in the CNS. In particular, dextran, chitosan, and also polyethylene glycol are the best candidates to study optimized formulations of coated IONPs and improve targeted drug transport across BBB.

## 2.7. Conclusions and Future Perspectives

Because of driven by the external magnetic field, IONPs are considered one of the most promising technologies for biomedical applications due to their unique physicochemical features. IONPs, in particular, could be suitable for physical targeting of the CNS, allowing for

better BBB crossing and medication administration into the brain. As a result, research in the production of tailored IONPs using controllable synthesis methods and careful adjustment of their properties is ongoing. about potential tactics for designing suitable IONPs that can progress from proof-of-concept to clinical settings in the future. Adjusting the parameters of the synthesis process is the first needed step in ensuring an accurate selection of physicochemical features such as size, shape, and structure. At the same time, improving numerous biomedical applications in the CNS requires the functionalization of IONPs with different polymers or chemical compounds. To better understand the interaction of IONPs with the external magnetic field utilized as a driving/delivery mechanism, a deeper examination of the magnetic characterization of IONPs is required. As seen by the huge number of current studies focused on the precise examination of magnetic properties like saturation magnetization, coercive field, and remnant magnetization, the emergent trait of superparamagnetism makes IONPs interesting nanomaterials. These parameters are crucial for the interaction with the applied magnetic field, which allows magnetic-driven nanocarriers to be modulated in the biological environment.

Furthermore, the assessment of biocompatibility and potential risk related to IONP exposure must be given special attention. The low toxicity of IONPs is widely recognized, but because results are often conflicting, more research is needed, as well as the development of novel cell models to evaluate it. This is a critical issue since the CNS is highly vulnerable to iron imbalance, particularly in the abnormalities of iron homeostasis that are closely linked to neurodegenerative diseases.

In conclusion, a challenging aspect is a need for new smart magnetic nanocarriers able to cross BBB and to reach the brain from the bloodstream effectively and safely. For this purpose, the use of an integrated approach taking into account type, composition, functionalization, and minimization of toxicity can promote the optimal choice for magnetic-field-directed NPs.



## Chapter 3:



# Superparamagnetic Oxygen-Loaded Nanobubbles to Enhance Tumor Oxygenation During Hyperthermia

*Sara Zullino<sup>1,2†</sup>, Monica Argenziano<sup>3†</sup>, Shoeb Ansari<sup>3</sup>, Roberta Ciprian<sup>4†</sup>, Lucia Nasi<sup>4</sup>, Franca Albertini<sup>4</sup>, Roberta Cavalli<sup>3\*</sup> and Caterina Guiot<sup>2</sup>*

### 3.1. Introduction

Oncological hyperthermia (HT) is a treatment that involves raising the temperature of the tumor between 40°C and 45°C for about an hour in two to three weekly sessions, often concomitantly with radiotherapy (RT) and sometimes radiochemotherapy<sup>130–133</sup>.

The capacity to heat the tumor almost uniformly and persistently during the HT session is the key to its effectiveness. In fact, clinical success in most tumors requires reaching a breakpoint temperature, which is traditionally assumed to be cumulatively equivalent to 43°C according to the definition of cumulative equivalent minutes at 43°C<sup>134</sup>, for a significant fraction and over a significant volume of the tumour (90 %)<sup>135</sup>.

External heating devices based on microwaves, radiofrequency (RF), ultrasound (US), or infrared are frequently inadequate for treating the entire tumor volume, particularly deep-seated tumors<sup>133</sup>, and while physiological vasodilatory-based temperature control can be countered in principle, it would necessitate multisite direct invasive temperature monitoring, which is inconvenient, harmful, and potentially unethical.

Invasive temperature monitoring reveals a highly inhomogeneous distribution as well as a typical initial delay for both temperature rise and hyperaemia<sup>136–139</sup>.

The requirement for endogenous heat generation techniques led to the study of magnetic fluid hyperthermia (MFH), which involves administering a stable colloidal suspension of biocompatible superparamagnetic iron oxide nanoparticles (SPIONs) in situ, which can be activated by external magnetic fields<sup>140</sup>. The physical foundations and the ability to customize therapies by fine-tuning a few factors are thoroughly described in the literature<sup>141</sup>.

Even in challenging tumors like recurrent glioblastoma and metastatic bone tumors<sup>142</sup>, clinical studies of MFH based on FDA-approved and marketed systems (MagForce® activated by MFH® 300F or NanoActivator®) in combination with RT showed very promising results<sup>143</sup>.

A lot of studies are still looking for new ways to boost the biological effects of the MFH<sup>144</sup>.

In breast cancer cells, magnetic nanobubbles (NBs) containing paclitaxel and coated with Herceptin and ultrasmall superparamagnetic iron oxide were explored for targeted drug delivery and multimodal imaging<sup>145</sup>. Pemetrexed and pazopanib-carrying NBs with magnetic

responsiveness and US sensitivity capabilities have recently been developed as a new theranostic system for non–small cell lung cancer<sup>146</sup>.

The rationale for combining HT and RT is based on some “complementary” effects, such as the fact that tumor cells are more radioresistant when their microenvironment is hypoxic<sup>134</sup> and acidic and when the cell is more sensitive to heat<sup>147</sup>.

Other unintended consequences are far more significant. Heat is less effectively dispersed because of the uneven and leaky structure of the angiogenically driven tumor vasculature, which can both damage the microvasculature and induce local HT<sup>131</sup>. As a result, improved blood circulation reduces hypoxia and raises pH in the environment, temporarily reversing radioresistance (and chemoresistance).

Because tumor oxygenation is one of the main goals of hyperthermic therapy, we looked into using oxygen nanocarriers “decorated” with SPIONs, named magnetic oxygen-loaded nanobubbles (MOLNBs), which combined a magnetic-based temperature increase with a direct oxygenation effect in the tumor volume.

Microbubbles containing oxygen have already been used in sonography as US contrast agents and for oxygen delivery to the hypoxic tumor microenvironment. Nanobubbles are spherical core-shell structures that are filled with gas or vaporizable substances and have dimensions in the nanometer range. Enhanced permeability and retention (EPR) effect was used to improve circulation stability and allow extravasation and accumulation in tumor tissue<sup>148</sup>.

Previously, theranostic polymer-shelled NBs with the ability to operate as drug carriers and US imaging systems have been developed<sup>149</sup>. Our research team had already developed, patented, and proposed oxygen-loaded nanobubbles (OLNBs) for use in other diseases<sup>150</sup>, and preliminary studies on the coupling of SPIONs with OLNBs had also been proposed.

## 3.2. Materials and Methods

### 3.2.1. Materials

Unless otherwise stated, the materials employed were purchased from Sigma-Aldrich (St. Louis, MO, USA). All the reagents were of analytical grade. Epikuron 200® was a kind gift from Cargill.

### 3.2.2. Synthesis of SPIONs

Superparamagnetic iron oxide nanoparticles ( $\text{Fe}_3\text{O}_4$ ) were prepared by using the co-precipitation method. Under continuous nitrogen purging, weighed volumes of  $\text{FeCl}_2 \cdot 4\text{H}_2\text{O}$  (0.99 g) and  $\text{FeCl}_3 \cdot 6\text{H}_2\text{O}$  (2.703 g) was added to deionized distilled water (50 mL) and stirred at  $85^\circ\text{C}$  until dissolved. Then, dropwise, 14 mL of standardized ammonium hydroxide solution was added, followed by 1 hour of stirring at  $85^\circ\text{C}$ . After the system achieved a precipitation state, it was allowed to cool and settle in the flask's bottom. The supernatant liquid is carefully decanted after precipitation is formed to avoid disrupting the precipitation. The precipitate was rinsed with water before being exposed to the air for 24 hours. SPION nanoparticles were obtained and kept at  $4^\circ\text{C}$ . Until the MOLNB preparation is completed. Then, using the electrostatic interaction with the dextran sulfate shell, they were introduced to the produced NB nanosuspension.

### 3.2.3. Preparation of MOLNB formulations

At room temperature, an ethanolic solution of Epikuron 200<sup>®</sup> (1% w/v) and palmitic acid as a cosurfactant (1% w/v) were added to perfluoropentane (PFP,  $\text{C}_5\text{F}_{12}$ ) under stirring. Then, with mild stirring, a volume of ultrapure water was gently added to the mixture until an emulsion was formed. In an ice bath, the system was homogenized for 3 minutes using a high-shear homogenizer (Ultraturrax, IKA, Germany). The nanosuspension was saturated with  $\text{O}_2$  in the aqueous medium until it reached a concentration of 35 mg/L. Then, under oxygen purge, an aqueous solution of dextran sulfate sodium salt (1% w/v) was added drop-by-drop to form the NB polymeric shell. Finally, 1 or 2 mg/mL of SPIONs was added drop-wise to the suspension under mild stirring at room temperature (Figure 3.1).

For the preparation of fluorescent NBs, 6-coumarin was loaded into the NB core by the addition of the fluorochrome directly to the PFP solution. The same preparation protocol used for blank formulations was employed. As a control, blank dextran shelled OLNBS were also prepared, without the addition of SPIONs.

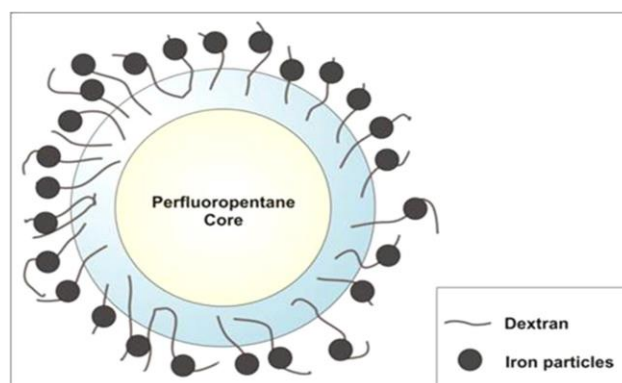


**Figure 3.1:** Sketch of MOLNB structure [dextran NBs covered by Fe<sub>3</sub>O<sub>4</sub> nanoparticles].

### 3.2.4. Physicochemical Characterization of NB Formulations

Photon correlation spectroscopy was used to evaluate the average hydrodynamic diameter, polydispersity index, and zeta-potential values of the NB formulations and SPIONs at a temperature of 25°C and a scattering angle of 90°. Filtered water was used to dilute the samples (1:30 dilution). An average of ten readouts was used to calculate each value. Samples of the NB formulations were placed in the electrophoretic cell of the same equipment for zeta-potential determination. The electric field was set to 14 V/cm. A Ubbelohde capillary viscosimeter (Schott Geräte, Mainz, Germany) was used to evaluate the viscosity of the NB formulation at 25°C. The osmolarity was determined at 25°C using a Knauer osmometer.

Transmission electron microscopy (TEM) in conventional and high-resolution (HR) modes was used to examine the morphology of blank OLNb, MOLNB, and SPIONs using a JEOL2200FS microscope operating at 200 keV. Before observation, the diluted NB aqueous solutions were sprayed on a Firmware-coated copper grid and allowed to air dry.

### 3.2.5. Determination of NB Physical Stability Over Time

Over time, the physical stability of blank OLNb and MOLNB was assessed. The average diameter and shape of NB formulations held at 4°C for up to two months were determined.

### 3.2.6. Ultrasound Imaging Evaluation

The echogenicity of the OLNbs and MOLNBs was investigated using B-mode US imaging. To achieve a homogeneous suspension, a nanobubble aqueous suspension with a concentration of  $\sim 1 \times 10^{10}$  NBs/mL was pipetted into a tank containing demineralized water and gently mixed with a magnetic stirrer. An acoustic absorbing pad was installed at the bottom of the tank to reduce acoustic reflections. The experiment was carried out at three different temperatures:

25°C, 37°C, and 41°C, to mimic room temperature, physiological, and hyperthermic circumstances. A US clinical echo equipment sonograph (MyLab™ 25Gold; Esaote, Genova, Italy) equipped with a linear array transducer (LA523, 7.5 MHz central frequency; Esaote) running in B-mode with the small parts imaging preset insonified nanobubbles. Figure 3.2 depicts a diagram of the experimental setup. B-mode cine loops were recorded with a rising Mechanical Index (MI), i.e., increasing acoustic strength while keeping the imaging setting the same. In the absence of NBs, B-mode cineloops of demineralized water were also obtained as a reference.

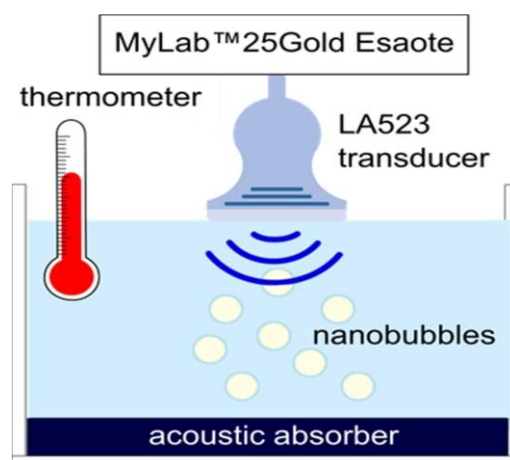


**Figure 3.2:** Experimental setup used for US imaging.

### 3.2.7. Hyperthermic and Magnetic Measurements

Hyperthermia properties were evaluated by calorimetric measurements by means of an AC commercial applicator (nanoScale Biomagnetics DM100, Zaragoza, Spain) Magnetic oxygen-loaded nanobubbles decorated with SPIONs at a concentration of 1 or 2 mg/mL were exposed for 10 min to an RF alternating magnetic field of amplitude = 250 Oe, frequency = 429 kHz. The temperature increase was measured with an optical fiber thermometer to avoid coupling with the RF field. An alternating gradient force magnetometer was used to measure isothermal magnetization curves at room temperature.

### 3.2.8. *In Vitro* Oxygen Release Studies

The dialysis bag technique was used to evaluate *in vitro* oxygen release from MOLNBs in the absence of SPIONs. A dialysis bag was filled with 3 mL of MOLNBs or OLNBs for the donor phase (cellulose membrane, 12 kDa) Then it was immersed in 45 mL of saline solution (NaCl 0.9% w/v) that had had its oxygen concentration lowered (up to 1 mg/L) using a N<sub>2</sub> purge to

simulate hypoxic conditions. Using an oximeter (HQ40d model; Hach), the concentration of oxygen released by diffusion from MOLNBs into the receiving phase was monitored for 24 hours. The in vitro oxygen release kinetics were studied at various temperatures (25°C, 37°C, and 41°C) to simulate ambient and normal body temperatures, as well as hyperthermic sessions. Oxygen release measurements under the effect of the magnetic field were prevented by the metallic nature of the oximetry probe and its interference with the AC applicator.

### 3.2.9. Cell Internalization

TUBO cells, a cloned rat Her<sub>2</sub>/neu+ cell line established from lobular carcinoma of a BALB-neuT mouse, were cultured in high-glucose Dulbecco's modified eagle medium (DMEM), containing 20% fetal bovine serum, 2 mM l-glutamine, and 1% penicillin-streptomycin in a humidified CO<sub>2</sub>/air incubator at 37°C. For NB uptake evaluation, TUBO cells were plated in 6-well plates on glass coverslips and incubated in DMEM medium for 24 h with/without 10% vol/vol 6-coumarin-labeled NBs in a humidified CO<sub>2</sub>/air incubator at 37°C. After 24-h incubation with 6-coumarin-labeled NBs, TUBO cells were fixed, stained with 4',6-diamidino-2-phenylindole (DAPI) to visualize cells nuclei, and then visualized by microscope. Fluorescence images were acquired by an LSM710 inverted confocal laser scanning microscope (Carl Zeiss, Oberkochen, Germany) equipped with a Plan-Neofluar 63 × 1.4 oil objective, which allowed a field view of at least five cells. A wavelength of 488 nm was used to detect fluorescent OLNBS and 460 nm to detect the labeled nuclei. The acquisition time was 400 ms.

### 3.2.10. Statistical Analysis

Data are expressed as means ± SD. Significance between experimental groups was determined by one-way analysis of variance followed by the Bonferroni multiple comparisons posttest using GraphPad InStat software (San Diego, CA, USA).  $p \leq 0.05$  was considered significant.

## 3.4. Results

### 3.4.1. Physicochemical Characterization of NB Formulations

Decorated SPIONs and oxygen-loaded NBs were manufactured using biocompatible components, tuning the preparation protocol, which was previously reported<sup>151</sup>. The

physicochemical parameters of OLNBs before and after the addition of SPIONs are reported in Table 3.1. The zeta-potential of SPIONs was +11.63 mV. The positive charge is suitable for obtaining a binding on the negative polymer shell by electrostatic interactions. The presence of SPIONs on the polymer shell produced a decrease of the MOLNB zeta potential of about 30%. This behavior can be related to the electrostatic binding of SPIONs and the partial shielding of the surface charge of NBs.

The pH of the NB nanosuspension was 5.86, the viscosity was about 1.42 cP, and the osmolarity was 354 mOsm, values suitable for future clinical translation. These parameters were not affected by the presence of the SPIONs. Moreover, the nanosuspension was homogeneous and stable over 2 months.

Figure 3.3 shows the TEM images of both SPIONs (Figure 3.3A) and blank dextran-shelled OLNBs (Figures 3.3B, C). The spherical and hollow morphology of the NBs is clearly visible in the images. The TEM studies of functionalized nanobubbles (MOLNBs) revealed a more contrasted shell with respect to OLNBs, maintaining the classic spherical shape, as shown in Figure 3.4A. By progressively increasing the magnification, the “granular” structure of the SPIONs in the shell becomes evident (Figures 3.4B, C). An average diameter of about 390 nm was confirmed for MOLNBs. Fluorescent OLNBs were visible under a fluorescence microscope and the morphology and physicochemical properties were the same as previously described. In vitro stability studies showed that the nanosuspension was homogeneous and stable over 2 months. **Table 3.1:** Physicochemical characteristics of NB formulations.

<b>Formulation</b>	<b>Average diameter ± SD (nm)</b>	<b>Polydispersity Index</b>	<b>Zeta Potential ± SD (mV)</b>
<b>Blank OLNBs</b>	375.5 ± 20.4	0.21 ± 0.01	-30.4 ± 3.45
<b>Fluorescent OLNBs</b>	378.2 ± 26.3	0.21 ± 0.01	-28.8 ± 3.68
<b>MOLNBs</b>	385.4 ± 25.8	0.19 ± 0.02	-19.72 ± 1.24



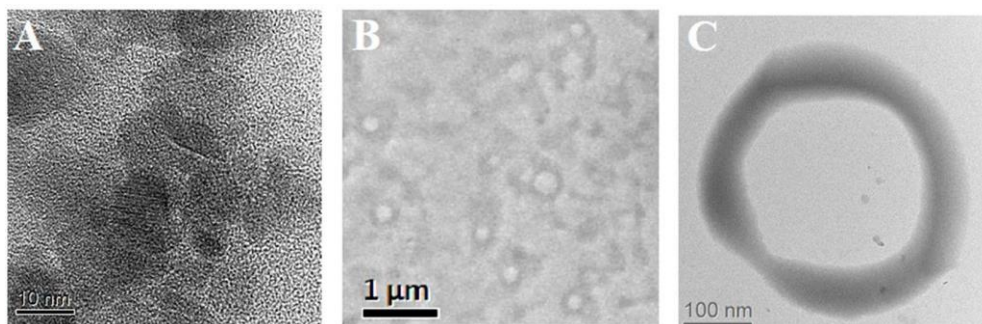


**Figure 3.3** (A) HRTEM image of SPIONs; (B, C) TEM images of blank-shelled OLNBs at different magnifications.

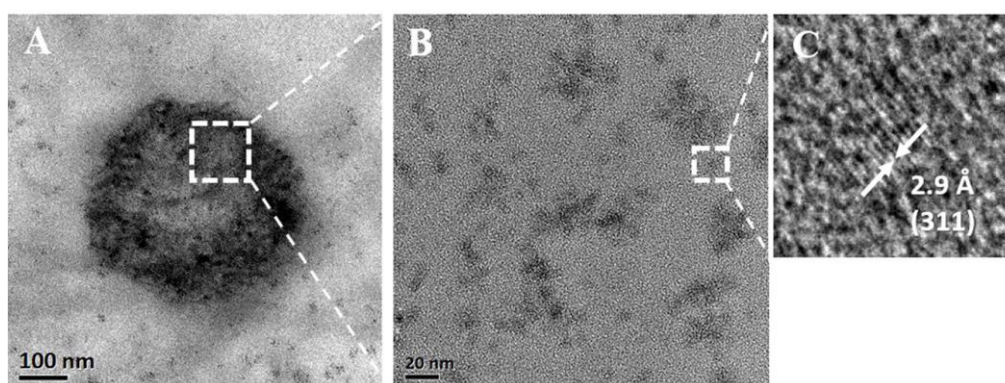


**FIGURE 3.4** (A) TEM image of a MOLNB; (B) HRTEM image of the square region in (A); (C) HRTEM image of the square region in (A) showing the (311) lattice planes of a Fe<sub>3</sub>O<sub>4</sub> nanoparticle.

### 3.4.2. Ultrasound Imaging Evaluation

Ultrasound experiments revealed that MOLNBs showed an increased echogenicity with respect to OLNBs (Figure 3.5). The ability of both the OLNBs and MOLNBs to generate an echogenic response was enhanced at 37°C, as visually demonstrated. The insonation affected the detectability increasing the volume size of NBs favouring the vaporization, due to acoustic droplet vaporization (ADV) phenomenon<sup>152</sup>. A decrease in the echogenicity was observed at 41°C, probably because most of the NBs showed a different vaporization behavior. We could speculate that this could be related to the phase transition of phospholipids (i.e., phosphatidylcholine) present in OLNBs from the gel to the liquid crystalline state. This effect was previously observed also for Sonovue® (Bracco, Italy), a commercial US contrast agent consisting of microbubbles loaded with SF<sub>6</sub> and coated with a phospholipidic shell<sup>153</sup>.

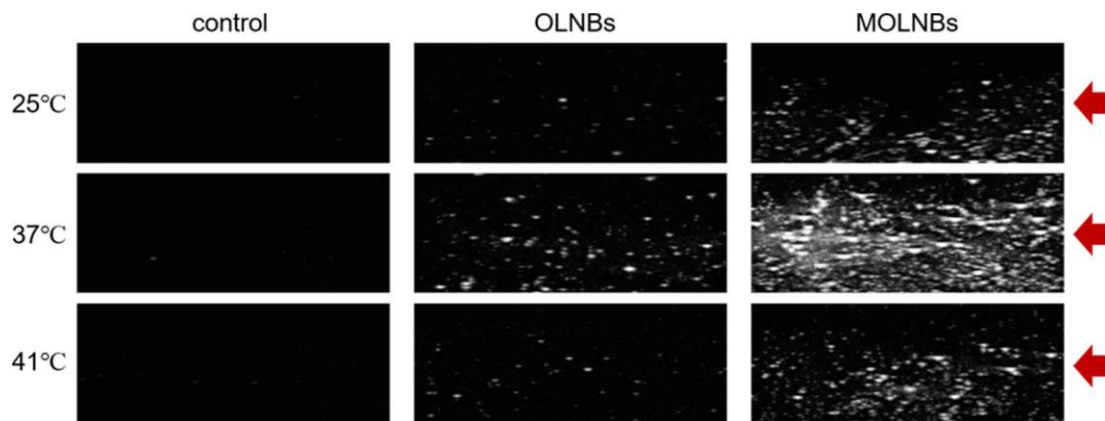


**Figure 3.5:** Snapshots of the B-mode cineloops of control experiment (demineralized water only), OLNBs, and MOLNBs at MI = 1.1 (i.e., maximum acoustic power) and different temperatures. Red arrows indicate the focus of the US probe.

### 3.4.3. Hyperthermic and Magnetic Measurements

A first simulation of the hyperthermic session was performed by exposing for 10 min a colloidal suspension of MOLNBs to an RF magnetic field. A temperature increase of the sample was observed during the RF field application. In Figure 3.6, the time dependence of the suspension temperature under irradiation is reported for two different NB concentrations. After 10 min of exposure, a temperature increase of 5°C (at field amplitude of 250 Oe) or 7°C (at field amplitude of 300 Oe) for the 2 mg/mL SPION concentration was attained. The specific heat absorption rate (SAR), expressed in W/g, was evaluated by using the following expression (Eq. 1):

$$SAR = \frac{c\rho}{c} \frac{dT}{dt} \quad (1)$$

where  $c$  is the specific heat capacity of the sample (for diluted solutions as in the present case,  $c$  is equal to the heat capacity of the solvent, assumed to be 4.18 J/g °C),  $\rho$  is the density of the solvent (equal to 1 g/mL),  $C$  is the concentration of the magnetic NB in the solvent (2 g/L), and  $dT/dt$  is the heating rate of the sample. The heating rate was calculated by fitting the temperature increase  $\Delta T$  with a linear trend at early times, i.e., the first 10 seconds of the experiment. Depending on the field amplitude, the SAR values range between 37.7 and 46.1 W/g.

The deviation from the linearity at longer times of the temperature increase is dictated by the combined effects of heating power and thermal losses. The temperature increase of the

solution can be attributed to the magnetic properties of MOLNBs, as confirmed by room temperature isothermal magnetization measurements. In Figure 3.7, hysteresis loop measurements are reported, confirming the superparamagnetic behavior of magnetic NBs, characterized by no remanence and no hysteresis.

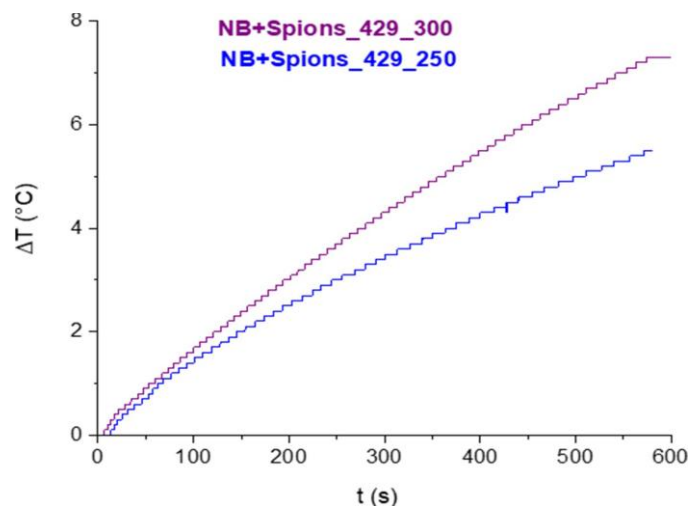


**Figure 3.6:** Variation of temperature as a function of time under exposure of RF magnetic field for two different AC field amplitudes.

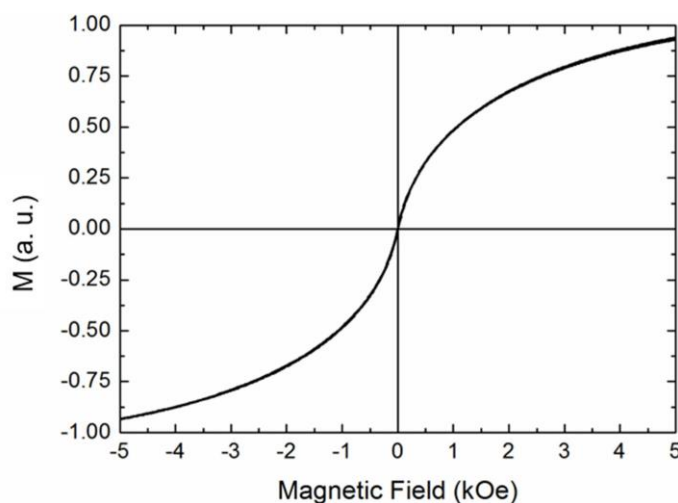


**Figure 3.7:** RT magnetization curve for MOLNBs.

#### 3.4.5. *In Vitro* Oxygen Release

The release studies showed the capability of OLNBs and MOLNBs to store and release oxygen. The *in vitro* oxygen release kinetics from MOLNBs into a hypoxic receiving phase showed a biphasic profile (Figure 3.8). In the first 4 h, oxygen was rapidly released from MOLNBs, reaching an oxygen concentration between about 4 and 6 mg/L at 25°C and 41°C, respectively.

Subsequently, an almost constant and slow oxygen release was obtained. After 24 h, the oxygen concentration in the external receiving phase kept constant, because an equilibrium between the internal and external phases was reached. A temperature-dependent release profile was observed. The presence of SPIONs on the NB shell did not affect the oxygen release capability. Indeed, the same *in vitro* release profiles were obtained for OLNBs at all temperatures.

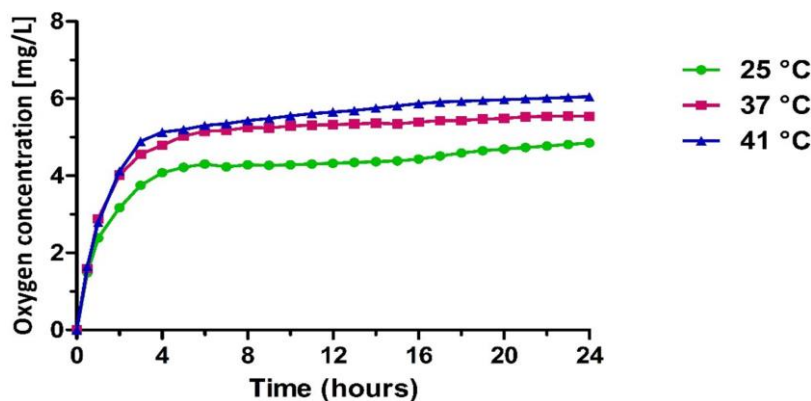


**Figure 3.8:** In vitro oxygen release from MOLNBs at different temperatures (i.e., 25°C, 37°C, and 41°C).

#### 3.4.6. Cell Internalization

Fluorescence microscopy was used to verify if NBs were internalized by the breast cancer *in vitro* model. Results show that NBs were avidly internalized by TUBO cells and were localized only in the cellular cytoplasm compartment (Figure 3.9). This result indicates that MOLNBs were able to deliver a gas or a drug directly inside the cancer cells.

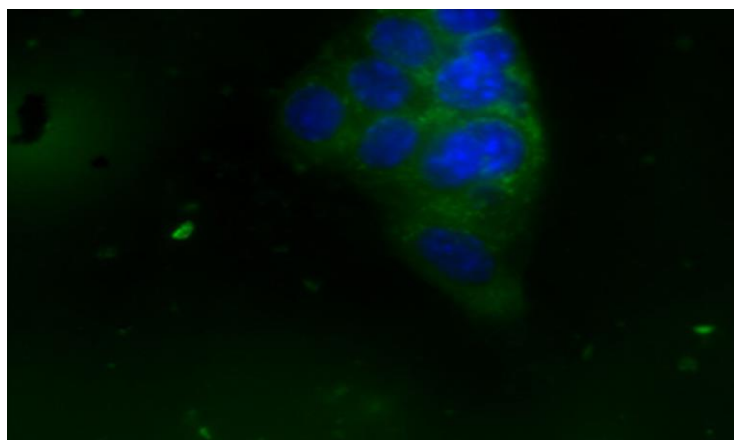


**Figure 3.9:** OLNb internalization by TUBO cell line. Cell nuclei after DAPI staining (in blue; OLNbs, in green). Magnification  $\times 63$ .

### 3.5. Discussion

In comparison to microbubbles, drug-loaded NBs showed an increase in drug blood lifetime, extravasation capability, and accumulation in tumors by passive targeting, exploiting the EPR effect<sup>148</sup>. To store and transport oxygen in hypoxic tissues, oxygen-loaded nanobubbles have been produced. Due to their theranostic feature, oxygen-loaded nanobubbles are also particularly appealing nanocarriers for their prospective application in cancer therapy. Furthermore, they could be used as a radiosensitizer. In RT, where the oxygen's enhancing effect is well known. Magnetic oxygen-loaded microbubbles have been reported in the literature. previously described for the dual-modality treatment of tumor hypoxia, showing enhanced antitumor effects<sup>154,155</sup>. The functionalization of OLNBs is discussed here. The use of SPIONs to obtain MOLNBs has been reported. This new specific nanoscaled carrier was demonstrated to be effective as a locally hyperthermic agent in vitro studies.

According to TEM examination, magnetic oxygen-loaded nanobubbles have a well-defined hollow structure with a shell densely decorated by SPIONs. The electrostatic interaction between the positive SPION charge and the negative surface charge of dextran sulfate-shelled NBs is strong enough to form a stable nanostructure.

The preliminary hyperthermic investigations of this work confirmed that MOLNBs might be a promising new theranostic MFH agent, presenting the additional advantages of delivering oxygen to cancer cells and allowing their imaging detection.

Interestingly, under RF magnetic field, MOLNBs manufactured with a SPION concentration of 2 mg/mL produced a temperature increase as large as 5°C at field amplitude of 250 Oe and 7°C at 300 Oe, after 10 minutes of treatment. The calculated SAR values of MOLNBs demonstrated a good heating efficiency and were comparable with those recently obtained by<sup>156,157</sup>.

The magnetic and hyperthermic properties can be possibly related to the small dimensions of the SPIONs and the average number of SPIONs that decorated the OLNb shell. As a matter of fact, preliminary investigations by Albertini et al. showed that the thermic effect can be related to the presence of SPION clusters, reaching higher temperatures in the presence of increased SPION agglomeration (personal communication). Therefore, based on these results,

MOLNBs could represent an innovative multitheranostic approach for hyperthermic treatment.

In addition, *in vitro* oxygen supply from MOLNBs was found to be significant and persistent. In contrast to OLNBs, the presence of SPIONs on the NB shell had no effect on the oxygen release kinetics.

The difference in gas concentration between the core and the exterior environment controls the amount of oxygen released by NBs by passive gas diffusion across the shell. Interestingly, the MOLNB core, being composed of PFP in which oxygen has a very high solubility, can act as a gas reservoir from which oxygen can be slowly released with kinetics depending on its partial pressure, according to Henry law. Furthermore, the high internal NB pressure, which is inversely associated with the bubble radius according to the Laplace rule, must be taken into consideration for the oxygen release kinetics.

Furthermore, the oxygen delivery from MOLNBs could be tuned for specific hyperthermic treatment by modulating the nanostructure of the nanocarriers, i.e., shell thickness and particle diameter.

According to Figure 3.8, a sustained rise in oxygen release over time is caused by a temperature increase in the hyperthermic region, resulting in an oxygen concentration increase of around 0.5 mg/L in the external aqueous solution. This impact could be linked to changes in shell permeability caused by changes in the MOLNB nanostructure. Phospholipids did, in fact, go through a sol-gel-sol transition as a function of temperature. In addition to the physiological mechanisms connected to heat-induced hyperemia, long-term oxygen release in heated biological tissues may be expected and would contribute to their oxygenation.

Unfortunately, we were unable to directly record the oxygen delivery in the presence of a magnetic field. Indeed, direct measurements were prevented when MOLNBs were in such conditions, due to the metallic composition of the oximetry probe. In our experimental setup, the oxygen concentration was measured just after the withdrawal of the sample from the magnetic field. We observed that the sustained *in vitro* oxygen release profile was maintained also after irradiation. This might indicate the integrity of the NB structure. The occurrence of mechanical modifications of the MOLNB shell following the interaction with the RF magnetic

field could be excluded because no massive oxygen delivery after the hyperthermic session was observed.

The MOLNBs' theranostic character was confirmed by US imaging, which revealed the system's echogenicity. The contrast created by OLNBs and MOLNBs is the same for each. B-mode imaging increased when the temperature increased from room to body temperature. The echogenicity of NB is related to the droplet-to-bubble phase transition.

Indeed, PFP-loaded NBs present the ability to be activated by the US, by means of a phenomenon called Acoustic droplet vaporization. ADV allows nanodroplets to be converted into bubbles following a US pulse, inducing the liquid-to-gas transition within the bubble core. However, the MOLNBs revealed an enhanced acoustic contrast with respect to OLNBs, probably depending on the difference in compressibility and density with respect to water. Finally, *in vitro* biological studies confirmed that MOLNBs can be easily internalized by tumor cells, and no cytotoxic effects were observed.

### 3.6. Conclusions

In a cancer cellular model, we produced and analyzed superparamagnetic theranostic OLNBs with echogenicity, heating potential, and internalization capability. Magnetic oxygen-loaded nanobubbles could be a novel fascinating nanotool for multifaceted tumor treatment, generating HT and releasing oxygen as a radiosensitizer for RT when exposed to an RF magnetic field. This nanoformulation could offer a new way to improve cancer treatment outcomes by allowing cancer cells to be killed locally by heating tumor tissues to hyperthermic temperatures.

## Chapter 4:



*Article*

# **Beyond Oncological Hyperthermia: Physically Drivable Magnetic Nanobubbles as Novel Multipurpose Theranostic Carriers in the Central Nervous System**

Eleonora Ficiarà <sup>1,\*</sup>,<sup>†</sup>,<sup>ORCID</sup> Shoeb Anwar Ansari <sup>1</sup>,<sup>†</sup>, Monica Argenziano <sup>2</sup>, Luigi Cangemi <sup>2</sup>,  
Chiara Monge <sup>2</sup>, Roberta Cavalli <sup>2</sup> and Federico D'Agata <sup>1</sup>,<sup>ORCID</sup>



#### 4.1. Introduction

Magnetic nanocarriers have been extensively investigated as hyperthermic agents in combination with radiotherapy to treat superficial and deep tumors<sup>158–160</sup>. In particular, Magnetic Fluid Hyperthermia (MFH) consists of the in-situ administration of a stable colloidal suspension of biocompatible Superparamagnetic Iron Oxide Nanoparticles (SPIONs) which can produce endogenous heat generation following activation by external magnetic fields<sup>161</sup>. Clinical applications of MFH have been approved by the Food and Drug Administration (FDA) and are already marketed (MagForce<sup>®</sup> activated by MFH<sup>®</sup> 300F or NanoActivator<sup>®</sup>).

As tumor oxygenation is one of the main targets of the hyperthermic treatment, our group investigated the use of oxygen carriers “decorated” by SPIONs as hyperthermic agent<sup>162</sup>, showing that in addition to heating (temperature increase of some C could be reached already at the low magnetic field) such Magnetic Oxygen-Loaded Nanobubbles (MOLNBs) are easily internalized by cells, do not produce toxic effects, deliver oxygen in a sustained way, and can be monitored either by using clinical Ultrasound (US) sonography and by Magnetic Resonance Imaging (MRI)<sup>162</sup>.

In the present study, we further investigated MOLNBs looking at possible applications besides hyperthermia, i.e., magnetic driving and delivery systems.

In particular, the attention was focused on the quantitative methods for engineered nanoparticles to cross brain barriers and to effectively target the Central Nervous System (CNS)<sup>163</sup>. Various chemical and physical approaches have been proposed to satisfy the requirement for effective therapy and imaging<sup>161,163,164</sup>.

As a matter of fact, magnetic nanoparticles have already been proposed to bypass the Blood-Brain Barrier (BBB) to treat glioblastomas and neurodegenerative diseases<sup>165–169</sup> as well as in regenerative medicine and drug delivery<sup>170,171</sup>. Very recently magnetic nanoparticles have been proposed as transducers in advanced neuromodulation, via the hysteretic heat when exposed to alternated magnetic fields<sup>172</sup>.

We propose MOLNBs as a new theranostic application for the treatment of cerebral tumors, based on their ability to carry oxygen (a well-known radiotherapy enhancer) and a proper load of chemotherapy drugs (doxorubicin and possibly temozolomide)<sup>173</sup>. Indeed, we speculate that they can be locally delivered to the Cerebro-spinal Fluid (CSF) by spinal

injection, magnetically driven towards the part of the choroid plexus anatomically most proximal to the tumor mass where the drug and oxygen cargoes are delivered after crossing the barrier from the CSF to the brain interstitial fluids.

Previous imaging by Computed Tomography (CT) and/or MRI can guide the tailoring of the magnetic field required for optimal driving to the tumor, whereas post-treatment imaging by MRI and US (when the skull does not shield the target) allows the monitoring of the MOLNBs final concentration.

To assess the feasibility of this innovative delivery approach we investigated whether such nanocarriers are safe, biocompatible, not cytotoxic, and not hemolytic (in case of systemic administration or possible interactions with blood). In addition, we evaluated their internalization capability by human brain microvascular endothelial cells (hBMECs) and, finally, if we can drive the MOLNBs using proper magnetic fields, which is known to be a weakness of all the similar procedure<sup>174</sup>.

Accordingly, together with a specific assessment of the physicochemical and biocompatibility properties of the MOLNBs, their response to the external magnetic field produced by a permanent magnet has been investigated via ultrasonic imaging.

## 4.1. Materials and Methods

### 4.1.1. Materials

All reagents were of analytical grade and obtained from Sigma-Aldrich (St. Louis, MO, USA) unless otherwise specified. Epikuron 200<sup>®</sup> was kindly provided by Cargill.

### 4.1.2. Methods

#### 4.1.2.1. Synthesis of SPIONs

Fe<sub>3</sub>O<sub>4</sub> nanoparticles were synthesized by a co-precipitation method. In a typical synthesis, 0.99 g of FeCl<sub>2</sub> 4H<sub>2</sub>O and FeCl<sub>3</sub> 6H<sub>2</sub>O was dissolved in 50 mL of degassed deionized distilled water in a conical flask and the temperature was moderately increased to 85°C under continuous nitrogen purging and stirring at 700 rpm for 45 min. Then, 20 mL of ammonia solution 30% was added dropwise to the reaction mixture, and after pH reached 12 the reaction was followed by stirring at 85°C for 1 h. After the system reached a precipitation state, it was allowed for cooling and settling of the precipitation at the bottom of the flask at room temperature. The black coloured precipitates were separated from the supernatant by

using a permanent magnet. The precipitate was rinsed with distilled water and allowed to expose in air for 24 h.

#### 4.1.2.2. Preparation of MOLNBs Formulations

Epikuron 200® (2.5% w/v) and palmitic acid as a co-surfactant (0.5% w/v) were dissolved in ethanol. 300 µL of the mixture was added to perfluoropentane (PFP, C<sub>5</sub>F<sub>12</sub>) in an ice bath. Then the appropriate volume of distilled water was added dropwise to the mixture. The system was homogenized for 2 min by using a high-shear homogenizer (Ultra-Turrax®) until the formation of a nanoemulsion. Thereafter, the nanoemulsion was saturated with O<sub>2</sub> for 10 min. Then, an aqueous solution of dextran sulfate sodium salt (2% w/v) was added dropwise to form the nanobubbles (NB) polymeric shell under an oxygen purge. Finally, 2 mg/mL of SPIONs suspension were added to NB under stirring, to obtain MOLNBs (see Figure 4.1).

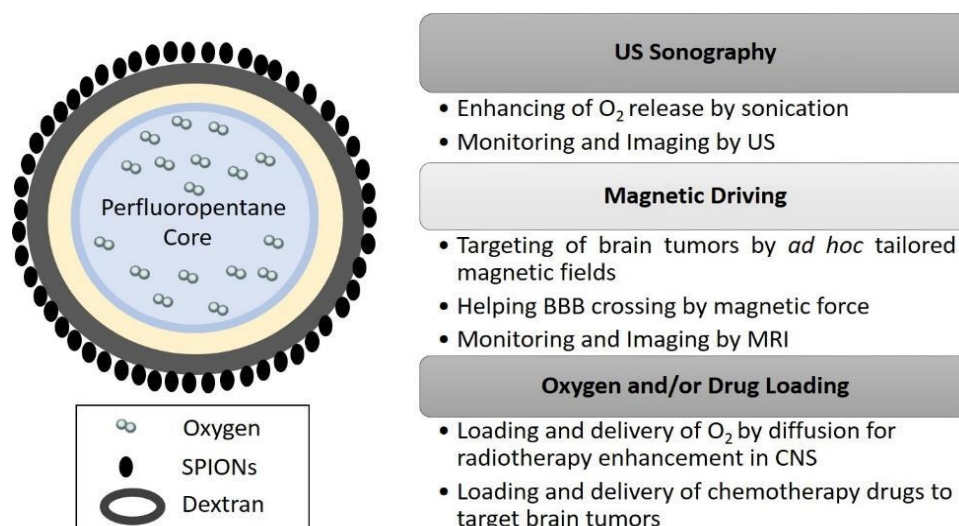


**Figure 4.1.** Sketch of MOLNBs (dextran NB covered with Fe<sub>3</sub>O<sub>4</sub> nanoparticles, not to scale) and relative multifunctional applications as a theranostic system in CNS.

For the fluorescent nanocarriers, 6-Coumarine (Sigma-Aldrich) was loaded into the MOLNBs core upon the addition of the fluorochrome directly to perfluoropentane solution. As a control, blank dextran shelled-OLNBs were also prepared, without the addition of SPIONs.

#### 4.1.2.3. Physicochemical Characterization of MOLNBs

The mean hydrodynamic diameter, polydispersity index (PDI), and zeta potential of the SPIONs and MOLNBs were measured by dynamic light scattering spectroscopy (DLS) at room temperature. The samples were diluted with ultrapure water in an electrophoretic cell. Each

measured value was the average of ten reciprocal, an electric field of 15 V/m was used for zeta potential determination. Photon correlation spectroscopy (PCS) with a scattering angle of 90°, the temperature of 25°C using a 90 Plus instrument (Brookhaven, NY, USA) was used. The viscosity of the NBs formulation was determined at 25°C using a capillary viscosimeter. The osmolarity was determined at 25°C using an osmometer. The morphology of MOLNBs was observed by Transmission Electron Microscopy (TEM) in conventional mode, by using a JEOL2200FS microscope. The diluted NB aqueous suspensions were sprayed on the Formwar-coated copper grid and air-dried before observation.

#### 4.1.2.4. Physical Stability of MOLNBs

The physical stability of blank OLNBs and MOLNBs was evaluated for up to 12 weeks. The parameters monitored for stability were average size distribution and surface morphology (shape of bubbles visualized by using microscopy) of the stored NB formulations at 4°C.

#### 4.1.2.5. Determination of Haemolytic Activity

The haemolytic activity of MOLNBs was evaluated on rat blood. Blood was diluted at 1:10 with PBS (pH 7.4). Triton X 1% was used as a positive control, where red blood cell breakage and further release of haemoglobin occurred. Saline solution (NaCl 0.9% w/v) was used as negative control. 1 mL of all samples were prepared (1:10, 1:100, 1:200, 1:400 dilution) and incubated for 90min at 37 °C. Then, samples were centrifuged for 5 min at 2000 rpm and the supernatant was analyzed with an ultraviolet-visible spectrophotometer (DU 730, Beckman Coulter, Fullerton, CA) at  $\lambda = 543$  nm. The percentage of haemolysis was calculated using the positive control as 100% haemolysis.

#### 4.1.2.6. Evaluation of MOLNBs Internalization by Human Brain Microvascular Endothelial Cells

Human brain microvascular endothelial cells (hBMECs), provided from Cell Systems (Kirkland, WA, USA), were cultured in EndoGRO Complete Medium (Merck Millipore), plated in 24-well plates on a glass coverslip ( $5 \times 10^4$  cells per well), and incubated for 4h in a 500 $\mu$ L of medium with/without MOLNBs and OLNBs (dilution 1:100 and 1:200) internalized with 6-Coumarine (Sigma-Aldrich) in a humidified CO<sub>2</sub>/air-incubator at 37°C. Fixing was carried out by adding 500 $\mu$ L of cold paraformaldehyde (PFA, 4%) and by incubating for 15 min at room temperature and rinsing the excess PFA with sterile PBS. After fixing, 40,6-diamidino-2-phenylindole (DAPI)

and Rhodamine-Phalloidin (R415, Invitrogen., Thermo Fisher Scientific, MA, USA) staining reactions were performed to label cells nuclei and the actin filaments. Fixed cells were kept at 4°C for 24 h and fluorescence images were acquired by a confocal laser scanning microscope (LSM 900, Carl Zeiss, Oberkochen, Germany) equipped with a 40X oil immersion objective, obtaining a field view of at least 5 cells. A wavelength of 505 nm was used to detect MOLNBs and OLNBs, of 565 nm and 460 nm to detect respectively the actin filaments and the nuclei. Images were processed using the software ImageJ (<https://imagej.nih.gov/ij/>).

#### 4.1.2.7. In Vitro Cytotoxicity Study

The hBMECs cells were used to perform in vitro cytotoxicity test. Cells (800/well) were seeded in 96-well plates and incubated at 37°C, 5% CO<sub>2</sub> for 24 h in EndoGRO Complete Medium. Then, the cells were treated with OLNBs, SPIONs, MOLNBs, in two different dilutions with medium (1:100 and 1:200). After 72 h incubation, viable cells were evaluated by 2,3-bis [2-methoxy-4-nitro-5sulphophenyl]-2Htetrazolium-5carboxanilide (MTT) inner salt reagent at 570 nm, as described by the manufacturer's protocol. The control cells were normalized to 100%, and the readings from treated cells were expressed as a percent of cell viability. Eight replicates were used to determine each data point and four different experiments were performed.

#### 4.1.2.8. US Imaging Monitoring

B-mode US imaging was carried out to investigate the response of MOLNBs to the external magnetic field due to their excellent echogenicity. MOLNBs at concentration  $1 \times 10^{10}$  NB/mL were injected in a plastic tank containing demineralized water by means of a syringe positioned as indicated in Figure 4.2. The plastic tank was made by 3D printer to obtain the dimensions  $7.5 \times 2 \times 3 \text{ cm}^3$  to well fit with the probe dimension. A sketch of the setup is shown in Figure 4.2a. The experiment was performed at a temperature of 20 °C. MOLNBs were sonicated by an US clinical equipment (MyLab.25Gold Esaote, Genova, Italy), connected to a linear array transducer (LA523, 7.5 MHz central frequency, Esaote, Genova, Italy) operating in B-mode using the small parts imaging preset. B-mode cineloops (60 sec) were acquired and recorded for postproduction both in the absence and in the presence of the permanent magnet exerting a magnetic force in the direction of injection (see Figure 4.2b). Snapshots from cineloops were extracted at different time frames (5, 15, 25, 55 sec) after the initial injection and compared in different conditions.

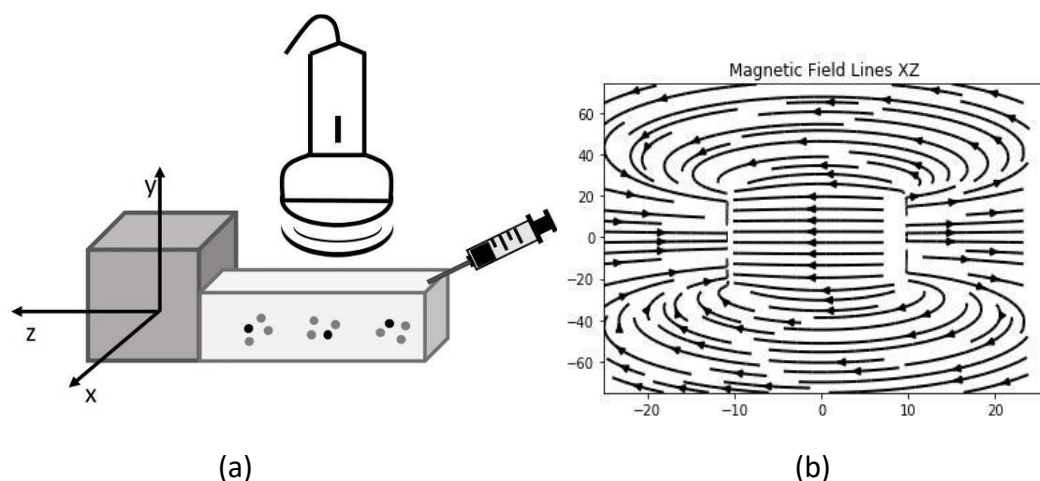


**Figure 4.2:** (a) A sketch of the setup used for the imaging of MOLNBs in the absence and presence of the magnetic field produced by the cuboid magnet. (b) Projection of magnetic field lines in the XZ plane is assessed by the z-direction of the magnetic field.

## 4.2. Results

### 4.2.1. Physicochemical Characterization of MOLNBs Formulations

The physicochemical characterization of OLNBs and MOLNBs is reported in Table 4.1. The negative value of the zeta potential is the fingerprint of dextran sulfate on the NB surface. The average zeta potential of SPIONs was measured to be +16.24 mV. The positive charge of SPIONs is appropriate for binding with negatively charged dextran sulfate polymer shells by electrostatic interactions. After binding of SPIONs, the polymer shell surface reduced its zeta potential by 45%. Other specific parameters of the OLNBs nanosuspension such as pH, viscosity, and osmolarity were 6.52, 0.98 cP, and 354 mOsm, respectively. These parameters were not affected by the presence of SPIONs on the NB surface. Furthermore, OLNBs showed homogenous size and stability over 3 months.

**Table 4.1.** Physicochemical characteristics of different nanocarriers formulations. Data reported as Mean  $\pm$  Standard Deviation.

Formulation	Average Diameter (nm)	Polydispersity Index	Zeta Potential (mV)
Blank OLNBs	331.6 $\pm$ 19.7	0.22 $\pm$ 0.10	-35.36 $\pm$ 4.16
Fluorescent OLNBs	338.2 $\pm$ 13.8	0.24 $\pm$ 0.08	-34.24 $\pm$ 6.52
MOLNBs	349.2 $\pm$ 18.2	0.21 $\pm$ 0.01	-20.41 $\pm$ 8.60

TEM images both of SPIONs and MOLNBs were acquired at different magnification. The TEM images of MOLNBs showed a spherical and hollow morphology, with a well-contrasted shell, as shown in Figure 4.3a. An average diameter of about 350 nm was detected for MOLNBs, confirming DLS measurements. The SPIONs structure is reported in Figure 4.3b, showing sizes ranging from 5 to 30 nm.

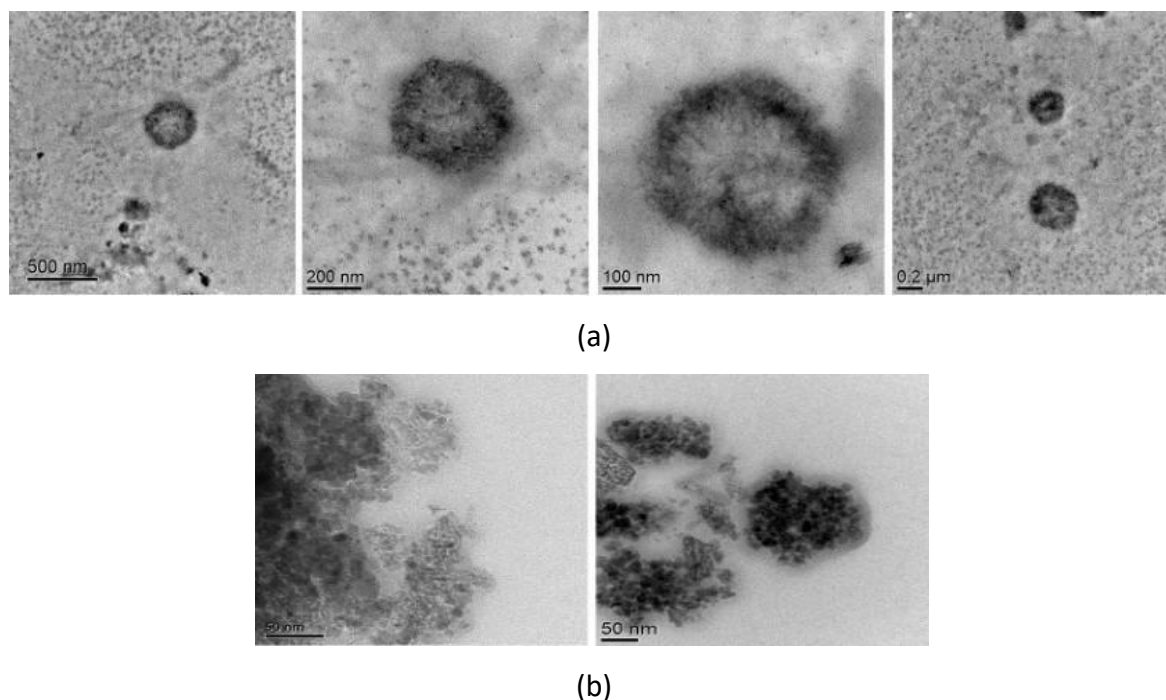


**Figure 4.3.** (a) TEM images of MOLNBs at different magnification. (b) TEM images of SPIONs.

#### 4.2.2. Haemolytic Activity

MOLNB aqueous suspensions tested at different dilutions (1:10, 1:100, 1:200, 1:400 v/v) did not present significant haemolytic activity, showing no red blood cell damage in comparison with control. These data suggest that this nanoformulation is biocompatible and suitable for potential in vivo administration without any haemolytic problems.

#### 4.2.3. Evaluation of MOLNBs Internalization and Toxicity

Confocal microscopy was used to verify whether MOLNBs were internalized by hBMECs. Images showed that MOLNBs, as well as OLNBs, were significantly internalized by hBMECs (Figure 4.4). Cytotoxicity studies underlined the very good viability of hBMECs after the treatment with SPIONs, MOLNBs, and OLNBs (Figure 4.5).

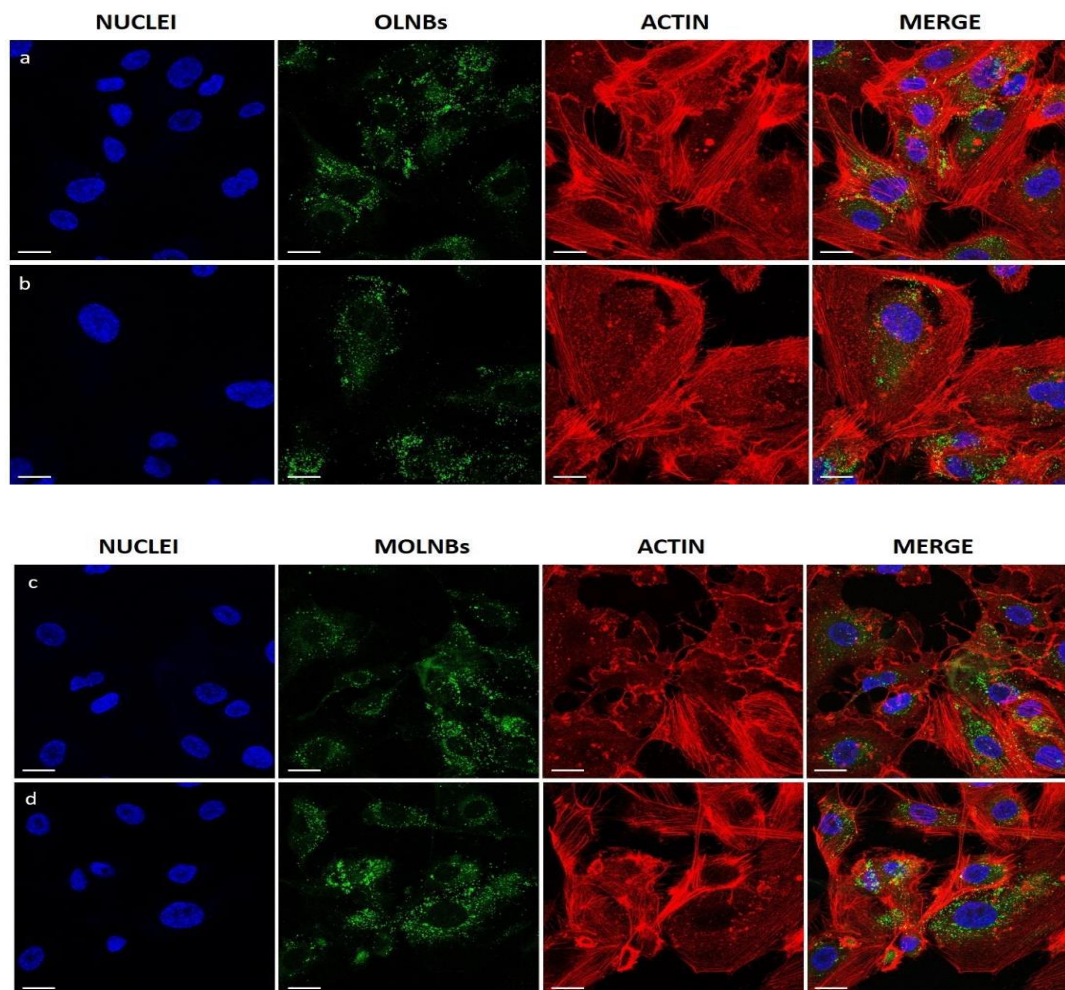


**Figure 4.4:** Confocal images of different formulations of nanocarriers internalized by hBMECs after 4 h of incubation. First and second rows: cells were treated with blank OLNBs (without SPIONs) in a dilution ratio of 1:100 (a) and 1:200 (b) with the medium. Third and fourth rows: cells were treated with MOLNBs in a dilution ratio of 1:100 (c) and 1:200 (d) with the medium. First Column: cell nuclei after DAPI staining, in blue. Second column: OLNBs and MOLNBs, conjugated with 6-Coumarine, in green. Third column: cell actin filaments after Rhodamine-Phalloidin staining, in red. Fourth column: merged images. Magnification: 40x. Calibration bar = 20  $\mu\text{m}$ .



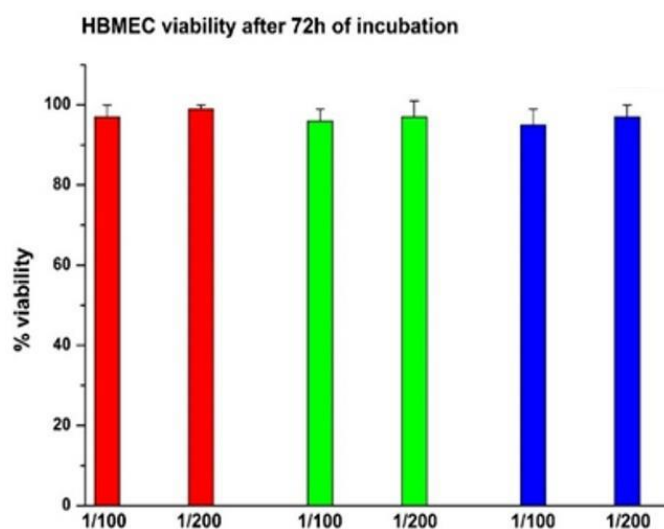


**Figure 4.5:** Percentage of viable cells after 72 h of incubation. The horizontal axis indicates the dilution (1:100 and 1:200) of NB. Red = MOLNBs; Green = SPIONs; Blue = OLNBs.

#### 4.2.4. US Monitoring of MOLNBs in the Magnetic Field

The motion of the MOLNBs, located along the negative z-direction of the coordinate system, centered in the magnet, whose corresponding magnetization of the MOLNBs is dominated by the component along the z-axis, is significantly affected by the field. Snapshots at different time intervals from US imaging showed a different distribution of MOLNBs in the absence and the presence of the magnetic field, which exerted a sensible effect driving a detectable motion toward the magnet and along the axis (see Figure 4.6).

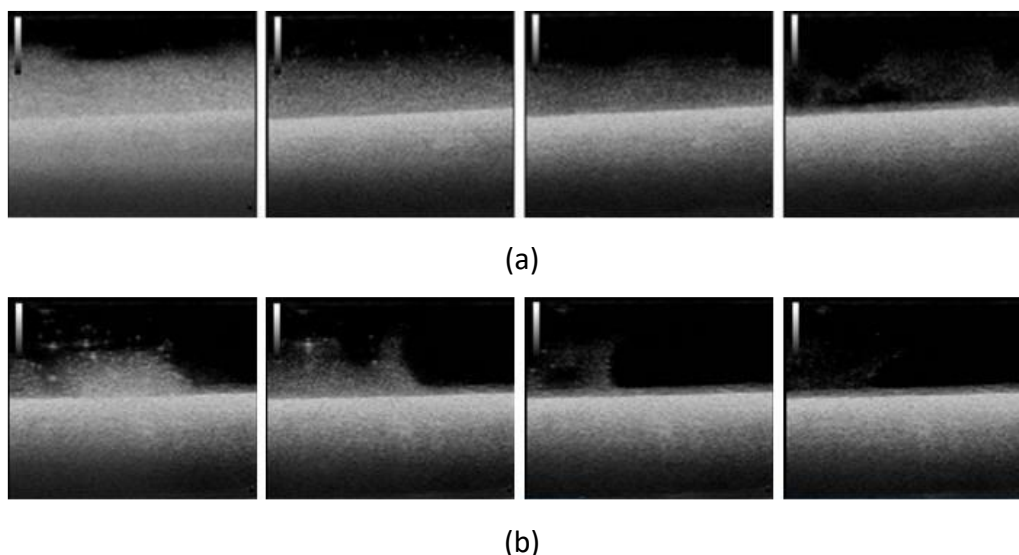


**Figure 4.6:** Snapshots from US imaging of MOLNBs in the absence (a) and presence (b) of the magnetic field. Images were recorded at different time frames (5, 15, 25, 55 sec) from the injection.

#### 4.5. Discussion

MOLNBs are stable nanosystems showing a well-defined hollow structure, whose shell is densely decorated by SPIONs, as indicated by TEM analysis. The addition of SPIONs does not significantly increase neither their average diameter nor the polydispersity index, while the zeta potential is decreased but the value is still effective in preventing aggregation phenomena. This behaviour suggested a good electrostatic interaction of SPIONs with the negatively charged NB shell. The combination of SPIONs with NB forming stable nanosystems was previously reported<sup>175</sup>.

Furthermore, the surface negative charge makes MOLNBs promising candidates to efficiently cross the BBB, being the zeta potential a crucial parameter for brain delivery<sup>176–178</sup>. MOLNBs were able to store in the perfluorocarbon core and slowly release oxygen by passive diffusion gradient, as previously evaluated<sup>162</sup>. The oxygen concentration in the nanoformulation is related to the gas solubilization capability of perfluoropentane (80 mL O<sub>2</sub> for 100 mL perfluoropentane). Indeed, the MOLNBs nanosuspension was saturated with O<sub>2</sub> until reaching a 35 mg/L concentration in the aqueous media, during the preparation process. In these conditions, our previous study<sup>162</sup> showed a passive sustained and long-lasting oxygen release at different temperatures.

Interestingly, the versatile and peculiar architecture of MOLNBs can allow the incorporation of drugs with different chemical properties. In fact, the nanostructure consists of three domains: the core, the shell, and the interface<sup>179</sup>. Their different lipophilicity was exploited for the incorporation of drugs, enabling high payloads<sup>180–182</sup>. Previously, chemotherapeutic drugs, such as doxorubicin and paclitaxel, were loaded in polymer-shelled NBs showing good stability and prolonged release kinetics<sup>183–185</sup>. Moreover, they were intravenously injected in mice without any acute side effects.

The absence of haemolytic activity of MOLNBs is an important aspect, being a key parameter for assessing the safety of the nanocarrier and biocompatibility, and is strictly required for intravenous administration in early preclinical development<sup>186,187</sup>

In vitro cytotoxicity assay and confocal microscopy images indicate that MOLNBs interact in a non-toxic way with hBMECs and are localized in the cytoplasm compartment of the cells, as a result of internalization, even if the uptake mechanisms are still not completely elucidated. These results highlight the potentiality of MOLNBs to enter in the CNS cells. Furthermore,

these data pave the way for future investigation concerning the ability of MOLNBs to cross brain barriers in an in vitro model.

The magnetic properties of MOLNBs were already investigated in previous research showing their superparamagnetic behavior and the possibility of monitoring their concentration in tissue with MRI<sup>162</sup>. In the same study, we were able to prove that also US may be effective in detecting MOLNBs, due to their vaporizable perfluoropentane core and the density contrast of the SPIONs on their surface. It is worthy of note that perfluoropentane can undergo to Acoustic Droplet Vaporization (ADV) phenomenon when irradiated by US<sup>188</sup>. The ADV favors the liquid to the gas phase shift of perfluoropentane, increasing the US backscattering. The US imaging contrast ability of SPIONs decorated polymer nanobubbles was previously demonstrated by Luo et al.<sup>189</sup>.

Therefore, we manufactured a simple device able to visualize the motion of the MOLNBs in a static magnetic field with field lines in the direction of injection by sonication. This preliminary magnetic investigation shows that MOLNBs can be magnetically guided using external permanent magnets.

The above results support our initial speculation since MOLNBs might be safely administrated either systemically or locally via intravertebral injection in the CSF, monitoring their concentration by MRI or sonography. Several studies evaluated the distribution of intrathecally injected nanoparticles within the CNS, assessing the good ability of administration route via CSF rather than systemic delivery<sup>190,191</sup>. Interestingly, future investigation will involve the study of MOLNBs stability in real matrix fluids, such as serum or CSF.

Furthermore, MOLNBs may be magnetically driven towards target membranes, for instance, the one separating CSF and the interstitial fluid of the brain located in the choroid plexus in the brain ventricles to deliver oxygen and chemotherapy drugs to brain tumors.

Tailoring the driving magnetic field based on the position and dimension of the brain tumor and the brain membranes to be crossed is a goal particularly challenging. Further investigations are required to validate such application by computational models based on MRI or CT tumor images (in silico models) and finally on in vivo animal models.

#### 4.6. Conclusions

Our study provides a complete characterization of the physicochemical properties of MOLNBs and demonstrates their biocompatibility and safety in the case of systemic administration. In addition, this nanoformulation might be considered a good starting point for developing a system able to cross the brain membranes, the main obstacle to enter CNS. Furthermore, our preliminary results highlighted the capability of MOLNBs to be magnetically driven. To summarize, this work opens new opportunities to consider MOLNBs in targeting brain tumors since they can deliver oxygen (potentiating radiotherapy) and chemotherapy drugs, being driven by ad hoc tailored magnetic fields under MRI and/or US monitoring.

## Chapter 5:



*Article*

# Step-by-Step Design of New Theranostic Nanoformulations: Multifunctional Nanovectors for Radio-Chemo-Hyperthermic Therapy under Physical Targeting

Shoeb Anwar Ansari <sup>1,†</sup>, Eleonora Ficiara <sup>1,\*,†</sup>, Federico D'Agata <sup>1</sup>, Roberta Cavalli <sup>2</sup>, Lucia Nasi <sup>3</sup>,  
Francesca Casoli <sup>3</sup>, Franca Albertini <sup>3</sup> and Caterina Guiot <sup>1</sup>

## 5.1. Introduction

In spite of the dramatic progress in tumor control, some specific organs and/or tumor stages require multi-treatment approaches to counteract cancer progression. This is the case, for instance, in unresectable head and neck tumors, which are normally treated with chemoradiotherapy and also benefit from external hyperthermic treatments<sup>192,193</sup>. Moreover, pancreatic cancer normally requires multimodal treatments since the response to traditional therapies is largely unsuccessful<sup>194</sup>.

Most importantly, tumors of the central nervous system (CNS) are still poorly treated because, very often, it is almost impossible to reach their site without seriously damaging the nearby structures.

Besides surgery, less invasive approaches are also critical, mainly due to the presence of biological membranes (such as the blood-brain barrier, BBB) preventing the passage of drugs<sup>195–197</sup>.

As far as conventional radiotherapy is concerned, most of the tumor tissues are weakly radiosensitive, also because of their hypoxic state.

The main therapeutic approaches are scarcely effective when applied individually; therefore, it may be useful to investigate whether their combination may induce synergistic effects.

Consequently, we developed a multimodal approach to target all the above critical issues with a unique theranostic system.

### 5.1.1. Loading and Delivery of Oxygen to Hypoxic Tissues

The feasibility of oxygen delivery to hypoxic tissues and organs has been investigated in various studies<sup>198,199</sup>. Hemoglobin-loaded particles (Hb particles), encapsulated within a biodegradable polymer, have been prepared for use as oxygen carriers<sup>200</sup> and showed an oxygenation capacity similar to that of native hemoglobin, as well as a prolonged circulation time after administration, in mice. Albumin microbubbles for oxygen and nitrogen delivery have been formulated<sup>201</sup> for use as contrast agents, together with lipid-coated perfluorocarbon (PFC) microbubbles, which were tested in a model of anaemic rats<sup>202,203</sup>, allowing survival at very low haematocrit levels.

Due to their excellent solubility for oxygen, perfluorocarbons were used also in the so-called 'liquid-assisted ventilation' technique, where PFC recruitment of surfactant deficient (e.g., neonatal hyaline membrane disease) or impaired alveoli was shown to be very effective<sup>204</sup>.

Reducing the dimension of the bubble allows larger internal partial pressures due to Laplace's law, and oxygen, being very soluble in perfluorocarbons both storing and delivering oxygen in hypoxic tissues, is enhanced by nanodimensions: oxygen-loaded nanobubbles have therefore been developed. Because of their theranostic property, oxygen-loaded nanobubbles are also very appealing nanocarriers for potential application in cancer therapy.

#### 5.1.2. Loading and Delivery of Anticancer Drugs

Interestingly, the choice of vectors in the nanometric scale is challenged by the presence of very selective biological barriers<sup>205</sup> or when the specific position is difficult to target. Due to their small size, nanoparticles have distinct properties compared with the bulk form of the same materials, and the interactions of nanoscale objects with living systems have yet to be thoroughly investigated. For instance, in biological fluids, proteins interact with nanoparticles, inducing *in vivo* responses<sup>206</sup>, which may limit the efficiency of the systemic delivery of drugs and active compounds expected to reach a specific organ. As a matter of fact, nanocarriers can improve the drug's transport efficiency and targeting of the cancer cells, and, acting at a specific site, they can reduce the side effects on the body. Significant improvements in the effectiveness of treatment by 'nano-carried' or 'bulk' drugs are, however, debatable. As gene therapy is a new frontier in cancer care, the use of (non-viral) nanovectors for genetic material delivery is very promising<sup>207</sup>.

To improve the local effectiveness, many targeting systems have been devised, mainly based on the actual bias concerning the coupling of targeting substances on the surface of the nanostructure.

In addition to chemical ones, physical targeting methods have also been investigated in the past<sup>208</sup>. Ultrasounds (US), in an appropriate frequency and intensity range, were shown to be able to transiently open the BBB, allowing the safe and effective delivery of drugs to the CNS. Based on this concept, a technique called Focused Ultrasound (FUS) has been developed, and many applications, mainly performed under MRI control, have already been demonstrated under FDA permission<sup>209</sup>.

Details on the US-mediated oxygen release can be found in the literature<sup>210</sup>. Such physical enhancement is of great importance whenever tissues can be effectively sonicated, e.g., the depth of the lesion to be treated is not too large and there are no interposed tissues with high

impedance. For this reason, sonication is scarcely of interest for application in the CNS since the skull almost completely shields the mechanical waves.

### 5.1.3. Magnetic Physical Targeting and Hyperthermia

Another physical targeting method near maturity is based on the use of magnetic fields able to drive nanoparticles with proper magnetic properties to their site of action. Many papers have focused on the feasibility of external driving implants<sup>211</sup>, on the biodistribution of the magnetic vectors, on their ability to overcome the BBB<sup>212</sup>, and on their toxicological properties<sup>213,214</sup>.

SPION-decorated dextran-sulphate-shelled OLNBs, i.e., magnetic oxygen-loaded nanobubbles (MOLNBs), manufactured by adding SPIONs to the surfaces of polymeric nanobubbles, have been designed as promising theranostic carriers for delivering oxygen and chemotherapy to critical tumors, such as CNS ones. Physicochemical and cytotoxicological properties and in vitro internalization by human brain microvascular endothelial cells, as well as the motion of MOLNBs in a static magnetic field, have therefore been investigated. Previous studies showed the potentiality of MOLNBs to be magnetically drivable using external permanent magnets. A challenging goal could be tailoring the driving magnetic field based on the position and dimension of the tumor and the membranes to be crossed.

Hyperthermia, a treatment designed to raise the temperature of cancerous regions of the body to 40–43°C, can cause cancer cell death by enhancing the cytotoxic effects of radiotherapy and chemotherapy. Although it is rarely used as a single treatment method in contemporary oncological management, several randomized studies show that, in conjunction with radiotherapy, it has the potential to improve the results of concomitant cancer treatments without significantly increasing their toxicity<sup>160</sup>.

Magnetic hyperthermia, consisting of the endogenous production of heat from nanomagnetic structures precisely inserted into the target tumor by applying an external time-varying magnetic field, is one of the most efficient and safe therapeutic approaches<sup>215</sup>.

## 5.2. Materials and Methods

### 5.2.1. Materials

Ethanol, perfluoropentane, Fe<sup>2+</sup>, and Fe<sup>3+</sup> were from Sigma-Aldrich. Epikuron® 200 (soy phosphatidylcholine 95%) was a kind gift from Cargill. Palmitic acid and dextran sulfate sodium salt (Mw = 100,000) were from Fluka (Buchs, CH, Switzerland).



## 5.2.2. Methods

### 5.2.2.1. Preparation of Chitosan Oxygen-Carrying Nanobubbles

At 25°C, a saturated solution of O<sub>2</sub> in 0.9 mg/mL NaCl was prepared and used for nanobubble preparation. Then, 300 µL of an ethanolic solution containing Epikuron 200 (1%, w/v) and palmitic acid (0.3%, w/v) was injected into a sealed vial of 10 mL of the O<sub>2</sub> solution under stirring. The system was homogenized for 2 min at 20,000 rpm using an Ultra-Turrax TA 18 homogenizer (IKA), which allowed the tool head to work at high peripheral speeds to generate very high shear rates for fast and efficient sample processing. Then, under continuous oxygen purging, 400 µL of 2.5% chitosan solution in acetate buffer with pH 5 was added as a polymeric shell for the nanobubbles. Then, 1 N NaOH solution was added under gentle stirring to obtain the desired pH.

### 5.2.2.2. Dextran and Dextran sulfate oxygen loaded nanodroplets

For oxygen-loaded nanodroplet liquid formulations, 1.5 mL DFP (Fluka, Buchs, Switzerland) along with 0.5 mL polyvinylpyrrolidone (Fluka, Buchs, Switzerland) and 1.8 mL soy lecithin (Degussa, Hamburg, Germany) solved in 1% w/v ethanol (Carlo Erba, Milan, Italy) and 0.3% w/v palmitic acid solution (Fluka, Buchs, Switzerland) were homogenized in 30 mL water (preparation A) or phosphate-buffered saline (PBS) (preparations C-D) for 2 min at 24,000 rpm by using an Ultra-Turrax SG215 homogenizer (IKA, Staufen, Germany). Ultrapure water was obtained using a 1–800 Millipore system (Molsheim, France). Thereafter, the solution was saturated with O<sub>2</sub> for 2 min. Finally, 1.5 mL dextran sulfate solution was added dropwise and homogenized for 2 min at 13,000 rpm. PFP was used as a core fluorocarbon in the OLN water formulation. Without adding oxygen, oxygen-free nanodroplet (OFND) and nanobubble (OFNB) water formulations were produced according to OLND and OLN methods. The OLND preparation process was used for the oxygen-saturated solution (OSS) water formulation, skipping the inclusion of dextran and DFP. Core fluorocarbon without adding oxygen, oxygen-free nanodroplet (OFND), and nanobubble (OFNB) water formulations were produced according to OLND and OLN methods.

### 5.2.2.3. Synthesis of SPIONs

There are numerous methods for synthesizing SPIONs. The co-precipitation method is the simplest chemical method for producing iron oxide nanoparticles. Using this method, we dissolved 0.99 gm and 2.7 gm of Fe<sup>2+</sup> and Fe<sup>3+</sup> in 50 mL of distilled water, respectively.

Magnetite is prone to oxidation; therefore, inert gas (nitrogen) purging was required under continuous stirring at 85 °C for 45 min to prevent magnetite transformation to maghemite.

The reaction mixture was then treated with 10 mL of 30% ammonia solution until the pH reached 12, and we continued stirring overnight, resulting in black-colored precipitation. After the system reached a precipitation state, the precipitation was allowed to cool and settle at the bottom of the flask at room temperature. A permanent magnet was used to separate the black precipitates from the supernatant. The precipitate was rinsed with distilled water and allowed to dry in the open air for 24 h.

#### 5.2.2.4. Preparation of MOLNB Formulations

The mixture of Epikuron 200 (2.5% w/v) and palmitic acid (0.5% w/v) was prepared in ethanol. Then, 400 µL of perfluoropentane was added to 300 µL of the mixture of Epikuron 200 and palmitic acid in an ice bath. Then, 4.8 mL distilled water was added dropwise. After this, the complete system was homogenized for 2 min at 20,000 rpm by using a high shear homogenizer (ultra-turrax TA 18) until the formation of a nanoemulsion. Thereafter, the nanoemulsion was incubated at 37 °C and saturated with oxygen for 10 min. Then, 400 µL of an aqueous solution of dextran sulfate sodium salt (2% w/v) was added dropwise as a polymeric shell under oxygen purging. Finally, 5.9 mg (1 mg/mL) and 2.95 mg (0.5 mg/mL) of SPION suspensions were added to NB under stirring, to obtain MOLNBs of two different concentrations [25]. MOLNBs containing 1 mg/mL and 0.5 mg/mL SPIONs correspond to around 25.76 % w/w and 14.78 % w/w SPION concentrations and were used directly without separating uncoated SPIONs.

#### 5.2.2.5. In Vitro Oxygen Release Study

In vitro study of oxygen release from MOLNBs was performed at different temperatures (i.e., 25 °C, 37 °C, 41 °C). Dialysis bag technique was used for oxygen release: the bag was filled with 3 mL of donor phase, such as MOLNBs. Then, the bag was placed in 50 mL of saline solution (NaCl 0.9% w/v); the oxygen concentration of the saline solution was previously reduced up to 2.5 mg/L by purging inert gas (nitrogen, argon). The oxygen release by diffusion was monitored for 24 h using an oximeter (Hach.) HACH HQ 40D is a digital oximeter connected with a LDO 101 digital, luminescent/optical dissolved oxygen (LDO) probe. We set a 30 min time interval for determining oxygen release, and every 30 min, the instrument recorded the oxygen concentration in the sample<sup>216</sup>.

#### 5.2.2.6. Physicochemical Characterization of OLNBs, OLNDs, and MOLNBs

The mean diameter, polydispersity index (PDI), and zeta potential were determined by dynamic light scattering spectroscopy (DLS) at room temperature. The samples were diluted with distilled water in an electrophoretic cell. Each determined value was the average of five reciprocals for diameter measurement and 10 reciprocals for  $\zeta$  potential determination; a 15 V/m electric field was used for  $\zeta$  potential determination. The viscosity and osmolarity were determined at room temperature by using a capillary viscosimeter and osmometer, respectively.

#### 5.2.2.7. Morphological Evaluation

The morphological examination of OLNBs, OLNDs, and MOLNBs was carried out by transmission electron microscopy (TEM) in conventional mode, by using a JEOL 2200FS microscope working at 200 kV. MOLNBs were also investigated by high-angle annular dark-field scanning transmission electron microscopy (HAADF-STEM). To minimize the radiation damage from the electron beam, the HRTEM images were acquired using a very low beam current and low exposure time.

#### 5.2.2.8. Magnetic Measurements and Hyperthermic Properties

The magnetic properties of OLNBs, SPIONs, and MOLNBs were measured at room temperature by an alternating gradient force magnetometer. The magnetization cycles were performed by applying a maximum magnetic field  $\mu_0 H = 1.8$  T.

Calorimetric measurements using an AC commercial applicator were used to evaluate the hyperthermia properties (nanoScale Biomagnetics DM100, Zaragoza, Spain). The specific needs involved in the process of applying a magnetic field and in measuring and analyzing the results were thoroughly examined and approached one at a time, leading to an integrated and final solution that ensured the highest standards in magnetic hyperthermia research. MOLNBs containing two different low concentrations of SPIONs (0.5 and 1 mg/mL) were tested by means of a DM100 nanoScale Biomagnetics apparatus for the measurement of magnetic hyperthermia. They were exposed for 30 min to an RF alternating magnetic field with amplitude = 300 Oe and frequency = 429 kHz. To avoid coupling with the RF field, the temperature increase was measured with an optical fiber thermometer. Based on a report from the manufacturer, an uncertainty level of  $\pm 10\%$  in the temperature measurements was assumed.

The specific absorption rate (SAR) in W/g of the formulation was calculated by the following equation:

$$SAR = \frac{C\rho}{c} \frac{dT}{dt}$$

where  $c$  is the specific heat capacity of the sample (assumed to be 4.18 J/g °C), the density of the solvent (equal to 1 g/mL),  $C$  the concentration of the magnetic NB in the solvent (1 g/L and 0.5 g/L), and  $dT/dt$  the heating rate of the sample, calculated by fitting its temperature increase  $\Delta T$  with a linear trend at an early time point.

#### 5.2.2.9. Evaluation of Antitumor Effect of Doxorubicin and Curcumin-Loaded OLNDs

TUBO cells, from a cloned rat Her2/neu+ cell line established from lobular carcinoma of a BALB-neuT mouse, were incubated for 48 h in the absence/presence of different concentrations of OLNDs, free chitosan, or DOX (either free or carried by OLNDs).

Curcumin-loaded OLNBs were prepared at different concentrations (1-15  $\mu$ M) and delivered to PC-3 and DU-145 cultured cells. Cell viability was checked by 3-(4,5-dimethylthiazol-2-yl)-2,5-diphenyltetrazolium bromide assay (MTT). All measurements were performed with the same batch, incubation time, and microplate reading techniques.

#### 5.2.2.10. Curcumin Release during HT

The in vitro curcumin release from curcumin-loaded MOLNBs was studied before and after HT using a multi-compartment rotating cell. Curcumin-loaded MOLNBs was placed in the donor chambers. The receiving and the donor chambers were separated by a semi-permeable cellulose membrane (cut-off 14 kDa). The receiving phase for all formulations was 2-Hydroxypropyl-beta-cyclodextrin (5% w/v). Moreover, 1 mL of sample was withdrawn at fixed times during the experiment, which lasted 26 h. The curcumin concentration was evaluated by HPLC (Shimadzu, UV/VIS detector SPD-20AV.)

#### 5.2.2.11. MRI Testing

MRI experiments were performed in a clinical magnetic resonance (MR) Scanner (3.0 T, Vida, Siemens). MOLNBs were suspended in tubes at different concentrations of SPIONs, such as 2.5, 2, 1, 0.5 mg/mL. The tubes were placed into the MR scanner and several MR sequences were run. We acquired multiple spin-echo varying 10 times the echo time (TE) in steps of 15 ms (max 150 ms, the repetition time was 3000 ms, TR, and the total duration of the measurement was around 20 min). We repeated the experiment 3 times, computing means and SD. To measure signal intensity, manually drawn regions of interest were used for each

sample in DICOM viewer software. The data were fitted in Microsoft Excel 2010 with an exponential curve to obtain  $T_2$  estimates.

#### 5.2.2.12. Magnetic Field and US Imaging Monitoring

Suspension of MOLNBs was injected into a plastic cylinder and sonicated. Two permanent cylindrical magnets (diameter = 6 mm, height = 0.75 mm) of neodymium covered with Ni-Cu-Ni (<https://calamite.org>, accessed on 26 July 2021) were located on the cylinder wall and the magnetic fields were calculated by using Python package Magpylib [39]. B-mode US imaging was performed to study the reaction of MOLNBs to the external magnetic field. MOLNBs (at concentration  $1 \times 10^{10}$  NB/mL) were injected in the plastic cylinder containing demineralized water with a syringe, through a glass tube. The experiment was carried out at a temperature of 25 °C. MOLNBs were sonicated using US clinical equipment (MyLab™25Gold Esaote, Genova, Italy), connected to a linear array transducer (LA523, 7.5 MHz central frequency, Esaote, Genova, Italy) operating in B-mode (small parts imaging preset). B-mode cine-loops (30 s) were acquired and recorded for postproduction both in the absence and in the presence of the magnets. Snapshots from cine-loops were extracted at different time frames (5, 15, 30 s) after the initial injection in the different configurations.

### 5.3. Results

#### 5.3.1. Oxygen-Loaded Nanosystems: Loading and Delivery of Oxygen to Hypoxic Tissues

Different oxygen-loaded nanosystems have been studied by our team, differing both for the polymer in the shell and the inner fluorocarbon agent storing oxygen to enhance the structural stability. A detailed description is given in Table 5.1 and an illustration in Figure 5.1.

**Table 5.1.** Different oxygen-loaded nanosystems. OLNb: oxygen-loaded nanobubbles; OLND: oxygen-loaded nanodroplets.

Shell Polymer	Perfluoropentane $C_5F_{12}$ (PFP) Core	Decafluoropentane $C_5H_2F_{10}$ (DFP) Core
Chitosan/Dextran/Dextran sulfate	OLNB	OLND

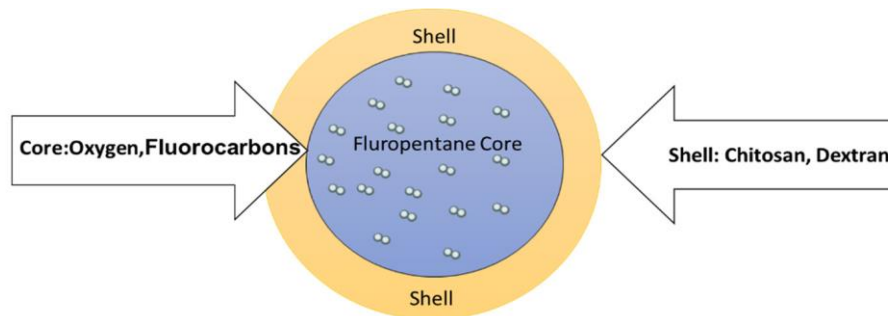


**Figure 5.1:** Structure of the oxygen-loaded nanosystem.

The main difference between PFP and DFP is their boiling point (28 °C for the former, in vapor state at human body temperature, therefore forming bubbles, and 55 °C for the latter, which is liquid at body temperature, forming droplets). This difference in boiling points might also impact the echogenic properties and the possibility of detection by US.

Both PFP and DFP are suitable for human use and are expected to be completely eliminated by expiration. Furthermore, all the natural polysaccharide polymers used in the different formulations are biodegradable and biocompatible.

According to the manufacturing details given in the Appendix, oxygen-loaded nanosystems can be characterized by the natural polysaccharide used for the shell, which defines their surface properties, their Zeta potential, and the oxygen exchange effectiveness. For the cases of chitosan and dextran details can be found in<sup>216,217</sup>.

Due to their dimensions and physical characteristics, the morphology of the above nanostructures can be investigated by transmission electron microscopy (TEM) (Figure 5.2a), fluorescent microscopy provided a FITC-labeled shell has been applied (Figure 5.2b) and, especially for OLNBs, by US (Figure 5.2c).

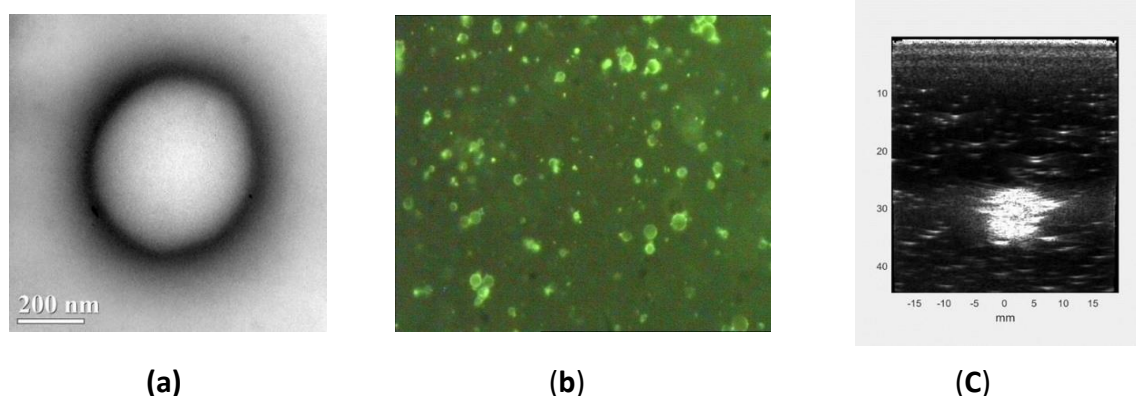


**Figure 5.2.** TEM (a), optical fluorescence (b), and US (c) imaging of OLNBs

Precise quantification of the oxygen contained in the nanostructures is very difficult; however, indirect estimates, e.g., based on salt oxidation, give an average value of 400  $\mu\text{g}/\text{mL}$  for OLNBS<sup>218</sup>. Besides their composition, oxygen release kinetics from the OLNBS by passive diffusion depend also on the characteristics of the considered external medium, its temperature, and its initial oxygen concentration. Moreover, the rate and extent of the oxygen release can be significantly increased by sonication<sup>217,218</sup>.

In Figure 5.3, the rate of oxygen exchange between the donor compartment containing the OLNBS and the receiving compartment composed of different liquids, i.e., saline and Perfadex®, used as perfusion medium in lung transplants, is shown (Figure 5.3a), together with the experimental device designed for the measurement (Figure 5.3b).

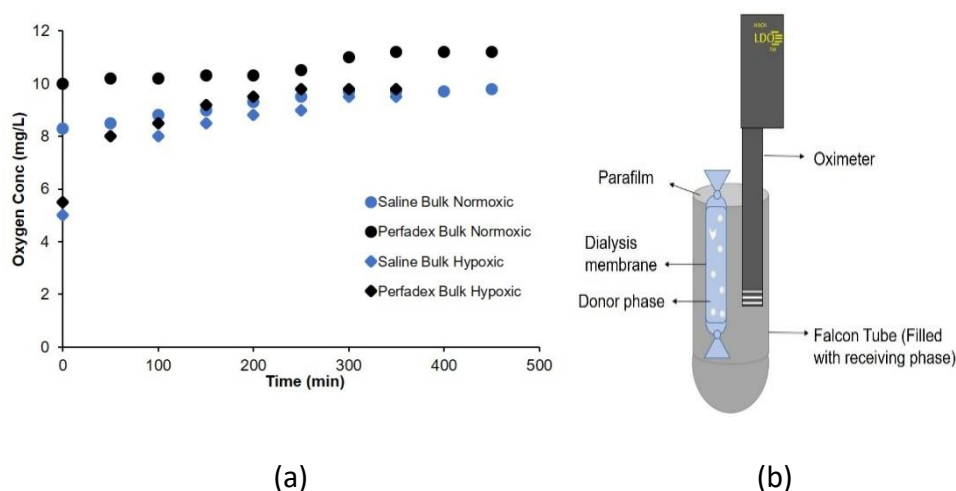


**Figure 5.3.** Examples of passive oxygen release in fluids: (a) oxygen concentration in different liquids, saline, and Perfadex, in normoxic and hypoxic bulk at 4° C; (b) Sketch of the device for measuring oxygen diffusion from the donor compartment to the bathing medium. Data are measured with an accuracy of  $\pm 1.5\%$  of the nominal value.

According to the results presented in Figure 5.3, oxygen exchange occurs by passive diffusion and is therefore accelerated in hypoxic media. The coefficient of diffusion is markedly dependent on the characteristics of the external media. Preliminary experiments of oxygen diffusion were performed on animal models using dextran shelled OLNDS.

**5.3.2. Drug-Loaded Oxygen-Loaded Nanosystems: Loading and Delivery of Anticancer Drugs**  
Oxygen-loaded nanodroplets (OLNDs) can be loaded with drugs and/or natural substances to counteract the development of tumors or prevent their local recurrence. Doxorubicin (DOX)

and curcumin (Curc) have been previously investigated in this context [31,32]. Doxorubicin is easily encapsulated in the chitosan-shelled nanodroplet structure and in DOX-loaded OLNDs, showing, even at low doses, marked effectiveness when administrated both in vitro and in vivo to TUBO cells, in a cloned rat Her2/neu+ cell line established from lobular carcinoma of a BALB-neuT mouse (Figure 5.4). Internalization of DOX-loaded OLNDs occurred also in vivo after administration in tumor-bearing mice, and the tumor growth limitation is related to the variable uptake efficiency of the nanovector<sup>219</sup>.

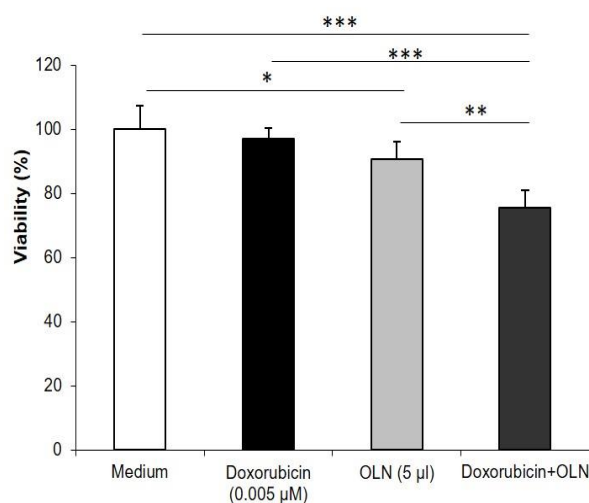


**Figure 5.4.** DOX in OLND promotes synergistic antitumor effects. Cell viability was evaluated by MTT assay. Data are expressed as percentage vs control. TUBO cells were left untreated or incubated for 48 h with DOX (0.005 μM), OLNDs (2.5% v/v), or DOX-loaded OLNDs (0.005 μM/2.5% v/v). Results are shown as means ± SD from three independent experiments. Significance of the differences: \* p < 0.05; \*\* p < 0.005; \*\*\* p < 0.001.

The in vivo results confirmed the potential of OLNDs as oxygen and drug delivery systems<sup>219</sup> after administration in mice.

Another formulation based on the association of dextran sulfate shelled OLNBS and curcuminoids (Curc) was shown to be effective in vitro against prostate cancer cells. The inhibition of the viability of PC-3 and DU-154 tumor cells is greatly improved when Curc is delivered by OLNBS at all doses (see Figure 5.5). Moreover, other important inhibitory effects of Curc-loaded OLNBS on cell motility and adhesivity were detected<sup>220</sup>.



Step-by-Step Design of New Theranostic Nanoformulations: Multifunctional Nanovectors for Radio-Chemo-Hyperthermic Therapy under Physical Targeting

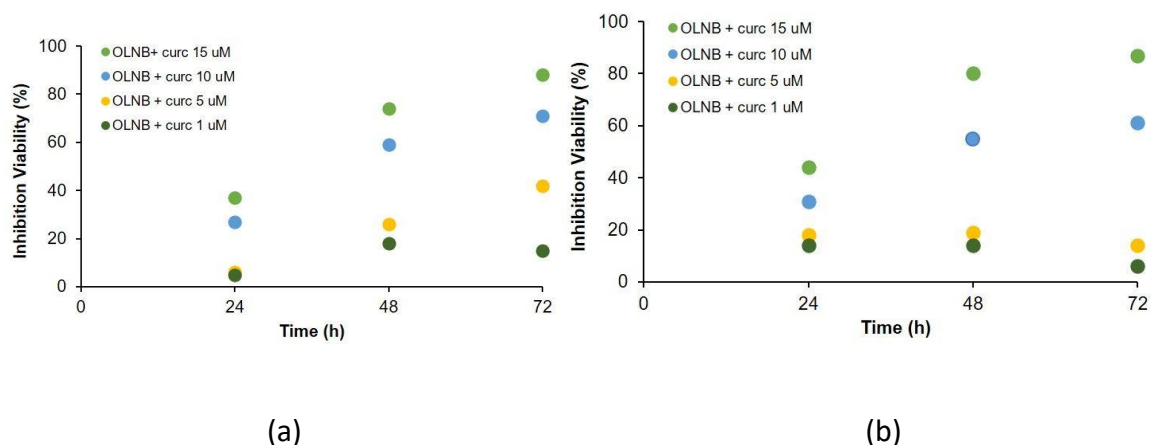


**Figure 5.5.** Percentage of inhibition of viability: (a) PC-3 tumor cells; (b) DU-145 tumor cells.

### 5.3.3. SPION-decorated OLNBs: Manufacturing and Physicochemical characterization of MOLNBs

The physicochemical characterization of OLNBs and MOLNBs is reported in figure 5.6. The highly negative Zeta potential (about -29 mV) of OLNBs is due to the presence of dextran sulfate on the nanobubble surface. The average Zeta potential of MOLNBs, decreased to -18.33 mV, because of the electrostatic interaction between the positively charged SPIONs decorating the negatively charged OLNBs. Other characteristics parameters of the MOLNBs nanosuspension such as viscosity, and osmolarity were 0.96 cP and 354 mOsm, respectively.

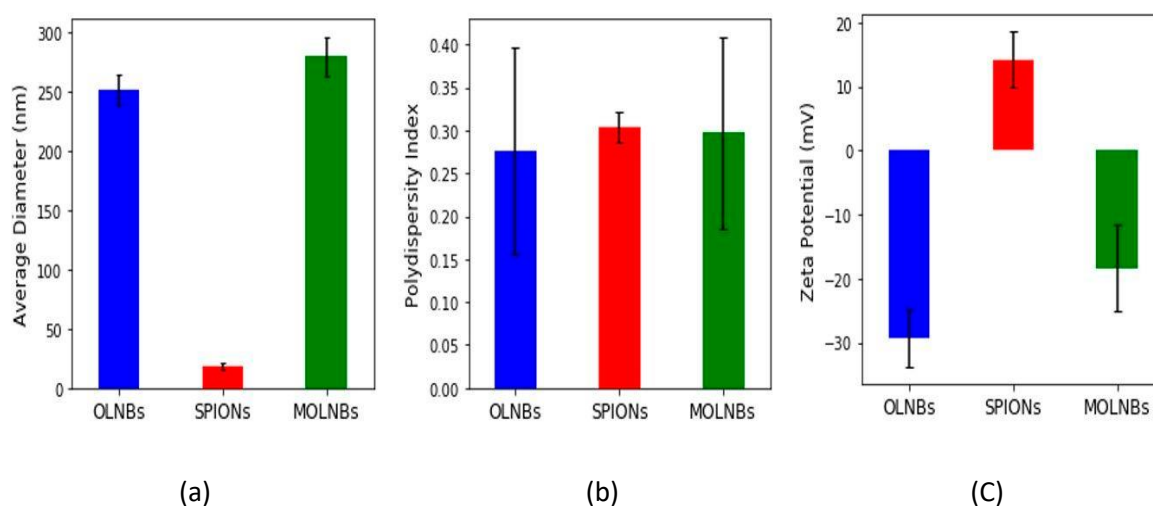


**Figure 5.6:** Physicochemical characteristics of nanocarrier formulations: (a) average diameter (nm); (b) polydispersity index; (c)  $\zeta$  potential (mV) for OLNBs (blue), SPIONs (red) and MOLNBs (green).

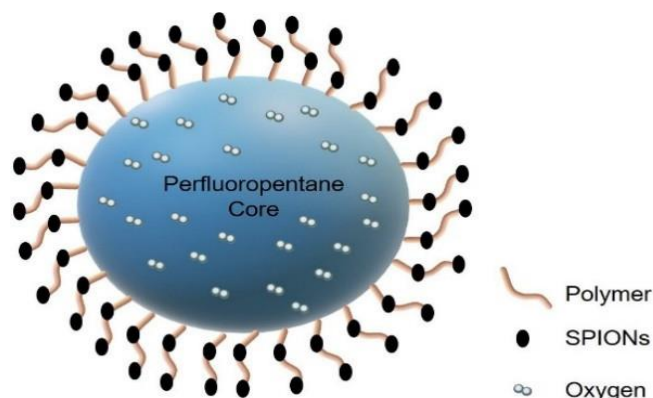


**Figure 5.7:** Illustration of MOLNBs (negatively charged dextran shell NBs decorated with positively charged SPIONs by electrostatic interaction).

The MOLNBs structure can be visualized in high-angle annular dark-field imaging (HAADF-STEM) mode at different scales (Figure 5.8). The atomic number contrast images clearly show the core/shell structure of the NBs and the SPIONs (bright spots) embedded in the polymeric shell of MOLNBs

Oxygen release at different temperatures (Figure 5.9) was evaluated, showing a significant increase at hyperthermic temperatures. Furthermore, MOLNBs showed a slightly change in Zeta potential from  $-18.33 \pm 2.82$  to  $-16.21 \pm 1.71$  over 3 months indicating chemico-physical stability of the nanostructure.

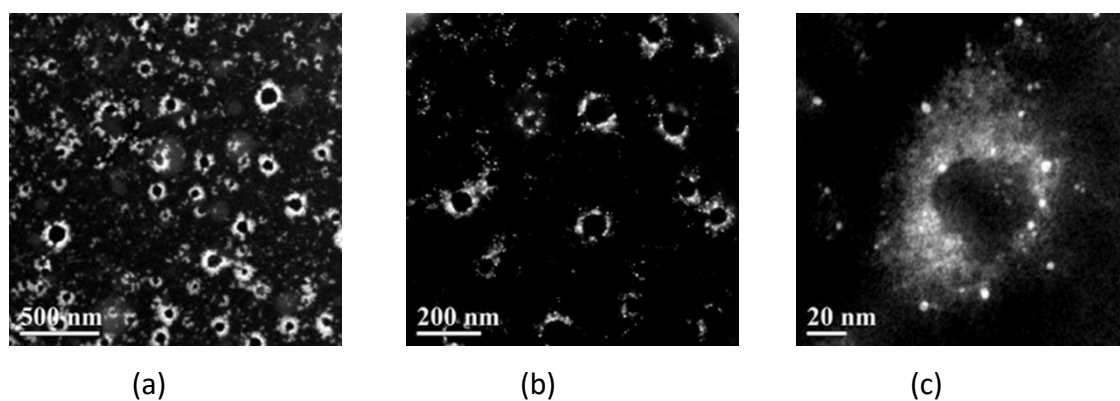


**Figure 5.8:** HAADF-STEM images of the MOLNBs decorated with SPIONs taken at different magnifications ((a) = 500 nm, (b) = 200 nm, (c) = 20 nm).

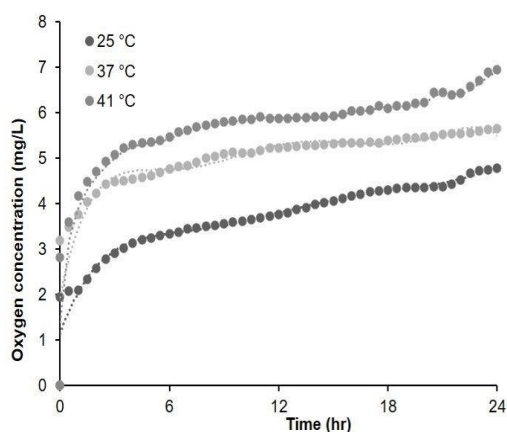


**Figure 5.9:** Oxygen release study performed by passive diffusion in saline solution at different temperatures over 24 h. Data of oxygen concentration were measured with an accuracy of  $\pm 1.5\%$  of the nominal value.

### 5.3.4. Magnetic Characterization of MOLNBs

#### In Vitro MRI Test

The properties of MOLNBs as contrast agents were investigated in vitro by MRI scanning using clinical equipment (3.0 T, Vida, Siemens), evaluating their relaxation time at different concentrations of the decorating SPIONs by transverse relaxation ( $T_2$ ) mapping.  $T_2$  values were obtained from exponential fitting of the signal and TE and are shown in Table 5.2, which indicates that an increasing concentration of SPIONs led to a  $T_2$  reduction.

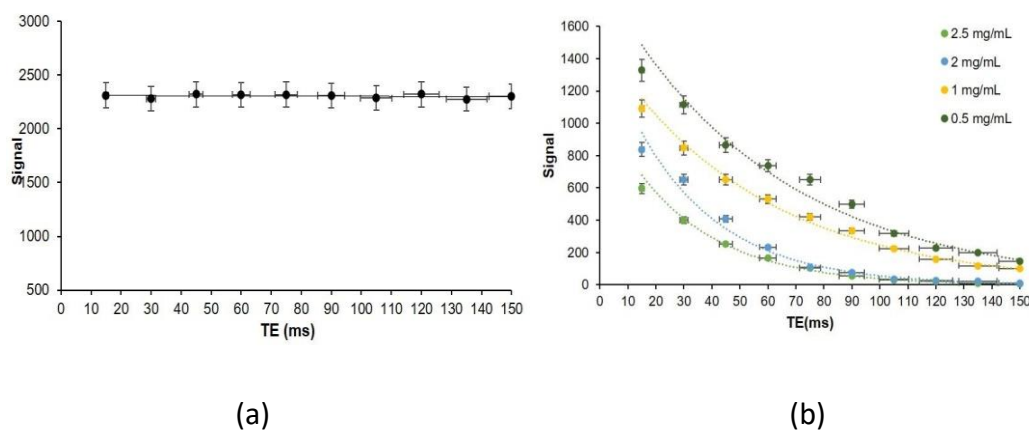


**Figure 5.10:** (a) Signal intensities of blank OLNBs at different TE value and (b) signal intensity of 0.5, 1, 2.0 and 2.5 mg/mL SPIONs concentration on MOLNBs at different TE values as a function of echo delay time.  $T_2$  is inversely proportional to the concentration of SPIONs loaded on MOLNBs, increased concentration shows a sharp reduction in the signal intensity. The error bars show SD.

**Table 5.2:** T2 signal values obtained from curve fitting.

Concentration(mg/mL)	Blank	0.5	1	2	2.5
T <sub>2</sub> (ms)	2000	58.82	55.55	30.30	29.41

### 5.3.5. Magnetic and Hyperthermic Properties of MOLNBs

The magnetic properties of OLNBs, SPIONs, and MOLNBs were measured at room temperature by an alternating gradient force magnetometer (AGFM) by applying a maximum magnetic field  $\mu_0H = 1.8$  T.

The sample of OLNBs showed a weak diamagnetic signal, obviously negligible with respect to that of SPIONs and MOLNBs, whose magnetic cycle is, respectively, described in Figure 5.11 (a, b).

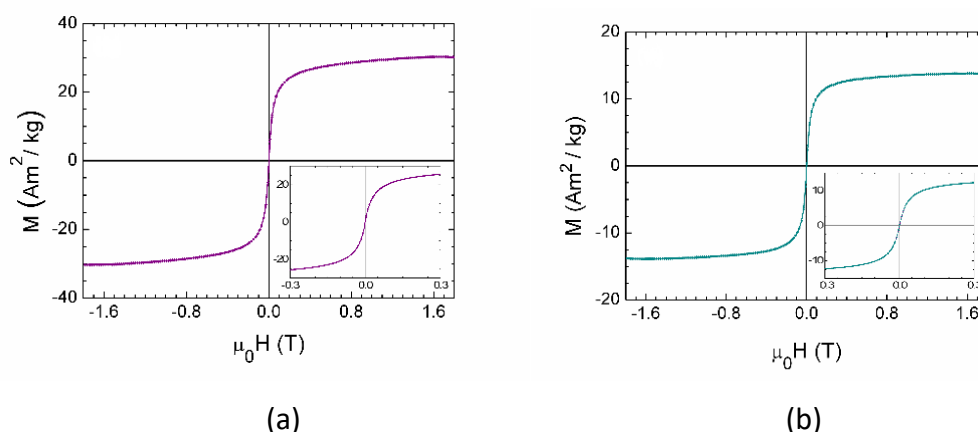


**Figure 5.11.** (a) Magnetization cycle of SPIONs; (b) Magnetization cycle of MOLNBs. In the insets, a zoom of the measurements is reported, highlighting the superparamagnetic behavior of the samples (i.e., absence of magnetic hysteresis and remanence).

The magnetic properties of OLNBs, SPIONs, and MOLNBs were measured at room temperature by an Alternating Gradient Force Magnetometer (AGFM) by applying a maximum magnetic field  $\mu_0H=1.8$  T.

Furthermore, the MOLNB sample showed superparamagnetic behaviour, with a specific magnetization value of  $14 \text{ Am}^2/\text{kg}$  at the maximum applied field  $\mu_0H = 1.8$  T, which is compatible with the known mass concentration of SPIONs (i.e., around 40%) in MOLNBs when taking into account the experimental error of the magnetic measurements. In conclusion,

these results confirm that MOLNBs show superparamagnetic behaviour with the magnetic moment expected for a specific quantity of incorporated SPIONs.

According to these magnetic properties, MOLNBs are effective candidates for hyperthermic agents<sup>221</sup>.

The hyperthermic experiment was carried out by exposing a colloidal aqueous suspension of curcumin-containing MOLNBs to an RF magnetic field for 30 min. In Figure 5.12, the time dependence of the temperature of the samples under irradiation is reported for MOLNBs with two different (low) concentrations of SPIONs (0.5 and 1 mg/mL). Moreover, NBs without SPIONs were exposed following the same procedure in order to evaluate the effects of the thermal dispersion of the equipment (which was subjected to the MOLNB temperatures). After 30 min of exposure, the temperature increase in the curcumin-loaded MOLNBs containing 0.5 mg/mL and 1 mg/mL SPIONs ranged between 2 and 4.8 °C and the corresponding SAR value ranged between  $(9 \pm 1)$  and  $(19 \pm 1)$  W/g, respectively.

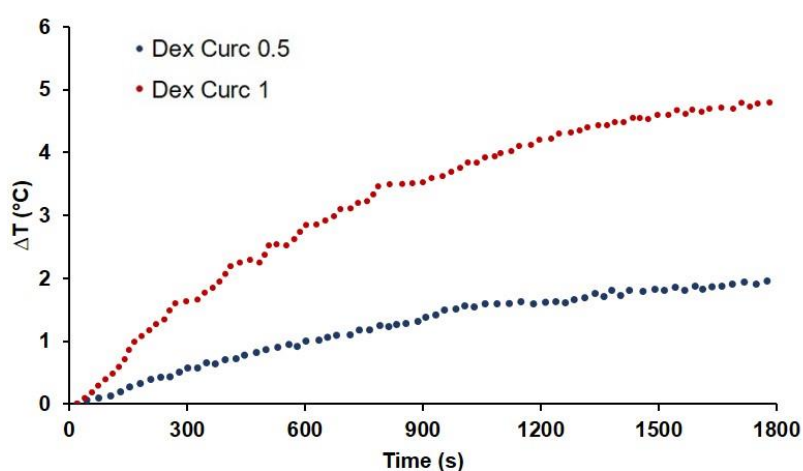


**Figure 5.12:** Magnetic hyperthermia measurements under an alternating ( $f = 429$  kHz) magnetic field of 300 Oe for 30 min: temperature increase as a function of time of the curcumin-loaded dextran MOLNBs at different concentrations of SPIONs (1 mg/mL and 0.5 mg/mL).

The increase in the temperature of MOLNBs is obviously tunable by properly tailoring the nanobubbles and SPION concentration, the RF power, and its timing in order to reach the hyperthermic temperature required by the clinical application.

The curcumin concentration in the solution, after filtering the curcumin-loaded MOLNBs, was evaluated by HPLC and no significant difference was detected before and after HT.

#### 5.3.6. Drivability by the Application of Weak Static Magnetic Fields of MOLNBs

We proposed a setup aimed to simulate the motion of MOLNBs inside fluids in the presence of magnetic fields in different configurations (which can be positioned, for instance, on the skull for CNS tumors), monitoring by US.

After injecting MOLNBs in the setup under US and monitoring the effect of the magnetic field, a significant deviation in MOLNBs' motion toward the magnets was observed (Figure 5.13b) with respect to the homogeneous flow of MOLNBs in the vertical direction in the absence of a magnetic field (Figure 5.13a).

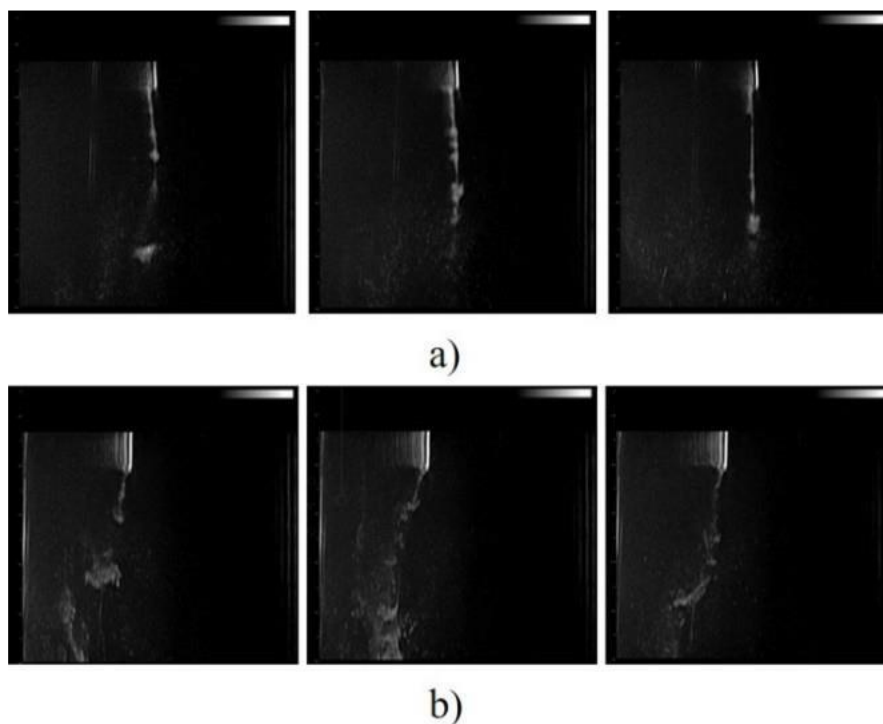


**Figure 5.13.** US imaging snapshot of MOLNBs in the absence (a) and the presence (b) of the magnetic field generated by two magnets (distance 4 cm from each other). Images were recorded at different time frames (5, 15, 30 s) from the injection.

#### 5.4. Discussion

Our team developed a multifunctional theranostic nanovector able to act as an oxygen reservoir for delivering to the hypoxic site of interest (e.g., the tumor) the amount of oxygen required to optimize the effect of radiotherapy, in controlled and prolonged kinetics. Due to

the presence of gases or vaporizable compounds within the inner core (oxygen and fluorocarbons), these nanovectors are called oxygen-loaded nanobubbles (OLNBs) or oxygen-loaded nanodroplets (OLNDs) depending on the vapor or liquid status of the core. While their shells, made of phospholipids, polymers, and surfactants, stabilized the structures, because of their gas cores, they were echogenic and could be used as contrast agents in ultrasonic and photoacoustic imaging. These bubbles, which have novel properties and flexible structures, can be engineered in a variety of sizes as vehicles for gas and drug delivery applications<sup>222</sup>.

The main characteristics of oxygen-loaded nanostructures manufactured with different natural biocompatible and biodegradable polymers containing different perfluorocarbons are revised looking at their possible application as radiosensitizers, based on previous *in vivo* experiments of oxygen diffusion monitored by transcutaneous oximetry (tcpO<sub>2</sub>) and by photoacoustic imaging on mouse legs, which demonstrated a sustained oxygenation effect of OLNDs for up to 1 h<sup>218</sup>.

Their ability to carry and deliver anticancer agents is discussed as well. The cell viability studies confirmed that these multifunctional nanovectors can act as drug delivery systems, improving the effectiveness of the encapsulated drugs, e.g., DOX in OLNBs, which promoted a synergistic antitumor effect, and curcumin-loaded OLNBs, which improved the inhibition of tumor cell viability. Although our evidence is based on two cases, the nanosystems are very flexible and could be easily designed for administering a large variety of different drugs.

Adding to the above nanostructures specific magnetic properties greatly enhances their potentiality either for diagnosis (MRI imaging, in addition to US), therapy (hyperthermia), or the possibility of physical targeting of tissues by exploiting the magnetic driving. Other indirect advantages are also expected, e.g., the temperature in the hyperthermic range induces a marked change in oxygen release over time, with increases in the external aqueous solution oxygen concentration of up to 0.5–1 mg/L. This oxygenation effect might further enhance the therapeutic outcome when hyperthermia is combined with radiation therapy. By gradient force magnetometry, we confirmed the superparamagnetic behaviour of our nanosystems, with the magnetic and hyperthermic properties being correlated with the small size of the MOLNBs and the average number of decorating SPIONs.

In particular, we detected a specific magnetization of 30 Am<sup>2</sup>/kg for SPIONs, and following the decoration of the OLNBs (without any intrinsic magnetic property) with SPIONs at 40% in

mass concentration, the final value of  $14 \text{ Am}^2/\text{kg}$  for MOLNBs is acceptable within the experimental errors. The specific magnetization can be finely tuned by varying the mass concentration of SPIONs according to any specific application, i.e., the position and characteristics of the target and the driving magnetic field.

The SPION concentration also defines the hyperthermic efficiency of MOLNBs, as well as the increase in temperature required by the therapy to induce cellular damage or to promote tumor oxygenation in combination with radiotherapy (or possibly also to enhance the penetration across biological membranes such as the BBB). Curcumin-loaded MOLNBs with different concentrations of SPIONs (0.5 and 1 mg/mL) showed a mild heating response to HT treatment, increasing by  $2^\circ\text{C}$  and  $4.8^\circ\text{C}$ , respectively, after 30 min.

Moreover, the curcumin concentration before and after HT was not significantly different, indicating that no disruption or shrinking occurred during their heating. This is an important result demonstrating safe and long-lasting drug delivery also under HT treatment. Figure 5.13 showed that by applying an external magnetic field generated by permanent magnets, it is possible to induce a significant deviation in the motion of the MOLNBs towards the magnets. This behaviour might be exploited for targeted drug delivery.

Interestingly, the possibility of US monitoring may be useful for triggering drug release from MOLNBs. In combination with MRI, it may allow MOLNBs to be used for precision medicine applications.

As a matter of fact, although such in vitro investigations are very promising, the above hypotheses need accurate validation on in vivo animal models in order to understand the capability of MOLNBs to reach the critical tumors that they intend to target. For instance, their main weakness for application to CNS tumors is that we have presently no data concerning the in vivo BBB trespassing of MOLNBs. Although our preliminary measurements seem to exclude relevant cell toxicity and hemolytic activity, the possibility of systemic administration and BBB overcoming should be tested, to better understand the final fate of MOLNBs.

In fact, BBB crossing is another very challenging task: although such an ability of nanovectors similar to MOLNBs has been shown in the literature, specific interactions between CNS cells and MOLNBs need to be more deeply understood. Interestingly, the behavior and safety of magnetic nanoparticles and their motion in brain tissue under a magnetic field were



previously investigated, showing no adverse effects associated with their motion<sup>223</sup>. In addition, innovative approaches to characterize the BBB permeability and the interaction with nanoparticles can be found in the literature<sup>224</sup>, highlighting the crucial importance of computational models to tune an optimal magnetic force field.

All the collected results show that MOLNBs is a versatile theranostic tool whose strengths are their multi-imaging capability and their ability to physically trigger the delivery of active molecules in combination with therapy protocols.

Thus, MOLNBs could represent a promising nanoplatform for applications to fulfill non-trivial therapeutic needs, such as those related to head and neck tumors, pancreatic tumors, and CNS pathologies.

Finally, our results seem to encourage the possibility of non-systemic administration approaches, e.g., the feasibility of some magnetic driving of the MOLNBs from the brain ventricles (filled by the cerebrospinal fluid (CSF), in which MOLNBs could be injected from the intravertebral spaces) to the nearby tumors to which the cargoes have to be delivered. The contact of CSF with the CNS makes it an attractive medium for drug delivery, circumventing systemic barriers. Several studies demonstrated the possibility of the intrathecal administration of nanoparticles<sup>225</sup> and the administration of active agents directly into the ventricles<sup>226</sup>.

Such a driving approach would require a 'personalized' model, based on CT or MRI imaging and a grid of permanent magnets producing the required magnetic field. However, some of the difficulties can be overcome by the fact that MOLNBs, being a theranostic system, are monitorable either via MRI or US sonography, allowing a real-time tracing of their path.

In conclusion, although still speculative, the availability of versatile theranostic nanovectors such as MOLNBs could open new scenarios for future integrated therapies.

## Chapter 6: Magnetically drivable metal chelators loaded Nanocarriers: A new therapeutic approach in neurological disorder associated with trace metal imbalance.

Shoeb Anwar Ansari, Eleonora Ficiarà , Federico D'Agata , Roberta Cavalli , Caterina Guiot

**Work in Progress.....**

## 6.1. Introduction

Neurodegenerative disorders (NDs) are a serious hazard to people's health. Neurons are a small unit of the nervous system, but neurons do not ordinarily multiply or replenish themselves, they cannot be replaced by the body when they are injured or die. Neurodegenerative diseases are incurable and devastating illnesses that cause nerve cells to degenerate and/or die over time. This affects a person's ability to move and speak and creates problems with movement and mental functioning. In 2019, around 50 million people worldwide were affected by NDs. The central nervous system is the most complex structure of the body and is characterized by a series of barriers such as the blood-cerebrospinal fluid (CSF) barrier, the blood-brain barrier (BBB), blood-spinal cord barrier, and the blood-retinal barrier<sup>227</sup>. BBB is a highly complex structure that strongly regulates the movement of ions for small to large molecules, therefore, shielding the brain from injuries and diseases. The abnormal level of traces of elements (Al, Cu, Mn, Fe, Zn, Hg, Cr) in CFS are precursors of clinically symptomatic dementia. Nanobubbles (NBs) and Magnetic nanoparticles (MNPs) are sub-micron size structures that are primarily designed to increase the stability and improve the biodistribution of the transported drug to the pathological region. The MNPs and NBs will be fabricated to selectively chelate iron and other metals, which are responsible for the pathogenic condition.

Iron is an essential mineral that is used by all cells of the body and is critical for the maintenance of metabolic capacity. Most of the iron in the body is bound to haemoglobin in red blood cells. The levels of iron in cells must be tightly regulated. When iron levels in cells become too high the iron can promote the production of reactive oxygen species (ROS) leading to oxidative stress damage and can induce a form of programmed cell death called ferroptosis. However, mitochondrial function is impaired when iron levels are too low, which limits energy production and growth. Iron chelators bind iron, which prevents it from accumulating in cells, and are typically used in the context of iron overload disorders. The pool of iron that is available for chelation by a given chelator depends on the affinity of the chelator for iron relative to the affinity of endogenous iron-binding proteins. Therefore, chelators with weak affinity will only be able to bind free iron, while strong chelators can also liberate iron that is bound to iron-binding proteins such as transferrin and ferritin. Iron homeostasis becomes dysregulated during aging, leading to

the accumulation of iron in certain tissues, which may promote pathological processes<sup>228</sup>. Therefore, iron chelation has been proposed as a potential therapeutic strategy for neurodegenerative diseases, cardiovascular disease, and cancer<sup>229</sup>.

**Molecular Basis of Iron Dysregulation:** Iron exists in two forms in living organisms: its reduced form,  $\text{Fe}^{+2}$  (or iron (II)), and the oxidized  $\text{Fe}^{+3}$  (or iron (III)) state. The transfer between these states, from ferrous iron ( $\text{Fe}^{+2}$ ) to the ferric form ( $\text{Fe}^{+3}$ ) in a catalytic reaction with hydrogen peroxide (or molecular oxygen) known as the Fenton reaction, can yield the highly toxic hydroxyl radical (OH) via the Haber Weiss reaction<sup>230</sup>. The Fenton reaction is a normal metabolic process, occurring at times including electron transfer in mitochondria and readily in the cytoplasm where a large proportion of iron is reduced. However, in PD patients the ratio of  $\text{Fe}^{+2}$ :  $\text{Fe}^{+3}$  is 1 : 3 rather than 1: 1, as in control brains<sup>231</sup>, although this figure can vary between sources<sup>232</sup>. The iron redox is, therefore, in favor of  $\text{Fe}^{+3}$ . The presence of additional iron together with a diminished supply of antioxidants leads to an increased generation of hydroxyl radicals through various reactions in the microglia, producing a cascade of destructive events including oxidative stress, lipid peroxidation, and eventually apoptosis. The iron increase in the pathology of PD is not dependent on systemic iron imbalance, with local dysregulation of the redox contributing to the overload in the respective tissues<sup>233</sup>.

Significant differences in the content of iron (III) and total iron were found in post mortem substantia nigra of Parkinson's disease. There was an increase of 176% in the levels of total iron and 255% of iron (III) in the substantia nigra of the parkinsonian patients compared to age-matched controls. In the cortex (Brodmann area 21), hippocampus, putamen, and globus pallidus there was no significant difference in the levels of iron (III) and total iron. Thus, the changes in total iron, iron (III) and the iron (II)/iron (III) ratio in the parkinsonian substantia nigra are likely to be involved in the pathophysiology and treatment of this disorder<sup>234</sup>.

#### 6.1.1. Polymeric nanobubbles for Iron chelation

Iron chelators have attracted a lot of attention for their possible therapeutic value in eliminating excess iron from certain brain regions afflicted by neurodegenerative disorders. In order to be effective, an iron chelator must be able to penetrate both cellular membranes and the blood-brain barrier, target the region of iron accumulation without

depleting transferrin-bound iron in the plasma, and remove chelatable iron from the site of accumulation or transfer it to other biological proteins like circulating transferrin<sup>235</sup>

Nanobubbles (NBs) are small bubble-like structures that form at the interface of hydrophobic and hydrophilic surfaces in liquids. At room temperature, NBs are stable, but when heated to physiological temperatures in the body, they may combine to create microbubbles. The development of NBs is dependent on the nucleation of gas from a supersaturated solution at the hydrophobic surface, which traps ambient gases. Bulk, interfacial, plasmonic, and oscillating nanobubbles are the four types of nanobubbles<sup>181</sup>. Nanobubbles consist of a fluoropentane core, phospholipid interface, and polymeric shell. For Iron chelation, we used different polymers such as Chitosan, Glycol Chitosan, Dextran, Glycol chitosan- EDTA, and Glycol chitosan Deferoxamine to optimise the chelation capacity of different polymers for neurological disorders.

Desferrioxamine (DFO) is the iron chelator with the longest clinical experience in treating iron overload. DFO is a highly specific iron (III) chelator with a log stability constant of 30 for the Fe (III) complex and has very little affinity for ferrous iron. DFO has been shown to produce negative iron balance and a significant reduction in the frequency of iron-induced complications in transfusion-dependent patients. It is typically given in an intramuscular formulation and is not suitable for chronic conditions due to its poor bioavailability, short half-life, extremely limited blood-brain barrier (BBB) penetration, and a high potential for acute toxicity. The synthesis of Glycol Chitosan- Deferoxamine functional, biocompatible polymers for use as bioconjugates in the field of polymer therapeutics has received increasing attention in recent years. Interest in the use of polymers to facilitate the delivery of drugs has stemmed from their ability to solubilize, camouflage, or stabilize compounds in order to improve properties such as bioavailability, biocompatibility, immunogenicity, and circulation times. One of the most effective methods for overcoming the drawbacks of parent drugs is its incorporation into drug delivery vehicles.

In particular, the attention was focused on the quantitative methods for engineered nanoparticles to cross brain barriers and to effectively target the Central Nervous System (CNS)<sup>236</sup>. Various chemical and physical approaches have been proposed to satisfy the requirement for effective therapy and imaging<sup>236-239</sup>. As a matter of fact, magnetic

nanoparticles have already been proposed to bypass the Blood-Brain Barrier (BBB) to treat glioblastomas and neurodegenerative diseases<sup>240-243</sup> as well as in regenerative medicine and drug delivery<sup>244</sup>.

### 6.1.2. Bilirubin loaded GC-DFO nanobubbles

Bilirubin is a yellowish pigment that is made during the normal breakdown of red blood cells. UCB (or indirect bilirubin in clinical words) is known as the most powerful endogenous antioxidant and anti-inflammatory. Nano-molar concentrations of UCB can neutralize 10,000 times higher levels of cellular ROS by reducing ROS, UCB may inhibit the N-methyl-D-aspartate (NMDA) excitotoxicity, preventing neuronal death.

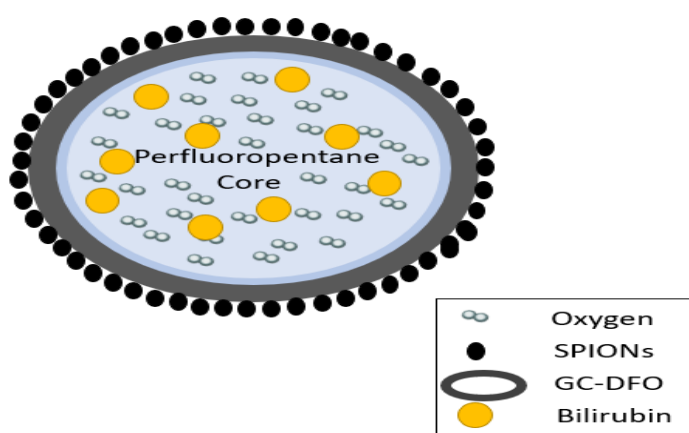


**Figure 6.1:** Bilirubin-loaded magnetic oxygen-loaded nanobubbles.

We propose the bilirubin loaded and SPIONs decorated Glycol chitosan -Deferoxamine and other polymers shelled NBs, i.e., Magnetic nanobubbles (MNBs), Manufactured by adding SPIONs to the surface of polymeric nanobubbles, have been investigated as promising nanocarriers for iron chelation and reduction of oxidative stress for neurological disorder. Physicochemical characterization, cytotoxicological properties, and invitro iron chelation as well as antioxidant study have been investigated.

## 6.2. Materials and Methods

### 6.2.1. Materials

Ethanol, perfluoropentane,  $Fe^{2+}$ , and  $Fe^{3+}$  were from Sigma-Aldrich. Epikuron® 200 (soy phosphatidylcholine 95%) was a kind gift from Cargill. Palmitic acid and dextran sulfate sodium salt (Mw = 100,000) were from Fluka (Buchs, CH, Switzerland).

## 6.2.2. Methods

### 6.2.2.1. Synthesis of Glycol Chitosan-Deferoxamines derivative

100 mg of glycol chitosan was dissolved in 2 mL of distilled water then 97 mg sodium periodate was added to the solution. The solution kept on continues stirring for 24hr at room temperature. After 24hr stirring the solution was dialyzed against the water for 24hr. Desferrioxamine mesylate salt (DFO, 0.300 g) was dissolved in a solution and was continued for overnight stirring then sodium cyanoborohydride 100mg was added under continuous stirring for 16hr. after that, glycine 500mg was added and the solution was dialyzed for 3 days with frequent change of water. The product was characterized by FTIR and NMR spectroscopy<sup>245</sup>.

### 6.2.2.2. Synthesis of Glycol chitosan-EDTA Conjugation

An amount of 500 mg of glycol chitosan was dissolved in 50 mL of deionized double-distilled water. Furthermore, 15 g of EDTA was added to 20 mL deionized double-distilled water, and the pH value was kept constant at pH 8 by continuously adding 5M sodium hydroxide until EDTA was completely dissolved. Deionized double-distilled water was added to make a final volume of 50 mL. Thereafter, the abovementioned solutions were mixed evenly under stirring and the pH value was adjusted to 6.0 with 5 M sodium hydroxide. In order to catalyse the formation of amide bonds between the amino groups of glycol chitosan and the carboxyl groups of EDTA, EDAC was added at a final concentration of 0.1 M. The reaction mixture was incubated at room temperature under continuous stirring for 14 h. The resulting conjugate was isolated by exhaustive dialyzing against 0.05 M sodium hydroxide and then exhaustively against deionized double-distilled water. The purified product was lyophilized and stored at  $-20\text{ }^{\circ}\text{C}$  until use.

### 6.2.2.3. Synthesis of superparamagnetic iron oxide nanoparticles

For coprecipitation, ferrous chloride tetrahydrate ( $\text{FeCl}_2 \cdot 4\text{H}_2\text{O}$ ), ferric chloride hexahydrate ( $\text{FeCl}_3 \cdot 6\text{H}_2\text{O}$ ), and sodium hydroxide (NaOH,) were used. The desired NaOH solutions (5.5, 8.5, and 14.5 M) were prepared and stored before the synthesis. 0.99gm of  $\text{FeCl}_2$  and 2.7 g of  $\text{FeCl}_3$  were dissolved in 50 ml de-ionized water and then 10 ml NaOH solution was added to the mixture of iron salts under a vigorous mechanical stirring. The reaction period was 30 minutes at room temperature in an air medium. After the reaction, the precipitate was washed three times with distilled water and was dried in an oven. The

precipitate can be obtained in a basic medium. The structural and magnetic properties of these nanoparticles depend on the synthesis conditions such as base concentration, stirring rate, etc<sup>246</sup>.

#### 6.2.2.4. Preparation of nanobubbles with different polymer shells for iron chelation

In ethanol, Epikuron 200<sup>®</sup> (2.5 % w/v) and palmitic acid (0.5 % w/v) as a co-surfactant were dissolved. In an ice bath, 300  $\mu$ L of Epikuron and the palmitic acid mixture were added to 400 $\mu$ L of Decafluoropentane. Then, drop by drop, the appropriate amount of water was added to the mixture. A high-shear homogenizer (Ultra-Turrax<sup>®</sup>) was used to homogenize the system for 2 minutes until a nanoemulsion is formed. The nanoemulsion was then saturated at 37°C. After those different polymers such as 2.7% chitosan, 2% Dextran sulfate, 2.7% Glycol chitosan, 2.7% Glycolchitosan + EDTA, and 2.7% Glycol-chitosan Deferoxamine was added dropwise to produce the nanobubbles (NB) polymeric shell to evaluate their iron chelation capacity

#### 6.2.2.5. Superparamagnetic iron oxide nanoparticles loaded Nanobubbles (MNBs)

The same recipe for NBs fabrication was followed, but finally, 1 mg/mL of SPIONs suspension were added to NBs under stirring, to obtain MNBs.

#### 6.2.2.6. Bilirubin loaded Glycol chitosan Deferoxamine nanobubbles.

In ethanol, Epikuron 200<sup>®</sup> (2.5 % w/v) and palmitic acid (0.5 % w/v) as a co-surfactant were dissolved. In an ice bath, 300 $\mu$ L of Epikuron and palmitic acid mixture and 125 $\mu$ g bilirubin in 50 $\mu$ L of DMSO<sub>4</sub> were added to 350 $\mu$ L of Decafluoropentane. Then, drop by drop, the appropriate amount of HEPES buffer (pH:7.4) was added to the mixture. A high-shear homogenizer (Ultra-Turrax<sup>®</sup>) was used to homogenize the system for 2 minutes until a nanoemulsion formed. The nanoemulsion was then saturated at 37°C. After that, an aqueous solution of Glycol-chitosan Deferoxamine (2.7% w/v) was added dropwise to produce the nanobubbles (NB) polymeric shell. Finally, 1 mg/mL of SPIONs suspension were added to NB under stirring, to obtain MOLNBs.

#### 6.2.2.7. Structural characterization of the synthesized derivative of Glycol-Chitosan+ Deferoxamine

##### 6.2.2.7.1. FTIR spectroscopy:

The structure of organic compounds is determined using FT-IR Technique. This is carried out by molecules absorbing infra-red light in the region of 4000-650  $\text{cm}^{-1}$ . The change in



energy is measured by observing the vibration of the molecules. Potassium bromide (KBr) discs with all the samples were prepared using an electrically operated KBr press model.

#### 6.2.2.7.2. Nuclear Magnetic Resonance ( $^1\text{H}$ NMR)

It is another technique used to identify the structure of a compound. It can be used to provide the basic carbon structure of a compound by measuring the absorbance of electromagnetic radiation under a magnetic field by observing the nucleus spin. The ability of NMR (Nuclear Magnetic Resonance) to provide information regarding the specific bonding structure and stereochemistry of molecules of pharmaceutical interest has made it a powerful analytical instrument for structural elucidation. The ability of NMR-based diffusion coefficient determination to distinguish between monomeric and dimeric substances was validated using a standard mixture of authentic materials containing both monomers and dimers.

#### 6.2.2.8. Physicochemical analysis

The mean hydrodynamic diameter, polydispersity index (PDI), and zeta potential of the SPIONs and MNBs were measured by dynamic light scattering spectroscopy (DLS) at room temperature. The samples were diluted with ultrapure water in an electrophoretic cell. Each measured value was the average of ten reciprocal, an electric field of 15 V/m was used for zeta potential determination. Photon correlation spectroscopy (PCS) with a scattering angle of  $90^\circ$ , the temperature of  $25^\circ\text{C}$  using a 90 Plus instrument (Brookhaven, NY, USA) was used. The viscosity of the NBs formulation was determined at  $25^\circ\text{C}$  using a capillary viscosimeter. The osmolarity was determined at  $25^\circ\text{C}$  using an osmometer.

#### 6.2.2.9. Iron chelation Studies

Iron chelation experiments were carried out using 100 PPM iron solutions ( $\text{Fe}^{+2}$  and  $\text{Fe}^{+3}$ ) in water and nanobubbles with various polymeric shells and SPIONs loaded. UV absorbance methods such as the Ferrozine assay and the Desferoxamine assay were developed for Chelation studies. 1ml of prepared polymeric nanobubbles were mixed into the  $\text{Fe}^{+2}$  and  $\text{Fe}^{+3}$  solutions for 90 minutes at room temperature. The solution was then centrifuged at 2000 RPM for 10 minutes, and the supernatant was separated and analyzed using UV absorbance spectroscopy.

#### 6.2.2.9.1. Ferrozine assay

The ferrozine reacts with divalent iron to form a stable magenta complex species. UV-visible spectrophotometry method was developed for the determination of iron present in the solution. 1 Molar ferrozine solution prepared and stored at room temperature. Ammonium acetate (pH 9.2) was used as a buffer. Take 1ml aliquot of the Iron (II) into the Eppendorf and add 100 $\mu$ L of 1 Molar ferrozine solution and 50 $\mu$ L of ammonium buffer. Kept the solution at a dark place for 30 minutes and analyzed at 562nm by using Beckman Coulter DU 730 Spectrometer.

#### 6.2.2.9.2. Deferoxamine assay

Desferrioxamine B mesylate are used to determine the trivalent iron. 1 Molar Desferrioxamine B mesylate solution is prepared and stored at room temperature. Take 1ml aliquot of the Iron (III) into the Eppendorf and add 100 $\mu$ L of 1 Molar Desferrioxamine B mesylate. Kept the solution at a dark place for 30 minutes and analyzed at 293nm by using Beckman Coulter DU 730 Spectrometer.

The following equation was used for the calculation of the percentage reduction of metal ion

concentration for the lyophilized as well as Nano scaled materials

$$\text{Percentage iron chelation} = \frac{C_{\text{initial}} - C_{\text{final}}}{C_{\text{initial}}} \times 100$$

where,

$C_{\text{initial}}$  is the initial concentration of the untreated Iron Solutions

$C_{\text{final}}$  is the concentration of after polymeric nanobubbles treatment

#### 6.2.2.10. Haemolytic activity

The haemolytic activity of MOLNBs was evaluated on rat blood. Blood was diluted 1:10 with PBS (pH 7.4). Triton x 100 1% was used as a positive control, where red blood cell breakage and further release of hemoglobin occurred. Saline solution (NaCl 0.9% w/v) was used as negative control. 1 mL of all samples were prepared (1:10, 1:100, 1:200, 1:400 dilution) and incubated for 90min at 37 C. Then, samples were centrifuged for 5 min at 2000 rpm and the supernatant was analyzed with an ultraviolet-visible spectrophotometer (DU 730, Beckman Coulter, Fullerton, CA) at= 543 nm. The percentage of hemolysis was calculated using the positive control as 100% homolysis<sup>247</sup>.

#### 6.2.2.11. Evaluation of antioxidant activity

TBA assay. This assay is based on the oxidative decomposition of polyunsaturated fatty acid in an acidic medium to generate malondialdehyde (MDA), which reacts with TBA to form TBA-MDA adduct<sup>248</sup>.

0.1 ml of linoleic acid (1% w/v) was taken in a test tube, 0.2 ml of sodium dodecyl sulfate (SDS) (4% w/v), 1.5 ml of phosphoric acid (1.0% v/v), 1.0 ml of TBA (0.6% w/v), 0.1 ml of water and 0.1 ml of an Iron solution of different concentration and iron chelated nanobubbles was added into it. The mixture was heated at 100 °C for 45 min later it was cooled down on an ice bath and mixed with 1-butanol (4 ml) to extract TBA-MDA adduct. Samples were analyzed by UV-vis spectrophotometer (DU 730, Beckman Coulter, Fullerton, CA at 535 nm.

#### 6.2.2.12. Quantitative determination of Bilirubin by HPLC method

The quantitative determination of Bilirubin was performed by an HPLC system (Shimadzu) equipped with a UV detector (Flexar UV/Vis LC spectrophotometer) using a Phenomenex C18 analytical column (4.6mmx 250 mm, 5 µm). The mobile phase consisted of a mixture of Water: Methanol (1:99 v/v), filtered and ultrasonically degassed before use. The mobile phase was pumped through the column at a flow rate of 1 ml/min and the samples (20 µl) were analyzed at 440 nm using a UV detector.

#### 6.2.2.13. In Vitro Cytotoxicity Study

The organotypic brain cultures cells (Substantia nigra) were used to perform in vitro cytotoxicity test. Cells were seeded in 6-well plates and incubated at 37 °C, 5% CO<sub>2</sub> for one week in a Complete culture medium. Change the medium the day after and every 2 days after on. Then, the cells were treated with GC-DFO, GC-DFO+SPIONs, GC-DFO+SPIONs (after chelation), in a series of dilutions with medium (1:64 to 1:11428). After 24 hours incubation, viable cells were evaluated by 2,3-bis [2-methoxy-4-nitro- 5sulphophenyl]-2Htetrazolium-5carboxanilide (MTT) inner salt reagent at 570 nm, immunofluorescence and lactate dehydrogenase (LDH). The control cells were normalized to 1 and the readings from treated cells were expressed as cell viability. Seven biological replicates were used to determine each data point.

### 6.3. Results

#### 6.3.1. Structural characterization of the synthesized derivative of Glycol-Chitosan+ Deferoxamine

##### 6.3.1.1. FT-IR spectroscopy:

The FTIR spectra of GC, DFO, and GC DFO, were recorded on PerkinElmer 100 FTIR using an attenuated total reflectance (ATR) accessory. All the samples were scanned from 4000-650  $\text{cm}^{-1}$  at a resolution of 4  $\text{cm}^{-1}$  and 8 scans/spectrum.

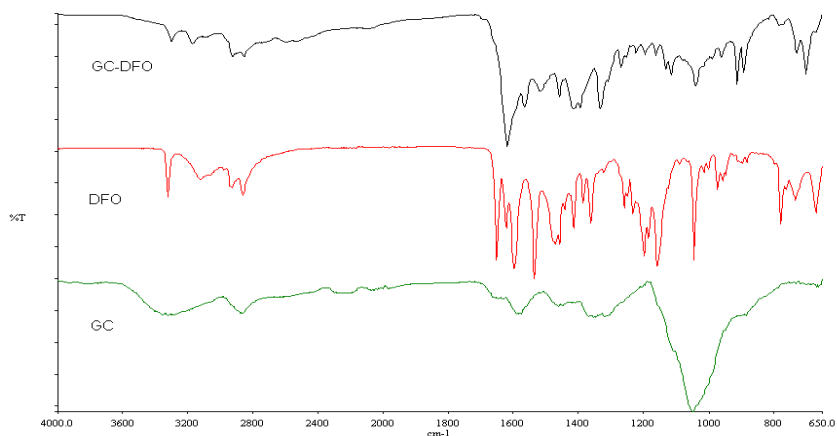


**Figure 6.2:** FTIR Spectra of GC, DFO, and Gc-DFO

**Table 6.1:** Principal IR peaks for GC-DFO

Wavenumber ( $\text{cm}^{-1}$ )	Functional group
1100	Alkyl amine
1620	Diketone
2900	(C-H) Alkane

##### 6.3.1.2. Structure conformation of GC-DFO from NMR

With the help of NMR Spectra, we conform the GC-DFO conjugation.

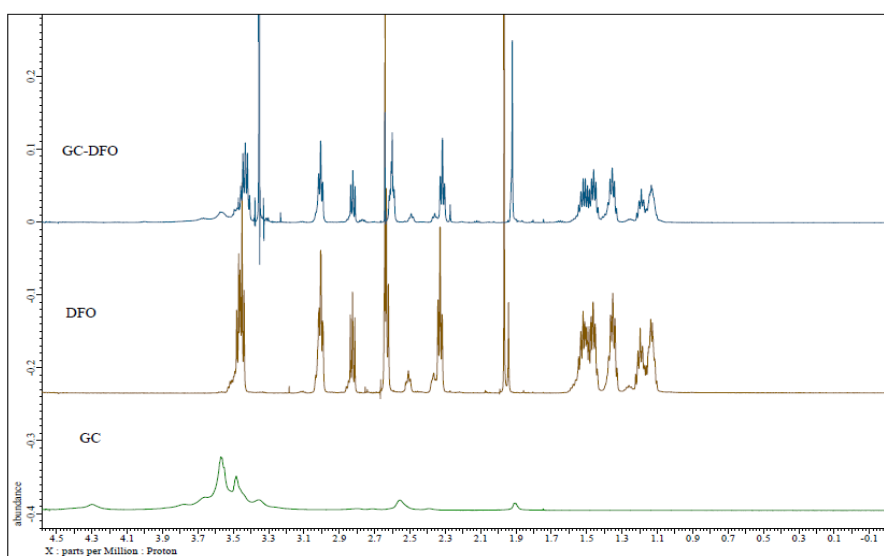


**Figure 6.3:**  $^1\text{H}$  NMR Spectra of GC-DFO

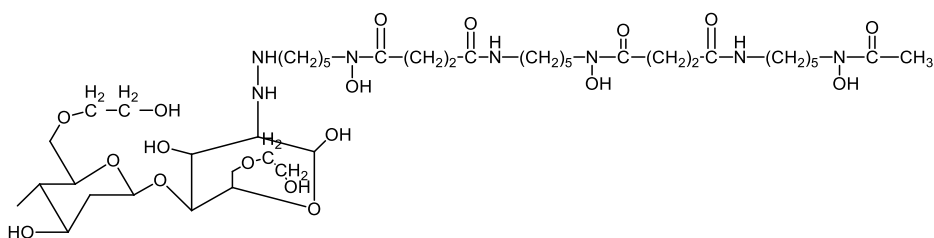


**Figure 6.4:** Structure of GC-DFO

### 6.3.2. Physicochemical Characterization of Formulations

Table 2 summarizes the physicochemical characterization of all formulations. The negative and positive values of the zeta potential represent the GC-DFO and Chitosan fingerprints on the NB surface, respectively. SPIONs average zeta potential was measured to be +22.24 mV. The positive charge of SPIONs is suitable for electrostatic interactions with the negatively charged GC-DFO polymer shell. The polymer shell surface's zeta potential was lowered by 45% when SPIONs were bound to it. The pH, viscosity, and osmolarity of the nanosuspension were all 6, 0.98 cP, and 354 mOsm, respectively. The presence of SPIONs on the NB surface had no effect on these parameters. Furthermore, OLNBS demonstrated homogeneous size and stability throughout three months.

**Table 6.2.** Physicochemical characteristics of different nanocarriers formulations. Data reported as Mean  $\pm$  Standard Deviation.

formulation	Average diameter $\pm$ SD (nm)	PDI	Zeta potential PZ $\pm$ SD (mV)
Chitosan NBs	319 $\pm$ 7.6	0.304 $\pm$ 0.01	+29.66 $\pm$ 3.18
GC-DFO	359.7 $\pm$ 5.8	0.311 $\pm$ 0.08	-32.49 $\pm$ 1.35
GC-EDTA	320.1 $\pm$ 2.3	0.224 $\pm$ 0.18	-24.17 $\pm$ 3.70
SPIONs	18.6 $\pm$ 2.3	0.264 $\pm$ 0.02	+22.24 $\pm$ 3.37
GC-DFO+ SPIONs	384.8 $\pm$ 7.6	0.257 $\pm$ 0.01	-20.14 $\pm$ 6.40
Dextran NBs	341.2 $\pm$ 11.7	0.22 $\pm$ 0.10	-33.36 $\pm$ 2.13
Dextran +SPIONs	349.2 $\pm$ 18.2	0.21 $\pm$ 0.01	-20.41 $\pm$ 8.60

### 6.3.3. Iron Chelation

Iron chelation studies were performed with two different iron solutions such as Fe<sup>+2</sup> and Fe<sup>+3</sup> at 100 PPM to determine the absorption capacity of different polymeric shell NBs.

Table 6.5 showed the percentage of Fe<sup>+2</sup> and Fe<sup>+3</sup> chelation. Table 6.6 showed the GC-DFO chelation capacity at different Fe<sup>+3</sup> concentrations.

**Table 6.3:** UV absorbance for Fe<sup>+2</sup>

Concentration (PPM)	Absorbance (562nm)
0	0 ± 0.0
0.5	0.210 ± 0.01
1	0.422 ± 0.01
1.5	0.616 ± 0.04
2	0.759 ± 0.10
2.5	0.924 ± 0.13

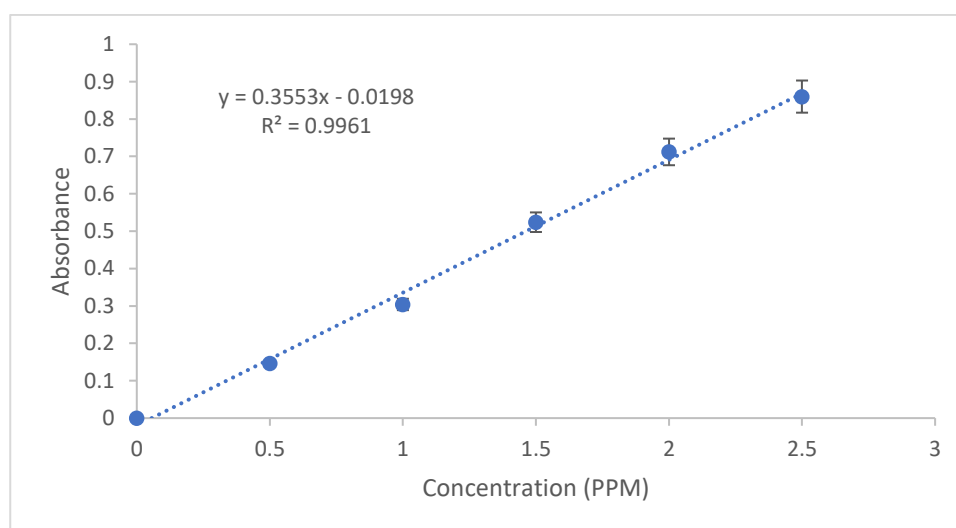


**Figure 6.5:** Standard plot for Fe<sup>+2</sup>

**Table 6.4:** UV absorbance for Fe<sup>+3</sup>

Concentration (PPM)	Absorbance (293nm)
0	0 ± 0.0
5	0.179 ± 0.08
10	0.358 ± 0.13
15	0.448 ± 0.17
20	0.620 ± 0.22
25	0.778 ± 0.23
30	0.872 ± 0.24

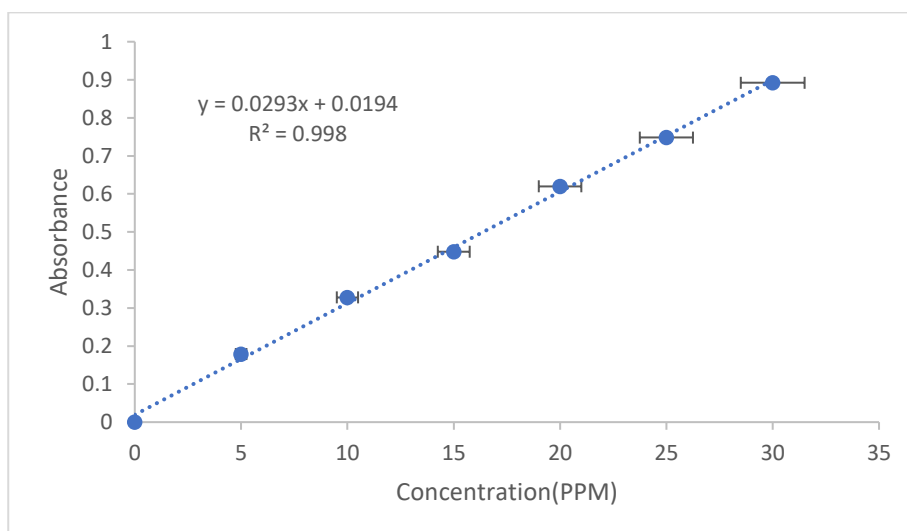


**Figure 6.6:** Standard plot for Fe<sup>+3</sup>

**Table 6.5:** Iron chelation

NBs Formulation	% Of Fe <sup>+3</sup> chelation	% Of Fe <sup>+2</sup> chelation
CS-NBs	55.65	88.35
GC-DFO	94.32	52.16
GC-EDTA	62.25	97.22
Dextran NBs	45.84	78.21
Glycol Chitosan NBs	29.43	55.32
DEX-DFO NBs	33.47	38.18
CS NBs+ DFO SPIONs	64.92	45.16
GC-DFO+ SPIONs (Blank)	93.63	58.19

**Table 6.6:** Iron Chelation with different iron concentration

Iron concentration (PPM)	% Of Chelation (GC-DFO NBs)
5	100
10	100
15	100
20	100
25	99
30	98

#### 6.3.4. Hemolytic Activity

MOLNB aqueous suspensions examined at various dilutions (1:10, 1:100, 1:200, and 1:400 v/v) exhibited no significant hemolytic activity, resulting in negligible red blood cell destruction as compared to the control. These findings indicate that this nanoformulation is biocompatible and acceptable for prospective in vivo delivery without hemolysis.

### 6.3.5. Antioxidant activity

The generation of MDA because of the degradation of fatty acid is a common indicator for determining the degree of lipid peroxidation. MDA reacts with TBA to produce a pink TBA-MDA adduct. The production of MDA is shown in Figure 6.7 and it was observed that after iron chelation DFO shelled NBs produced a lesser amount of MDA ( $P < 0.001$ ) compared to free iron. A decreased production of MDA might be because of the inhibiting of GC-DFO NBs after chelation on ROS produced during the oxidation process.

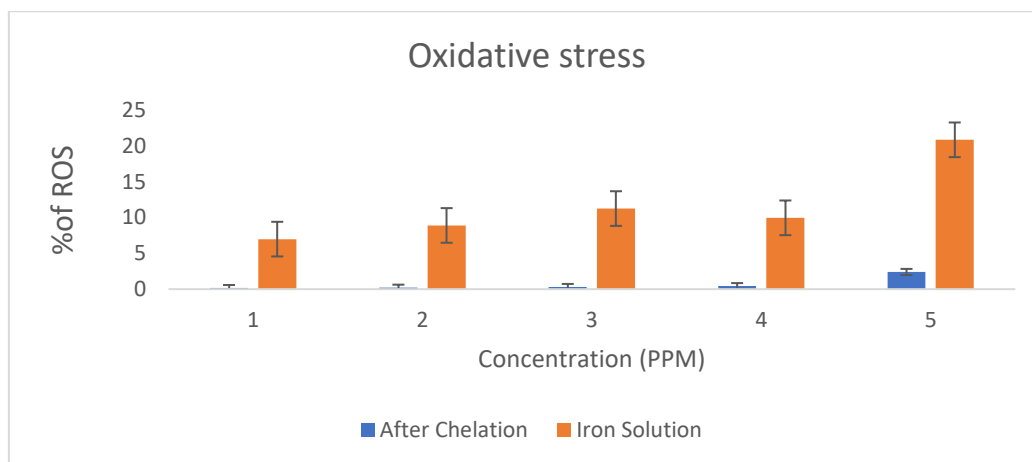


**Figure 6.7:** Antioxidant activity

### 6.3.6. Quantitative determination of Bilirubin by HPLC method

By using a sophisticated HPLC analytical technique we determine the concentration of bilirubin inside the NBs at 4.119 retention time.

**Table 6.7:** Bilirubin concentration

Sample Name	Concentration ( $\mu\text{molar}$ )
GC-Bilirubin	32.30
GC-DFO+Bilirubin	33.75



### 6.3.7. In-vitro cytotoxicity

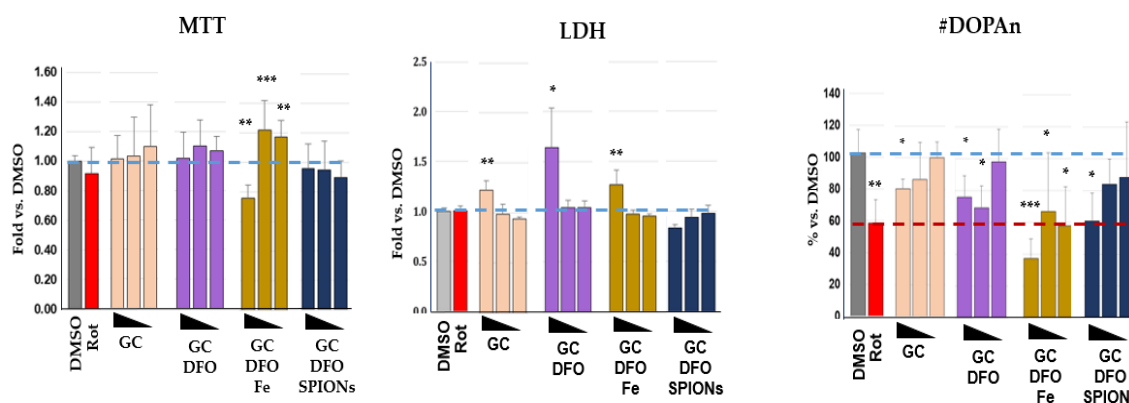


**Figure 6.8:** Viability of cell after 24 hours treatment, MTT, LDH, and DOPAn count

### 6.4. Discussion

Successful post-polymerization modification of the dioxolane groups to form reactive aldehyde groups was achieved without degradation or cross-linking of the copolymer. The availability of the aldehyde groups along the polymer backbone to form stable conjugates with amine-containing molecules was confirmed via a reaction with the iron-chelating drug Desferrioxamine (DFO). Sophisticated analytical technique such as NMR and FT-IR was used to confirm the GC-DFO conjugation<sup>245</sup>.

MOLNBs are stable nanosystems with a well-defined hollow structure and a shell extensively adorned with SPIONs. The inclusion of SPIONs has no significant effect on their average diameter or polydispersity index, whereas the zeta potential is reduced yet still effective in preventing aggregation occurrences. This behaviour revealed that SPIONs had a good electrostatic interaction with the negatively charged NB shell. SPIONs and NB combine to generate stable nanosystems. Furthermore, the surface negative charge makes MOLNBs promising candidates to efficiently cross the BBB, being the zeta potential a crucial parameter for brain delivery<sup>247</sup>.

The human brain is the central organ of the body and it is protected by a series of multiple barriers such as the blood-cerebrospinal fluid (CSF) barrier and blood-brain barrier (BBB). CSF reflects the central nervous system's biochemical state under different physiological and pathological conditions. This makes CSF a potential candidate for identifying novel early biomarkers for neurological diseases, The abnormal level of traces of elements (Al, Cu, Mn, Fe, Zn, Hg, Cr) in CSF as precursors of clinically symptomatic dementia. Table 6.5

and Table 6.6 showed that our prepared magnetic nanobubbles (GC-DFO) polymeric shells were able to chelate approximately 90% of the excess iron and reduce the burden.

By using the HPLC method we determined the bilirubin concentration inside the nanobubbles. A small amount of bilirubin like the micromolar concentration of bilirubin is able to neutralize the 10,000 times higher levels of cellular ROS by reducing ROS, UCB may inhibit the N-methyl-D-aspartate (NMDA) excitotoxicity, preventing neuronal death<sup>249</sup>.

The absence of hemolytic activity of MOLNBs is an important aspect, being a key parameter for assessing the safety of the nanocarrier and biocompatibility, and is strictly required for intravenous administration in early preclinical development.

With the help of Thiobarbituric (TBA assay) acid assay we confirmed that our prepared magnetic oxygen loaded nanobubbles has antioxidant activity, Figure 6.7 showed how nanobubbles chelate the iron and reduced the reactive oxygen species (ROS).

MTT, LDH, and Immunofluorescence cytotoxicity assay were performed on organotypic brain cell culture. We confirmed that our nanobubbles formulation (GC, GC-DFO, and GC-DFO-SPIONs and MOLNBS (after chelation)) at the higher dilution tested (1:192) are safe.

## 6.5. Conclusion

we propose a novel system of chelation therapy through the use of nanocarriers conjugated to chelators, which show a unique ability to cross the blood-brain barrier (BBB), to chelate metals, and to escape across the BBB with their corresponding complexed metal ions. This method may provide a safer and more effective means of reducing the metal load in neural tissue, thus attenuating the harmful effects of oxidative damage and its sequelae. We prepared and characterized the physicochemical properties and cytotoxicity of Magnetic oxygen-loaded nanobubbles functionalizing by different polymers shells such as Chitosan, Dextran Sulphate, Glycol-chitosan-EDTA and Glycol-chitosan Deferoxamine, and perfluoropentane-cored nanobubbles with superparamagnetic iron oxide nanoparticles. Magnetic oxygen-loaded nanobubbles with sizes of about 380 nm were manufactured, able to store oxygen and chelate excess iron. Their toxicity was evaluated on organotypic brain cultures (substantia nigra)

## Chapter 7: Conclusions

### 7.1. Conclusion

The overall scope of this work is the design and formulation of new polymeric nanocarriers to chelate the excess iron and overcome the blood-brain barriers. Because of driven by the external magnetic field, IONPs are considered one of the most promising technologies for biomedical applications due to their unique physicochemical features. IONPs, in particular, could be suitable for physical targeting of the CNS, allowing for better BBB crossing and medication administration into the brain. As a result, research in the production of tailored IONPs using controllable synthesis methods and careful adjustment of their properties is ongoing. about potential tactics for designing suitable IONPs that can progress from proof-of-concept to clinical settings in the future. Adjusting the parameters of the synthesis process is the first needed step in ensuring an accurate selection of physicochemical features such as size, shape, and structure. At the same time, improving numerous biomedical applications in the CNS requires the functionalization of IONPs with different polymers or chemical compounds. We have started with the preparation of superparamagnetic oxygen-loaded nanobubbles (in chapter.3). In a cancer cellular model, we produced and analyzed superparamagnetic theranostic OLNBS with echogenicity, heating potential, and internalization capability. Magnetic oxygen-loaded nanobubbles could be a novel fascinating nanotool for multifaceted tumor treatment, generating HT and releasing oxygen as a radiosensitizer for RT when exposed to an RF magnetic field. This nanoformulation could offer a new way to improve cancer treatment outcomes by allowing cancer cells to be killed locally by heating tumor tissues to hyperthermic temperatures.

In chapter.4 we have studied the biocompatibility of nanoformulation and the magnetically driven capacity with the help of an external magnetic field and US Sonography. This work is a good starting point for developing the system able to cross the BBB. MOLNBS are stable nanosystems showing a well-defined hollow structure, whose shell is densely decorated by SPIONs, as indicated by TEM analysis. The addition of SPIONs does not significantly increase neither their average diameter nor the polydispersity index, while the zeta potential is decreased but the value is still effective in preventing aggregation phenomena. This behavior suggested a good electrostatic interaction of SPIONs with the negatively charged NB shell. Furthermore, the surface negative charge makes MOLNBS promising candidates to efficiently cross the BBB, being the zeta potential a crucial parameter for brain delivery.

The absence of haemolytic activity of MOLNBs is an important aspect, being a key parameter for assessing the safety of the nanocarrier and biocompatibility, and is strictly required for intravenous administration in early preclinical development. In vitro cytotoxicity assay and confocal microscopy images indicate that MOLNBs interact in a non-toxic way with hBMECs and are localized in the cytoplasm compartment of the cells, as a result of internalization. These results highlight the potentiality of MOLNBs to enter in the CNS cells. These results support our initial speculation since MOLNBs might be safely administrated either systemically or locally via intravertebral injection in the CSF, monitoring their concentration by MRI or sonography. Then we focused on (Chapter. 5) preparation of multifunctional nanovectors for radio-chemo-hyperthermic therapy under physical targeting. While investigating the possible synergistic effect of the conventional anticancer therapies, which, taken individually, are often ineffective against critical tumors, such as central nervous system (CNS) ones, the design of theranostic nanovectors able to carry and deliver chemotherapy drugs and magnetic hyperthermic agents to the target radiosensitizers (oxygen) was pursued. The cell viability studies confirmed that these multifunctional nanovectors can act as drug delivery systems, improving the effectiveness of the encapsulated drugs, e.g., DOX in OLNBs, which promoted a synergistic antitumor effect, and curcumin-loaded OLNBs, which improved the inhibition of tumor cell viability. The nanosystems are very flexible and could be easily designed for administrating a large variety of different drugs. Nanostructure's specific magnetic properties greatly enhance their potentiality either for diagnosis (MRI imaging, in addition to US), therapy (hyperthermia), or the possibility of physical targeting of tissues by exploiting the magnetic driving. Other indirect advantages are also expected, e.g., the temperature in the hyperthermic range induces a marked change in oxygen release over time, with increases in the external aqueous solution oxygen concentration of up to 0.5–1 mg/L. This oxygenation effect might further enhance the therapeutic outcome when hyperthermia is combined with radiation therapy. Thus, MOLNBs could represent a promising nanoplatform for applications to fulfill non-trivial therapeutic needs, such as those related to head and neck tumors, pancreatic tumors, and CNS pathologies. our results seem to encourage the possibility of non-systemic administration approaches, e.g., the feasibility of some magnetic driving of the MOLNBs from the brain ventricles (filled by the cerebrospinal fluid (CSF), in which MOLNBs could be injected from the intravertebral

spaces) to the nearby tumors to which the cargoes have to be delivered. The contact of CSF with the CNS makes it an attractive medium for drug delivery, circumventing systemic barriers.

As shown in chapter 6 we synthesized the derivative of a polymer such as GC-DFO to use as a polymer shelled for NBs and to improve the iron chelation capacity. Our study introduced a new potent iron chelation nanoformulation, that can cross the BBB and inhibit iron induce mitochondrial membrane lipid peroxidation, and can protect neurons. we propose a novel system of chelation therapy through the use of nanocarriers conjugated to chelators, which show a unique ability to cross the blood-brain barrier (BBB), to chelate metals, and to escape across the BBB with their corresponding complexed metal ions. This method may provide a safer and more effective means of reducing the metal load in neural tissue, thus attenuating the harmful effects of oxidative damage and its sequelae. Obviously, more work is needed to better understand the role of iron in the pathogenesis of neurological disorders and to design therapeutic agents for more effective management.

## 7.2. What's next

In this Ph.D. thesis, we studied how iron chelation is helpful to reduce the oxidative burden and metal load in neural tissue. We would like to combine this iron chelation therapy with some drug and biological samples such as bilirubin to protect neurons from damage and improve neural health. To do this we already started the collaboration with Fondazione Italiana Fegato Onlus. They are working organotypic brain cultures (substantia nigra) and PD models. Bilirubin has the ability to neutralize 10,000 times higher levels of cellular ROS by reducing ROS. It will be helpful to improve the dopaminergic neurons count in neurological disorders.

## 8. References

- (1) Gitler, A. D.; Dhillon, P.; Shorter, J. Neurodegenerative Disease: Models, Mechanisms, and a New Hope. *DMM Dis. Model. Mech.* **2017**, *10* (5), 499–502. <https://doi.org/10.1242/dmm.030205>.
- (2) Lynch, C. World Alzheimer Report 2019: Attitudes to Dementia, a Global Survey. *Alzheimer's & Dementia*. September 20, 2020. <https://doi.org/10.1002/alz.038255>.
- (3) Prevalence\_of\_dementia\_and\_major\_subtypes\_in\_Europe\_A\_collaborative\_study\_ [https://www.researchgate.net/publication/12464923\\_Prevalence\\_of\\_dementia\\_and\\_major\\_subtypes\\_in\\_Europe\\_A\\_collaborative\\_study\\_of\\_population-based\\_cohorts](https://www.researchgate.net/publication/12464923_Prevalence_of_dementia_and_major_subtypes_in_Europe_A_collaborative_study_of_population-based_cohorts) (accessed Sep 8, 2021).
- (4) Armstrong, R. What Causes Neurodegenerative Disease? *Folia Neuropathol.* **2020**, *58* (2), 93–112. <https://doi.org/10.5114/FN.2020.96707>.
- (5) Oboudiyat, C.; Glazer, H.; Seifan, A.; Greer, C.; Isaacson, R. S. Alzheimer's Disease. *Semin. Neurol.* **2013**, *33* (4), 313–329. <https://doi.org/10.1055/s-0033-1359319>.
- (6) 2016 Alzheimer's Disease Facts and Figures. *Alzheimers. Dement.* **2016**, *12* (4), 459–509. <https://doi.org/10.1016/J.JALZ.2016.03.001>.
- (7) Lane, C. A.; Hardy, J.; Schott, J. M. Alzheimer's Disease. *Eur. J. Neurol.* **2018**, *25* (1), 59–70. <https://doi.org/10.1111/ene.13439>.
- (8) Sheppard, O.; Coleman, M. Alzheimer's Disease: Etiology, Neuropathology and Pathogenesis. *Alzheimer's Dis. Drug Discov.* **2020**, 1–22. <https://doi.org/10.36255/exonpublications.alzheimersdisease.2020.ch1>.
- (9) Tiwari, S.; Atluri, V.; Kaushik, A.; Yndart, A.; Nair, M. Alzheimer's Disease: Pathogenesis, Diagnostics, and Therapeutics. *Int. J. Nanomedicine* **2019**, *14*, 5541–5554. <https://doi.org/10.2147/IJN.S200490>.
- (10) Wadghiri, Y. Z.; Sigurdsson, E. M.; Sadowski, M.; Elliott, J. I.; Li, Y.; Scholtzova, H.; Tang, C. Y.; Aguinaldo, G.; Pappolla, M.; Duff, K.; Wisniewski, T.; Turnbull, D. H. Detection of Alzheimer's Amyloid in Transgenic Mice Using Magnetic Resonance Microimaging. *Magn. Reson. Med.* **2003**, *50* (2), 293–302. <https://doi.org/10.1002/mrm.10529>.
- (11) Briggs, R.; Kennelly, S. P.; O'Neill, D. Drug Treatments in Alzheimer's Disease. *Clin. Med. J. R. Coll. Physicians London* **2016**, *16* (3), 247–253. <https://doi.org/10.7861/clinmedicine.16-3-247>.
- (12) Beitz, J. M. Parkinson's Disease: A Review. *Front. Biosci. - Sch.* **2014**, *6 S* (1), 65–74. <https://doi.org/10.2741/s415>.
- (13) Samii, A.; Nutt, J. G.; Ransom, B. R. Parkinson's Disease. *Lancet* **2004**, *363* (9423), 1783–1793. [https://doi.org/10.1016/S0140-6736\(04\)16305-8](https://doi.org/10.1016/S0140-6736(04)16305-8).
- (14) Gelb, D. J.; Oliver, E.; Gilman, S. Diagnostic Criteria for Parkinson Disease. *Arch. Neurol.* **1999**, *56* (1), 33–39. <https://doi.org/10.1001/archneur.56.1.33>.
- (15) Gibb, W. R. G.; Lees, A. J. The Relevance of the Lewy Body to the Pathogenesis of Idiopathic Parkinson's Disease. *J. Neurol. Neurosurg. Psychiatry* **1988**, *51* (6), 745–752.

- <https://doi.org/10.1136/jnnp.51.6.745>.
- (16) Tolosa, E.; Wenning, G.; Poewe, W. The Diagnosis of Parkinson's Disease. *Lancet Neurol.* **2006**, *5* (1), 75–86. [https://doi.org/10.1016/S1474-4422\(05\)70285-4](https://doi.org/10.1016/S1474-4422(05)70285-4).
- (17) Aarsland, D.; Beyer, M. K.; Kurz, M. W. Dementia in Parkinson's Disease. *Curr. Opin. Neurol.* **2008**, *21* (6), 676–682. <https://doi.org/10.1097/WCO.0b013e3283168df0>.
- (18) Sadrzadeh, S. M. H.; Saffari, Y. Iron and Brain Disorders. *Am. J. Clin. Pathol.* **2004**, *121* Suppl (Suppl 1). <https://doi.org/10.1309/ew0121lg9n3n1yl4>.
- (19) Liu, J. L.; Fan, Y. G.; Yang, Z. S.; Wang, Z. Y.; Guo, C. Iron and Alzheimer's Disease: From Pathogenesis to Therapeutic Implications. *Front. Neurosci.* **2018**, *12* (SEP), 632. <https://doi.org/10.3389/fnins.2018.00632>.
- (20) Beard, J. L.; Connor, J. R. Iron Status and Neural Functioning. *Annu. Rev. Nutr.* **2003**, *23*, 41–58. <https://doi.org/10.1146/annurev.nutr.23.020102.075739>.
- (21) Iron deficiency and neural development: an update - PubMed <https://pubmed.ncbi.nlm.nih.gov/10971834/> (accessed Sep 20, 2021).
- (22) COOK, J. D.; SKIKNE, B. S. Iron Deficiency: Definition and Diagnosis. *J. Intern. Med.* **1989**, *226* (5), 349–355. <https://doi.org/10.1111/j.1365-2796.1989.tb01408.x>.
- (23) Halliwell, B.; Gutteridge, J. M. C. Oxygen Toxicity, Oxygen Radicals, Transition Metals and Disease. *Biochem. J.* **1984**, *219* (1), 1–14. <https://doi.org/10.1042/bj2190001>.
- (24) W, van G.; MI, H.-H.; MI, C.-S.; JP, van D.; HG, van E. Iron Uptake in Blood-Brain Barrier Endothelial Cells Cultured in Iron-Depleted and Iron-Enriched Media. *J. Neurochem.* **1998**, *71* (3), 1134–1140. <https://doi.org/10.1046/J.1471-4159.1998.71031134.X>.
- (25) Zecca, L.; Youdim, M. B. H.; Riederer, P.; Connor, J. R.; Crichton, R. R. Iron, Brain Ageing and Neurodegenerative Disorders. *Nature Reviews Neuroscience*. Nature Publishing Group November 2004, pp 863–873. <https://doi.org/10.1038/nrn1537>.
- (26) Mastroberardino, P. G.; Hoffman, E. K.; Horowitz, M. P.; Betarbet, R.; Taylor, G.; Cheng, D.; Na, H. M.; Gutekunst, C. A.; Gearing, M.; Trojanowski, J. Q.; Anderson, M.; Chu, C. T.; Peng, J.; Greenamyre, J. T. A Novel Transferrin/TfR2-Mediated Mitochondrial Iron Transport System Is Disrupted in Parkinson's Disease. *Neurobiol. Dis.* **2009**, *34* (3), 417–431. <https://doi.org/10.1016/j.nbd.2009.02.009>.
- (27) Horowitz, M. P.; Greenamyre, J. T. Mitochondrial Iron Metabolism and Its Role in Neurodegeneration. *J. Alzheimer's Dis.* **2010**, *20* (SUPPL.2), S551. <https://doi.org/10.3233/JAD-2010-100354>.
- (28) Ward, R. J.; Zucca, F. A.; Duyn, J. H.; Crichton, R. R.; Zecca, L. The Role of Iron in Brain Ageing and Neurodegenerative Disorders. *Lancet Neurol.* **2014**, *13* (10), 1045–1060. [https://doi.org/10.1016/S1474-4422\(14\)70117-6](https://doi.org/10.1016/S1474-4422(14)70117-6).
- (29) Liu, J. L.; Fan, Y. G.; Yang, Z. S.; Wang, Z. Y.; Guo, C. Iron and Alzheimer's Disease: From Pathogenesis to Therapeutic Implications. *Front. Neurosci.* **2018**, *12* (SEP), 1–14. <https://doi.org/10.3389/fnins.2018.00632>.
- (30) Benarroch, E. E. Brain Iron Homeostasis and Neurodegenerative Disease. *Neurology*



- 2009**, 72 (16), 1436–1440. <https://doi.org/10.1212/WNL.0b013e3181a26b30>.
- (31) Lane, D. J. R.; Ayton, S.; Bush, A. I. Iron and Alzheimer's Disease: An Update on Emerging Mechanisms. *J. Alzheimer's Dis.* **2018**, 64 (s1), S379–S395. <https://doi.org/10.3233/JAD-179944>.
- (32) Zecca, L.; Youdim, M. B. H.; Riederer, P.; Connor, J. R.; Crichton, R. R. Iron, Brain Ageing and Neurodegenerative Disorders. *Nat. Rev. Neurosci.* **2004**, 5 (11), 863–873. <https://doi.org/10.1038/nrn1537>.
- (33) Apostolakis, S.; Kypraiou, A. M. Iron in Neurodegenerative Disorders: Being in the Wrong Place at the Wrong Time? *Rev. Neurosci.* **2017**, 28 (8), 893–911. <https://doi.org/10.1515/revneuro-2017-0020>.
- (34) Raimundo, N.; Song, L.; Shutt, T. E.; McKay, S. E.; Cotney, J.; Guan, M. X.; Gilliland, T. C.; Hohuan, D.; Santos-Sacchi, J.; Shadel, G. S. Mitochondrial Stress Engages E2F1 Apoptotic Signaling to Cause Deafness. *Cell* **2012**, 148 (4), 716–726. <https://doi.org/10.1016/j.cell.2011.12.027>.
- (35) Boddaert, N.; Sang, K. H. L. Q.; Rötig, A.; Leroy-Willig, A.; Gallet, S.; Brunelle, F.; Sidi, D.; Thalabard, J. C.; Munnich, A.; Cabantchik, Z. I. Selective Iron Chelation in Friedreich Ataxia: Biologic and Clinical Implications. *Blood* **2007**, 110 (1), 401–408. <https://doi.org/10.1182/blood-2006-12-065433>.
- (36) Hocq, A.; Brouette, N.; Saussez, S.; Luhmer, M.; Gillis, P.; Gossuin, Y. Variable-Field Relaxometry of Iron-Containing Human Tissues: A Preliminary Study. *Contrast Media Mol. Imaging* **2009**, 4 (4), 157–164. <https://doi.org/10.1002/cmimi.275>.
- (37) McLachlan, D. R. C.; Kruck, T. P. A.; Kalow, W.; Andrews, D. F.; Dalton, A. J.; Bell, M. Y.; Smith, W. L. Intramuscular Desferrioxamine in Patients with Alzheimer's Disease. *Lancet* **1991**, 337 (8753), 1304–1308. [https://doi.org/10.1016/0140-6736\(91\)92978-B](https://doi.org/10.1016/0140-6736(91)92978-B).
- (38) Crielaard, B. J.; Lammers, T.; Rivella, S. Targeting Iron Metabolism in Drug Discovery and Delivery. *Nat. Rev. Drug Discov.* **2017**, 16 (6), 400–423. <https://doi.org/10.1038/nrd.2016.248>.
- (39) Sripetchwandee, J.; Wongjaikam, S.; Krintratun, W.; Chattipakorn, N.; Chattipakorn, S. C. A Combination of an Iron Chelator with an Antioxidant Effectively Diminishes the Dendritic Loss, Tau-Hyperphosphorylation, Amyloids- $\beta$  Accumulation and Brain Mitochondrial Dynamic Disruption in Rats with Chronic Iron-Overload. *Neuroscience* **2016**, 332, 191–202. <https://doi.org/10.1016/j.neuroscience.2016.07.003>.
- (40) Nazem, A.; Mansoori, G. A. Nanotechnology Solutions for Alzheimer's Disease: Advances in Research Tools, Diagnostic Methods and Therapeutic Agents. *J. Alzheimer's Dis.* **2008**, 13 (2), 199–223. <https://doi.org/10.3233/JAD-2008-13210>.
- (41) Wong, A. D.; Ye, M.; Levy, A. F.; Rothstein, J. D.; Bergles, D. E.; Searson, P. C. The Blood-Brain Barrier: An Engineering Perspective. *Front. Neuroeng.* **2013**, 6 (JUL). <https://doi.org/10.3389/fneng.2013.00007>.
- (42) Martinho, N.; Damgé, C.; Reis, C. P. Recent Advances in Drug Delivery Systems. *J. Biomater. Nanobiotechnol.* **2011**, 02 (05), 510–526. <https://doi.org/10.4236/jbnb.2011.225062>.

- (43) Pardridge, W. M. Molecular Biology of the Blood-Brain Barrier. *Mol. Biotechnol.* **2005**, *30* (1), 57–69. <https://doi.org/10.1385/mb:30:1:057>.
- (44) Shakeri, S.; Ashrafizadeh, M.; Zarrabi, A.; Roghanian, R.; Afshar, E. G.; Pardakhty, A.; Mohammadinejad, R.; Kumar, A.; Thakur, V. K. Multifunctional Polymeric Nanoplatfoms for Brain Diseases Diagnosis, Therapy and Theranostics. *Biomedicines* **2020**, *8* (1). <https://doi.org/10.3390/biomedicines8010013>.
- (45) Saeedi, M.; Eslamifar, M.; Khezri, K.; Dizaj, S. M. Applications of Nanotechnology in Drug Delivery to the Central Nervous System. *Biomed. Pharmacother.* **2019**, *111*, 666–675. <https://doi.org/10.1016/j.biopha.2018.12.133>.
- (46) Senior, J. H. Nanoparticulate Drug Delivery Systems. *Drug Dev. Ind. Pharm.* **2008**, *34* (1), 116–116. <https://doi.org/10.1080/03639040701877119>.
- (47) Garbayo, E.; Mendoza, A.; Blanco-Prieto, M. Diagnostic and Therapeutic Uses of Nanomaterials in the Brain. *Curr. Med. Chem.* **2014**, *21* (36), 4100–4131. <https://doi.org/10.2174/0929867321666140815124246>.
- (48) Saraiva, C.; Praça, C.; Ferreira, R.; Santos, T.; Ferreira, L.; Bernardino, L. Nanoparticle-Mediated Brain Drug Delivery: Overcoming Blood-Brain Barrier to Treat Neurodegenerative Diseases. *J. Control. Release* **2016**, *235*, 34–47. <https://doi.org/10.1016/j.jconrel.2016.05.044>.
- (49) Olivier, J. C. Drug Transport to Brain with Targeted Nanoparticles. *NeuroRx* **2005**, *2* (1), 108–119. <https://doi.org/10.1602/neurorx.2.1.108>.
- (50) Wohlfart, S.; Gelperina, S.; Kreuter, J. Transport of Drugs across the Blood-Brain Barrier by Nanoparticles. *J. Control. Release* **2012**, *161* (2), 264–273. <https://doi.org/10.1016/j.jconrel.2011.08.017>.
- (51) Xue, X. *Nanomedicine in Brain Diseases*; 2019. <https://doi.org/10.1007/978-981-13-8731-9>.
- (52) Naqvi, S.; Panghal, A.; Flora, S. J. S. Nanotechnology: A Promising Approach for Delivery of Neuroprotective Drugs. *Front. Neurosci.* **2020**, *14* (June), 1–26. <https://doi.org/10.3389/fnins.2020.00494>.
- (53) Shubayev, V. I.; Pisanic, T. R.; Jin, S. Magnetic Nanoparticles for Theragnostics. *Adv. Drug Deliv. Rev.* **2009**, *61* (6), 467–477. <https://doi.org/10.1016/j.addr.2009.03.007>.
- (54) Zhang, L.; Gu, F. X.; Chan, J. M.; Wang, A. Z.; Langer, R. S.; Farokhzad, O. C. Nanoparticles in Medicine: Therapeutic Applications and Developments. *Clin. Pharmacol. Ther.* **2008**, *83* (5), 761–769. <https://doi.org/10.1038/sj.clpt.6100400>.
- (55) Mura, S.; Nicolas, J.; Couvreur, P. Stimuli-Responsive Nanocarriers for Drug Delivery. *Nat. Mater.* **2013**, *12* (11), 991–1003. <https://doi.org/10.1038/nmat3776>.
- (56) Kudr, J.; Haddad, Y.; Richtera, L.; Heger, Z.; Cernak, M.; Adam, V.; Zitka, O. Magnetic Nanoparticles: From Design and Synthesis to Real World Applications. *Nanomaterials* **2017**. <https://doi.org/10.3390/nano7090243>.
- (57) Wu, W.; He, Q.; Jiang, C. Magnetic Iron Oxide Nanoparticles: Synthesis and Surface

- Functionalization Strategies. *Nanoscale Res. Lett.* **2008**, *3* (11), 397–415. <https://doi.org/10.1007/s11671-008-9174-9>.
- (58) Majidi, S.; Sehrig, F. Z.; Farkhani, S. M.; Goloujeh, M. S.; Akbarzadeh, A. Current Methods for Synthesis of Magnetic Nanoparticles. *Artif. Cells, Nanomedicine Biotechnol.* **2016**, *44* (2), 722–734. <https://doi.org/10.3109/21691401.2014.982802>.
- (59) Michailidi, E. D.; Bomis, G.; Varoutoglou, A.; Efthimiadou, E. K.; Mitropoulos, A. C.; Favvas, E. P. Fundamentals and Applications of Nanobubbles. *Interface Sci. Technol.* **2019**, *30*, 69–99. <https://doi.org/10.1016/B978-0-12-814178-6.00004-2>.
- (60) Cavalli, R.; Argenziano, M.; Vigna, E.; Giustetto, P.; Torres, E.; Aime, S.; Terreno, E. Preparation and in Vitro Characterization of Chitosan Nanobubbles as Theranostic Agents. *Colloids Surfaces B Biointerfaces* **2015**, *129*, 39–46. <https://doi.org/10.1016/j.colsurfb.2015.03.023>.
- (61) Endo-Takahashi, Y.; Negishi, Y. Microbubbles and Nanobubbles with Ultrasound for Systemic Gene Delivery. *Pharmaceutics* **2020**, *12* (10), 1–14. <https://doi.org/10.3390/pharmaceutics12100964>.
- (62) Ficiarà, E.; Ansari, S. A.; Argenziano, M.; Cangemi, L.; Monge, C.; Cavalli, R.; D'Agata, F. Beyond Oncological Hyperthermia: Physically Drivable Magnetic Nanobubbles as Novel multipurpose Theranostic Carriers in the Central Nervous System. *Molecules* **2020**, *25* (9), 2104. <https://doi.org/10.3390/molecules25092104>.
- (63) Gehrke, I.; Geiser, A.; Somborn-Schulz, A. Innovations in Nanotechnology for Water Treatment. *Nanotechnol. Sci. Appl.* **2015**, *8*, 1. <https://doi.org/10.2147/NSA.S43773>.
- (64) Kadajji, V. G.; Betageri, G. V. Water Soluble Polymers for Pharmaceutical Applications. *Polym. 2011, Vol. 3, Pages 1972-2009* **2011**, *3* (4), 1972–2009. <https://doi.org/10.3390/POLYM3041972>.
- (65) Kurita, K. Chitin and Chitosan: Functional Biopolymers from Marine Crustaceans. *Mar. Biotechnol.* **2006**, *8* (3), 203–226. <https://doi.org/10.1007/s10126-005-0097-5>.
- (66) Badawy, M. E. I.; Rabea, E. I. A Biopolymer Chitosan and Its Derivatives as Promising Antimicrobial Agents against Plant Pathogens and Their Applications in Crop Protection. *Int. J. Carbohydr. Chem.* **2011**, *2011*, 1–29. <https://doi.org/10.1155/2011/460381>.
- (67) Dodane, V.; Vilivalam, V. D. Pharmaceutical Applications of Chitosan. *Pharm. Sci. Technol. Today* **1998**, *1* (6), 246–253. [https://doi.org/10.1016/S1461-5347\(98\)00059-5](https://doi.org/10.1016/S1461-5347(98)00059-5).
- (68) Maestrelli, F.; Zerrouk, N.; Chemtob, C.; Mura, P. Influence of Chitosan and Its Glutamate and Hydrochloride Salts on Naproxen Dissolution Rate and Permeation across Caco-2 Cells. *Int. J. Pharm.* **2004**, *271* (1–2), 257–267. <https://doi.org/10.1016/j.ijpharm.2003.11.024>.
- (69) Prabakaran, M.; Rodriguez-Perez, M. A.; De Saja, J. A.; Mano, J. F. Preparation and Characterization of Poly(L-Lactic Acid)-Chitosan Hybrid Scaffolds with Drug Release Capability. *J. Biomed. Mater. Res. - Part B Appl. Biomater.* **2007**, *81* (2), 427–434. <https://doi.org/10.1002/jbm.b.30680>.

- (70) Janes, K. A.; Fresneau, M. P.; Marazuela, A.; Fabra, A.; Alonso, M. J. Chitosan Nanoparticles as Delivery Systems for Doxorubicin. *J. Control. Release* **2001**, *73* (2–3), 255–267. [https://doi.org/10.1016/S0168-3659\(01\)00294-2](https://doi.org/10.1016/S0168-3659(01)00294-2).
- (71) Kyzas, G. Z.; Bikiaris, D. N. Recent Modifications of Chitosan for Adsorption Applications: A Critical and Systematic Review. *Mar. Drugs* **2015**, *13* (1), 312–337. <https://doi.org/10.3390/md13010312>.
- (72) NM, A.; JF, M. Chitosan Derivatives Obtained by Chemical Modifications for Biomedical and Environmental Applications. *Int. J. Biol. Macromol.* **2008**, *43* (5), 401–414. <https://doi.org/10.1016/J.IJBIOMAC.2008.09.007>.
- (73) Bhatnagar, A.; Sillanpää, M. Applications of Chitin- and Chitosan-Derivatives for the Detoxification of Water and Wastewater - A Short Review. *Adv. Colloid Interface Sci.* **2009**, *152* (1–2), 26–38. <https://doi.org/10.1016/j.cis.2009.09.003>.
- (74) Bayat, A.; Sadeghi, A. M. M.; Avadi, M. R.; Amini, M.; Rafiee-Tehrani, M.; Shafiee, A.; Majlesi, R.; Junginger, H. E. Synthesis of N,N-Dimethyl N-Ethyl Chitosan as a Carrier for Oral Delivery of Peptide Drugs. *J. Bioact. Compat. Polym.* **2006**, *21* (5), 433–444. <https://doi.org/10.1177/0883911506068679>.
- (75) Heinze, T.; Liebert, T.; Heublein, B.; Hornig, S. Functional Polymers Based on Dextran. *Adv. Polym. Sci.* **2006**, *205* (1), 199–291. [https://doi.org/10.1007/12\\_100](https://doi.org/10.1007/12_100).
- (76) Tears Naturelle Single Dose Eye Drops - Summary of Product Characteristics (SmPC) - (emc) <https://www.medicines.org.uk/emc/product/6295/smpc#gref> (accessed Sep 20, 2021).
- (77) Ogilvie, M. B.; Harvey, J. D. The Biographical Dictionary of Women in Science: Pioneering Lives from Ancient Times to the Mid-20th Century. *Choice Rev. Online* **2001**, *38* (06), 38-3076-38–3076. <https://doi.org/10.5860/choice.38-3076>.
- (78) McNamara, K.; Tofail, S. A. M. Nanosystems: The Use of Nanoalloys, Metallic, Bimetallic, and Magnetic Nanoparticles in Biomedical Applications. *Physical Chemistry Chemical Physics*. 2015. <https://doi.org/10.1039/c5cp00831j>.
- (79) Cardoso, V. F.; Francesko, A.; Ribeiro, C.; Bañobre-López, M.; Martins, P.; Lanceros-Mendez, S. Advances in Magnetic Nanoparticles for Biomedical Applications. **2017**, *7* (5), 1700845. <https://doi.org/10.1002/adhm.201700845>.
- (80) Khanna, L.; Verma, N. K.; Tripathi, S. K. Burgeoning Tool of Biomedical Applications - Superparamagnetic Nanoparticles. *Journal of Alloys and Compounds*. 2018. <https://doi.org/10.1016/j.jallcom.2018.04.093>.
- (81) Xie, W.; Guo, Z.; Gao, F.; Gao, Q.; Wang, D.; Liaw, B. S.; Cai, Q.; Sun, X.; Wang, X.; Zhao, L. Shape-, Size-and Structure-Controlled Synthesis and Biocompatibility of Iron Oxide Nanoparticles for Magnetic Theranostics. *Theranostics* **2018**, *8* (12), 3284–3307. <https://doi.org/10.7150/thno.25220>.
- (82) Mahoney, R. Intellectual Property and Public Health. **2006**, *84* (5), 340. <https://doi.org/10.2471/blt.06.031989>.
- (83) D'Agata, F.; Ruffinatti, F.; Boschi, S.; Stura, I.; Rainero, I.; Abollino, O.; Cavalli, R.; Guiot,

- C. Magnetic Nanoparticles in the Central Nervous System: Targeting Principles, Applications and Safety Issues. **2017**, 23 (1), 9. <https://doi.org/10.3390/molecules23010009>.
- (84) Sintov, A. C.; Velasco-Aguirre, C.; Gallardo-Toledo, E.; Araya, E.; Kogan, M. J. Metal Nanoparticles as Targeted Carriers Circumventing the Blood-Brain Barrier; Elsevier, 2016; pp 199–227. <https://doi.org/10.1016/bs.irn.2016.06.007>.
- (85) Majidi, S.; Sehrig, F. Z.; Farkhani, S. M.; Goloujeh, M. S.; Akbarzadeh, A. Current Methods for Synthesis of Magnetic Nanoparticles. **2014**, 44 (2), 722–734. <https://doi.org/10.3109/21691401.2014.982802>.
- (86) Sharma, H. S.; Menon, P. K.; Lafuente, J. V.; Aguilar, Z. P.; Wang, Y. A.; Muresanu, D. F.; Mössler, H.; Patnaik, R.; Sharma, A. The Role of Functionalized Magnetic Iron Oxide Nanoparticles in the Central Nervous System Injury and Repair: New Potentials for Neuroprotection with Cerebrolysin Therapy. *J. Nanosci. Nanotechnol.* **2014**, 14 (1), 577–595. <https://doi.org/10.1166/jnn.2014.9213>.
- (87) Ajdary, M.; Moosavi, M.; Rahmati, M.; Falahati, M.; Mahboubi, M.; Mandegary, A.; Jangjoo, S.; Mohammadinejad, R.; Varma, R. Health Concerns of Various Nanoparticles: A Review of Their in Vitro and in Vivo Toxicity. **2018**, 8 (9), 634. <https://doi.org/10.3390/nano8090634>.
- (88) N, Z.; H, J.; P, Y.; J, N.; MU, F.; MW, A.; IO, U.; H, L.; X, N. Surface Modification of Magnetic Iron Oxide Nanoparticles. *Nanomater. (Basel, Switzerland)* **2018**, 8 (10). <https://doi.org/10.3390/NANO8100810>.
- (89) Shubayev, V. I.; Pisanic, T. R.; Jin, S. Magnetic Nanoparticles for Theragnostics. *Adv. Drug Deliv. Rev.* **2009**, 61 (6), 467–477. <https://doi.org/10.1016/j.addr.2009.03.007>.
- (90) Ali, A.; Zafar, H.; Zia, M.; ul Haq, I.; Phull, A. R.; Ali, J. S.; Hussain, A. Synthesis, Characterization, Applications, and Challenges of Iron Oxide Nanoparticles. *Nanotechnol. Sci. Appl.* **2016**, 9, 49–67. <https://doi.org/10.2147/NSA.S99986>.
- (91) Rasheed, R.; Meera, V. Synthesis of Iron Oxide Nanoparticles Coated Sand by Biological Method and Chemical Method. **2016**, 24, 210–216. <https://doi.org/10.1016/j.protcy.2016.05.029>.
- (92) Osial, M.; Rybicka, P.; Pękała, M.; Cichowicz, G.; Cyrański, M.; Krysiński, P. Easy Synthesis and Characterization of Holmium-Doped SPIONs. *Nanomaterials* **2018**, 8 (6), 430. <https://doi.org/10.3390/nano8060430>.
- (93) Bhandari, R.; Gupta, P.; Dziubla, T.; Hilt, J. Z. Single Step Synthesis, Characterization and Applications of Curcumin Functionalized Iron Oxide Magnetic Nanoparticles. **2016**, 67, 59–64. <https://doi.org/10.1016/j.msec.2016.04.093>.
- (94) Gruskiene, R.; Krivorotova, T.; Staneviciene, R.; Ratautas, D.; Serviene, E.; Sereikaite, J. Preparation and Characterization of Iron Oxide Magnetic Nanoparticles Functionalized by Nisin. *Colloids Surfaces B Biointerfaces* **2018**, 169, 126–134. <https://doi.org/10.1016/j.colsurfb.2018.05.017>.
- (95) Lassoued, A.; Dkhil, B.; Gadri, A.; Ammar, S. Control of the Shape and Size of Iron Oxide ( $\alpha$ -Fe<sub>2</sub>O<sub>3</sub>) Nanoparticles Synthesized through the Chemical Precipitation Method.

- Results Phys.* **2017**, *7*, 3007–3015. <https://doi.org/10.1016/J.RINP.2017.07.066>.
- (96) Fatima, H.; Kim, K.-S. Iron-Based Magnetic Nanoparticles for Magnetic Resonance Imaging. **2018**, *29* (11), 2678–2685. <https://doi.org/10.1016/j.appt.2018.07.017>.
- (97) Belaïd, S.; Stanicki, D.; Elst, L. Vander; Muller, R. N.; Laurent, S. Influence of Experimental Parameters on Iron Oxide Nanoparticle Properties Synthesized by Thermal Decomposition: Size and Nuclear Magnetic Resonance Studies. **2018**, *29* (16), 165603. <https://doi.org/10.1088/1361-6528/aaae59>.
- (98) Frey, N. A.; Peng, S.; Cheng, K.; Sun, S. Magnetic Nanoparticles: Synthesis, Functionalization, and Applications in Bioimaging and Magnetic Energy Storage. **2009**, *38* (9), 2532. <https://doi.org/10.1039/b815548h>.
- (99) Glasgow, W.; Fellows, B.; Qi, B.; Darroudi, T.; Kitchens, C.; Ye, L.; Crawford, T. M.; Mefford, O. T. Continuous Synthesis of Iron Oxide (Fe<sub>3</sub>O<sub>4</sub>) Nanoparticles via Thermal Decomposition. **2016**, *26*, 47–53. <https://doi.org/10.1016/j.jpartic.2015.09.011>.
- (100) Effenberger, F. B.; Couto, R. A.; Kiyohara, P. K.; Machado, G.; Masunaga, S. H.; Jardim, R. F.; Rossi, L. M. Economically Attractive Route for the Preparation of High Quality Magnetic Nanoparticles by the Thermal Decomposition of Iron(III) Acetylacetonate. **2017**, *28* (11), 115603. <https://doi.org/10.1088/1361-6528/aa5ab0>.
- (101) Orsini, N. J.; Babić-Stojić, B.; Spasojević, V.; Calatayud, M. P.; Cvjetičanin, N.; Goya, G. F. Magnetic and Power Absorption Measurements on Iron Oxide Nanoparticles Synthesized by Thermal Decomposition of Fe(Acac)<sub>3</sub>. **2018**, *449*, 286–296. <https://doi.org/10.1016/j.jmmm.2017.10.053>.
- (102) Grüttner, C.; Müller, K.; Teller, J.; Westphal, F. Synthesis and Functionalisation of Magnetic Nanoparticles for Hyperthermia Applications. **2013**, *29* (8), 777–789. <https://doi.org/10.3109/02656736.2013.835876>.
- (103) Kekalo, K.; Koo, K.; Zeitchick, E.; Baker, I. Microemulsion Synthesis of Iron Core/Iron Oxide Shell Magnetic Nanoparticles and Their Physicochemical Properties. **2012**, *1416*. <https://doi.org/10.1557/opl.2012.736>.
- (104) López, R.; Pineda, M.; Hurtado, G.; León, R.; Fernández, S.; Saade, H.; Bueno, D. Chitosan-Coated Magnetic Nanoparticles Prepared in One Step by Reverse Microemulsion Precipitation. **2013**, *14* (10), 19636–19650. <https://doi.org/10.3390/ijms141019636>.
- (105) Lu, A.-H.; Salabas, E. L.; Schüth, F. Magnetic Nanoparticles: Synthesis, Protection, Functionalization, and Application. *Angew. Chemie Int. Ed.* **2007**, *46* (8), 1222–1244. <https://doi.org/10.1002/ANIE.200602866>.
- (106) Wang, Y.; Yang, C.-X.; Yan, X.-P. Hydrothermal and Biomineralization Synthesis of a Dual-Modal Nanoprobe for Targeted near-Infrared Persistent Luminescence and Magnetic Resonance Imaging. **2017**, *9* (26), 9049–9055. <https://doi.org/10.1039/c7nr02038d>.
- (107) Nejati, K.; Zabihi, R. Preparation and Magnetic Properties of Nano Size Nickel Ferrite Particles Using Hydrothermal Method. *Chem. Cent. J.* **2012**, *6* (1), 394. <https://doi.org/10.1186/1752-153X-6-23>.

- (108) Lassoued, A.; Lassoued, M. S.; Dkhil, B.; Ammar, S.; Gadri, A. Synthesis, Photoluminescence and Magnetic Properties of Iron Oxide ( $\alpha$ -Fe<sub>2</sub>O<sub>3</sub>) Nanoparticles through Precipitation or Hydrothermal Methods. **2018**, *101*, 212–219. <https://doi.org/10.1016/j.physe.2018.04.009>.
- (109) Hemery, G.; Keyes, A. C.; Garaio, E.; Rodrigo, I.; Garcia, J. A.; Plazaola, F.; Garanger, E.; Sandre, O. Tuning Sizes, Morphologies, and Magnetic Properties of Monocore Versus Multicore Iron Oxide Nanoparticles through the Controlled Addition of Water in the Polyol Synthesis. **2017**, *56* (14), 8232–8243. <https://doi.org/10.1021/acs.inorgchem.7b00956>.
- (110) Hasany, S. F.; Ahmed, I.; J, R.; Rehman, A. Systematic Review of the Preparation Techniques of Iron Oxide Magnetic Nanoparticles. **2013**, *2* (6), 148–158. <https://doi.org/10.5923/j.nn.20120206.01>.
- (111) Hurley, K. R.; Ring, H. L.; Kang, H.; Klein, N. D.; Haynes, C. L. Characterization of Magnetic Nanoparticles in Biological Matrices. **2015**, *87* (23), 11611–11619. <https://doi.org/10.1021/acs.analchem.5b02229>.
- (112) Gopal, S. V.; Mini, R.; Jothy, V. B.; Joe, I. H. Synthesis and Characterization of Iron Oxide Nanoparticles Using {DMSO} as a Stabilizer. **2015**, *2* (3), 1051–1055. <https://doi.org/10.1016/j.matpr.2015.06.036>.
- (113) Babić-Stojić, B.; Jokanović, V.; Milivojević, D.; Požek, M.; Jagličić, Z.; Makovec, D.; Orsini, N. J.; Marković, M.; Arsin, K.; Paunović, V. Ultrasmall Iron Oxide Nanoparticles: Magnetic and {NMR} Relaxometric Properties. **2018**, *18* (2), 141–149. <https://doi.org/10.1016/j.cap.2017.11.017>.
- (114) Das, B.; Kusz, J.; Reddy, V. R.; Zubko, M.; Bhattacharjee, A. Solventless Synthesis, Morphology, Structure and Magnetic Properties of Iron Oxide Nanoparticles. **2017**, *74*, 62–69. <https://doi.org/10.1016/j.solidstatesciences.2017.10.010>.
- (115) Lim, J.; Yeap, S. P.; Che, H. X.; Low, S. C. Characterization of Magnetic Nanoparticle by Dynamic Light Scattering. **2013**, *8* (1). <https://doi.org/10.1186/1556-276x-8-381>.
- (116) Bona, K. R. Di; Xu, Y.; Ramirez, P. A.; DeLaine, J.; Parker, C.; Bao, Y.; Rasco, J. F. Surface Charge and Dosage Dependent Potential Developmental Toxicity and Biodistribution of Iron Oxide Nanoparticles in Pregnant {CD}-1 Mice. **2014**, *50*, 36–42. <https://doi.org/10.1016/j.reprotox.2014.09.010>.
- (117) Ghazanfari, M. R.; Kashefi, M.; Shams, S. F.; Jaafari, M. R. Perspective of Fe<sub>3</sub>O<sub>4</sub> Nanoparticles Role in Biomedical Applications. *Biochem. Res. Int.* **2016**, *2016*. <https://doi.org/10.1155/2016/7840161>.
- (118) Akbarzadeh, A.; Samiei, M.; Davaran, S. Magnetic Nanoparticles: Preparation, Physical Properties, and Applications in Biomedicine. *Nanoscale Res. Lett.* **2012**. <https://doi.org/10.1186/1556-276X-7-144>.
- (119) Muthiah, M.; Park, I.-K.; Cho, C.-S. Surface Modification of Iron Oxide Nanoparticles by Biocompatible Polymers for Tissue Imaging and Targeting. **2013**, *31* (8), 1224–1236. <https://doi.org/10.1016/j.biotechadv.2013.03.005>.
- (120) Sodipo, B. K.; Aziz, A. A. {ChemInform} Abstract: Recent Advances in Synthesis and

- Surface Modification of Superparamagnetic Iron Oxide Nanoparticles with Silica. **2016**, 47 (36). <https://doi.org/10.1002/chin.201636202>.
- (121) Sharma, K. S.; Ningthoujam, R. S.; Dubey, A. K.; Chattopadhyay, A.; Phapale, S.; Juluri, R. R.; Mukherjee, S.; Tewari, R.; Shetake, N. G.; Pandey, B. N.; Vatsa, R. K. Synthesis and Characterization of Monodispersed Water Dispersible Fe<sub>3</sub>O<sub>4</sub> Nanoparticles and in Vitro Studies on Human Breast Carcinoma Cell Line under Hyperthermia Condition. **2018**, 8 (1). <https://doi.org/10.1038/s41598-018-32934-w>.
- (122) Liu, Y.; Li, J.; Xu, K.; Gu, J.; Huang, L.; Zhang, L.; Liu, N.; Kong, J.; Xing, M.; Zhang, L.; Zhang, L. Characterization of Superparamagnetic Iron Oxide Nanoparticle-Induced Apoptosis in PC12 Cells and Mouse Hippocampus and Striatum. *Toxicol. Lett.* **2018**, 292, 151–161. <https://doi.org/10.1016/j.toxlet.2018.04.033>.
- (123) Jeevanandam, J.; Barhoum, A.; Chan, Y. S.; Dufresne, A.; Danquah, M. K. Review on Nanoparticles and Nanostructured Materials: History, Sources, Toxicity and Regulations. **2018**, 9, 1050–1074. <https://doi.org/10.3762/bjnano.9.98>.
- (124) Zullino, S.; Soster, M.; Khadjavi, A.; Gabriele, D.; Ciprian, R.; Albertini, F.; Cavalli, R.; Guiot, C. PO-1068: Characterization of Superparamagnetic, Oxygen Loaded NanoBubbles for Hyperthermia and Radiotherapy. *Radiother. Oncol.* **2015**, 115, S576. [https://doi.org/10.1016/s0167-8140\(15\)41060-6](https://doi.org/10.1016/s0167-8140(15)41060-6).
- (125) Wierzbinski, K. R.; Szymanski, T.; Rozwadowska, N.; Rybka, J. D.; Zimna, A.; Zalewski, T.; Nowicka-Bauer, K.; Malcher, A.; Nowaczyk, M.; Krupinski, M.; Fiedorowicz, M.; Bogorodzki, P.; Grieb, P.; Giersig, M.; Kurpisz, M. K. Potential Use of Superparamagnetic Iron Oxide Nanoparticles for in Vitro and in Vivo Bioimaging of Human Myoblasts. **2018**, 8 (1). <https://doi.org/10.1038/s41598-018-22018-0>.
- (126) Li, Q.; Tang, G.; Xue, S.; He, X.; Miao, P.; Li, Y.; Wang, J.; Xiong, L.; Wang, Y.; Zhang, C.; Yang, G.-Y. Silica-Coated Superparamagnetic Iron Oxide Nanoparticles Targeting Of~{EPCs} in Ischemic Brain Injury. **2013**, 34 (21), 4982–4992. <https://doi.org/10.1016/j.biomaterials.2013.03.030>.
- (127) Unterweger, H.; Dézsi, L.; Matuszak, J.; Janko, C.; Poettler, M.; Jordan, J.; Bäuerle, T.; Szebeni, J.; Fey, T.; Boccaccini, A.; Alexiou, C.; Cicha, I. Dextran-Coated Superparamagnetic Iron Oxide Nanoparticles for Magnetic Resonance Imaging: Evaluation of Size-Dependent Imaging Properties, Storage Stability and Safety. **2018**, Volume 13, 1899–1915. <https://doi.org/10.2147/ijn.s156528>.
- (128) Arias, L.; Pessan, J.; Vieira, A.; Lima, T.; Delbem, A.; Monteiro, D. Iron Oxide Nanoparticles for Biomedical Applications: A Perspective on Synthesis, Drugs, Antimicrobial Activity, and Toxicity. **2018**, 7 (2), 46. <https://doi.org/10.3390/antibiotics7020046>.
- (129) Ivask, A.; Pilkington, E. H.; Blin, T.; Käkinen, A.; Vija, H.; Visnapuu, M.; Quinn, J. F.; Whittaker, M. R.; Qiao, R.; Davis, T. P.; Ke, P. C.; Voelcker, N. H. Uptake and Transcytosis of Functionalized Superparamagnetic Iron Oxide Nanoparticles in an in Vitro Blood Brain Barrier Model. *Biomater. Sci.* **2018**, 6 (2), 314–323. <https://doi.org/10.1039/C7BM01012E>.
- (130) Falk, M. H.; Issels, R. D. Hyperthermia in Oncology. *Int. J. Hyperth.* **2001**, 17 (1), 1–18.



- <https://doi.org/10.1080/02656730150201552>.
- (131) Hildebrandt, B.; Wust, P.; Ahlers, O.; Dieing, A.; Sreenivasa, G.; Kerner, T.; Felix, R.; Riess, H. The Cellular and Molecular Basis of Hyperthermia. *Crit. Rev. Oncol. Hematol.* **2002**, *43* (1), 33–56. [https://doi.org/10.1016/S1040-8428\(01\)00179-2](https://doi.org/10.1016/S1040-8428(01)00179-2).
- (132) van der Zee, J. Heating the Patient: A Promising Approach? *Ann. Oncol.* **2002**, *13* (8), 1173–1184. <https://doi.org/10.1093/annonc/mdf280>.
- (133) Wust, P.; Hildebrandt, B.; Sreenivasa, G.; Rau, B.; Gellermann, J.; Riess, H.; Felix, R.; Schlag, P. Hyperthermia in Combined Treatment of Cancer. *Lancet Oncol.* **2002**, *3* (8), 487–497. [https://doi.org/10.1016/S1470-2045\(02\)00818-5](https://doi.org/10.1016/S1470-2045(02)00818-5).
- (134) Sapareto, S. A.; Dewey, W. C. Thermal Dose Determination in Cancer Therapy. *Int. J. Radiat. Oncol. Biol. Phys.* **1984**, *10* (6), 787–800. [https://doi.org/10.1016/0360-3016\(84\)90379-1](https://doi.org/10.1016/0360-3016(84)90379-1).
- (135) Dewhirst, M. W.; Sim, D. A. The Utility of Thermal Dose as a Predictor of Tumor and Normal Tissue Responses to Combined Radiation and Hyperthermia. *Cancer Res.* **1984**, *44* (10 SUPPL.), 4772–4781.
- (136) Kim, S. H.; Kim, J. H.; Hahn, E. W. The Enhanced Killing of Irradiated HeLa Cells in Synchronous Culture by Hyperthermia. *Radiat. Res.* **1976**, *66* (2), 337–345. <https://doi.org/10.2307/3574401>.
- (137) Gerweck, L. E. Modification of Cell Lethality at Elevated Temperatures. The PH Effect. *Radiat. Res.* **1977**, *70* (1), 224–235. <https://doi.org/10.2307/3574745>.
- (138) Gerweck, L. E.; Nygaard, T. G.; Burlett, M. Response of Cells to Hyperthermia under Acute and Chronic Hypoxic. *Cancer Res.* **1979**, *39* (3), 966–972.
- (139) Guiot, C.; Madon, E.; Allegro, D.; Piantà, P. G.; Baiotto, B.; Gabriele, P. Perfusion and Thermal Field during Hyperthermia. Experimental Measurements and Modelling in Recurrent Breast Cancer. *Phys. Med. Biol.* **1998**, *43* (10), 2831–2843. <https://doi.org/10.1088/0031-9155/43/10/012>.
- (140) Hildebrandt, B.; Wust, P.; Ahlers, O.; Dieing, A.; Sreenivasa, G.; Kerner, T.; Felix, R.; Riess, H. The Cellular and Molecular Basis of Hyperthermia. *Crit. Rev. Oncol. Hematol.* **2002**, *43* (1), 33–56. [https://doi.org/10.1016/S1040-8428\(01\)00179-2](https://doi.org/10.1016/S1040-8428(01)00179-2).
- (141) Spirou, S. V.; Basini, M.; Lascialfari, A.; Sangregorio, C.; Innocenti, C. Magnetic Hyperthermia and Radiation Therapy: Radiobiological Principles and Current Practice. *Nanomaterials* **2018**, *8* (6), 401. <https://doi.org/10.3390/nano8060401>.
- (142) Matsumine, A.; Takegami, K.; Asanuma, K.; Matsubara, T.; Nakamura, T.; Uchida, A.; Sudo, A. A Novel Hyperthermia Treatment for Bone Metastases Using Magnetic Materials. *Int. J. Clin. Oncol.* **2011**, *16* (2), 101–108. <https://doi.org/10.1007/s10147-011-0217-3>.
- (143) Maier-Hauff, K.; Rothe, R.; Scholz, R.; Gneveckow, U.; Wust, P.; Thiesen, B.; Feussner, A.; Deimling, A.; Waldoefner, N.; Felix, R.; Jordan, A. Intracranial Thermotherapy Using Magnetic Nanoparticles Combined with External Beam Radiotherapy: Results of a Feasibility Study on Patients with Glioblastoma Multiforme. *J. Neurooncol.* **2007**, *81* (1),

- 53–60. <https://doi.org/10.1007/s11060-006-9195-0>.
- (144) Ansari, S. A. M. K.; Ficiarà, E.; Ruffinatti, F. A.; Stura, I.; Argenziano, M.; Abollino, O.; Cavalli, R.; Guiot, C.; D'Agata, F. Magnetic Iron Oxide Nanoparticles: Synthesis, Characterization and Functionalization for Biomedical Applications in the Central Nervous System. *Materials (Basel)*. **2019**, *12* (3). <https://doi.org/10.3390/ma12030465>.
- (145) Song, W.; Luo, Y.; Zhao, Y.; Liu, X.; Zhao, J.; Luo, J.; Zhang, Q.; Ran, H.; Wang, Z.; Guo, D. Magnetic Nanobubbles with Potential for Targeted Drug Delivery and Trimodal Imaging in Breast Cancer: An in Vitro Study. *Nanomedicine* **2017**, *12* (9), 991–1009. <https://doi.org/10.2217/nnm-2017-0027>.
- (146) Hamarat Şanlıer, Ş.; Ak, G.; Yılmaz, H.; Ünal, A.; Bozkaya, Ü. F.; Taniyan, G.; Yıldırım, Y.; Yıldız Türkyılmaz, G. Development of Ultrasound-Triggered and Magnetic-Targeted Nanobubble System for Dual-Drug Delivery. *J. Pharm. Sci.* **2019**, *108* (3), 1272–1283. <https://doi.org/10.1016/J.XPHS.2018.10.030>.
- (147) Paulides, M. M.; Dobsicek Trefna, H.; Curto, S.; Rodrigues, D. B. Recent Technological Advancements in Radiofrequency- Andmicrowave-Mediated Hyperthermia for Enhancing Drug Delivery. *Adv. Drug Deliv. Rev.* **2020**, *163–164*, 3–18. <https://doi.org/10.1016/j.addr.2020.03.004>.
- (148) Cavalli, R.; Soster, M.; Argenziano, M. Nanobubbles: A Promising Efficient Tool for Therapeutic Delivery. *Ther. Deliv.* **2016**, *7* (2), 117–138. <https://doi.org/10.4155/tde.15.92>.
- (149) Cavalli, R.; Argenziano, M.; Vigna, E.; Giustetto, P.; Torres, E.; Aime, S.; Terreno, E. Preparation and in Vitro Characterization of Chitosan Nanobubbles as Theranostic Agents. *Colloids Surfaces B Biointerfaces* **2015**, *129*, 39–46. <https://doi.org/10.1016/j.colsurfb.2015.03.023>.
- (150) Cavalli, R.; Bisazza, A.; Giustetto, P.; Civra, A.; Lembo, D.; Trotta, G.; Guiot, C.; Trotta, M. Preparation and Characterization of Dextran Nanobubbles for Oxygen Delivery. *Int. J. Pharm.* **2009**, *381* (2), 160–165. <https://doi.org/10.1016/j.ijpharm.2009.07.010>.
- (151) Argenziano, M.; Banche, G.; Luganini, A.; Finesso, N.; Allizond, V.; Gulino, G. R.; Khadjavi, A.; Spagnolo, R.; Tullio, V.; Giribaldi, G.; Guiot, C.; Cuffini, A. M.; Prato, M.; Cavalli, R. Vancomycin-Loaded Nanobubbles: A New Platform for Controlled Antibiotic Delivery against Methicillin-Resistant Staphylococcus Aureus Infections. *Int. J. Pharm.* **2017**, *523* (1), 176–188. <https://doi.org/10.1016/j.ijpharm.2017.03.033>.
- (152) Kripfgans, O. D.; Fabiilli, M. L.; Carson, P. L.; Fowlkes, J. B. On the Acoustic Vaporization of Micrometer-Sized Droplets. *J. Acoust. Soc. Am.* **2004**, *116* (1), 272–281. <https://doi.org/10.1121/1.1755236>.
- (153) Guiot, C.; Madon, E.; Allegro, D.; Piantà, P. G.; Baiotto, B.; Gabriele, P. Perfusion and Thermal Field during Hyperthermia. Experimental Measurements and Modelling in Recurrent Breast Cancer. *Phys. Med. Biol.* **1998**, *43* (10), 2831–2843. <https://doi.org/10.1088/0031-9155/43/10/012>.
- (154) Huang, W. C.; Shen, M. Y.; Chen, H. H.; Lin, S. C.; Chiang, W. H.; Wu, P. H.; Chang, C. W.;

- Chiang, C. S.; Chiu, H. C. Monocytic Delivery of Therapeutic Oxygen Bubbles for Dual-Modality Treatment of Tumor Hypoxia. *J. Control. Release* **2015**, *220* (Pt B), 738–750. <https://doi.org/10.1016/j.jconrel.2015.09.016>.
- (155) Sheng, Y.; Beguin, E.; Nesbitt, H.; Kamila, S.; Owen, J.; Barnsley, L. C.; Callan, B.; O’Kane, C.; Nomikou, N.; Hamoudi, R.; Taylor, M. A.; Love, M.; Kelly, P.; O’Rourke, D.; Stride, E.; McHale, A. P.; Callan, J. F. Magnetically Responsive Microbubbles as Delivery Vehicles for Targeted Sonodynamic and Antimetabolite Therapy of Pancreatic Cancer. *J. Control. Release* **2017**, *262*, 192–200. <https://doi.org/10.1016/j.jconrel.2017.07.040>.
- (156) Umut, E.; Coşkun, M.; Pineider, F.; Berti, D.; Güngüneş, H. Nickel Ferrite Nanoparticles for Simultaneous Use in Magnetic Resonance Imaging and Magnetic Fluid Hyperthermia. *J. Colloid Interface Sci.* **2019**, *550*, 199–209. <https://doi.org/10.1016/j.jcis.2019.04.092>.
- (157) Sudame, A.; Kandasamy, G.; Maity, D. Single and Dual Surfactants Coated Hydrophilic Superparamagnetic Iron Oxide Nanoparticles for Magnetic Fluid Hyperthermia Applications. *J. Nanosci. Nanotechnol.* **2019**, *19* (7), 3991–3999. <https://doi.org/10.1166/jnn.2019.16326>.
- (158) Spirou, S. V.; Basini, M.; Lascialfari, A.; Sangregorio, C.; Innocenti, C. Magnetic Hyperthermia and Radiation Therapy: Radiobiological Principles and Current Practice. *Nanomaterials* **2018**, *8* (6). <https://doi.org/10.3390/nano8060401>.
- (159) Sohail, A.; Ahmad, Z.; Bégu, O. A.; Arshad, S.; Sherin, L. Revue Sur Le Traitement Par Hyperthermie Médicée Par Nanoparticules. *Bull. Cancer* **2017**, *104* (5), 452–461. <https://doi.org/10.1016/j.bulcan.2017.02.003>.
- (160) Chang, D.; Lim, M.; Goos, J. A. C. M.; Qiao, R.; Ng, Y. Y.; Mansfeld, F. M.; Jackson, M.; Davis, T. P.; Kavallaris, M. Biologically Targeted Magnetic Hyperthermia: Potential and Limitations. *Front. Pharmacol.* **2018**, *9* (AUG). <https://doi.org/10.3389/fphar.2018.00831>.
- (161) D’Agata, F.; Ruffinatti, F. A.; Boschi, S.; Stura, I.; Rainero, I.; Abollino, O.; Cavalli, R.; Guiot, C. Magnetic Nanoparticles in the Central Nervous System: Targeting Principles, Applications and Safety Issues. *Molecules* **2018**, *23* (1), 9. <https://doi.org/10.3390/molecules23010009>.
- (162) Zullino, S.; Argenziano, M.; Ansari, S.; Ciprian, R.; Nasi, L.; Albertini, F.; Cavalli, R.; Guiot, C. Superparamagnetic Oxygen-Loaded Nanobubbles to Enhance Tumor Oxygenation During Hyperthermia. *Front. Pharmacol.* **2019**, *0*, 1001. <https://doi.org/10.3389/FPHAR.2019.01001>.
- (163) Guiot, C.; Zullino, S.; Priano, L.; Cavalli, R. The Physics of Drug-Delivery across the Blood-Brain Barrier. *Ther. Deliv.* **2016**, *7* (3), 153–156. <https://doi.org/10.4155/tde-2016-0001>.
- (164) Huang, H.-Y.; Liu, H.-L.; Hsu, P.-H.; Chiang, C.-S.; Tsai, C.-H.; Chi, H.-S.; Chen, S.-Y.; Chen, Y.-Y. A Multitheragnostic Nanobubble System to Induce Blood–Brain Barrier Disruption with Magnetically Guided Focused Ultrasound. *Adv. Mater.* **2015**, *27* (4), 655–661. <https://doi.org/10.1002/ADMA.201403889>.

- (165) Sintov, A. C.; Velasco-Aguirre, C.; Gallardo-Toledo, E.; Araya, E.; Kogan, M. J. Metal Nanoparticles as Targeted Carriers Circumventing the Blood–Brain Barrier. *Int. Rev. Neurobiol.* **2016**, *130*, 199–227. <https://doi.org/10.1016/BS.IRN.2016.06.007>.
- (166) Tam, V. H.; Sosa, C.; Liu, R.; Yao, N.; Priestley, R. D. Nanomedicine as a Non-Invasive Strategy for Drug Delivery across the Blood Brain Barrier. *Int. J. Pharm.* **2016**, *515* (1–2), 331–342. <https://doi.org/10.1016/J.IJPHARM.2016.10.031>.
- (167) Yao, J.; Hsu, C.-H.; Li, Z.; Kim, T.; Hwang, L.-P.; Lin, Y.-C.; Lin, Y.-Y. Magnetic Resonance Nano-Theranostics for Glioblastoma Multiforme. *Curr. Pharm. Des.* **2015**, *21* (36), 5256–5266. <https://doi.org/10.2174/1381612821666150923103307>.
- (168) Mahmoudi, K.; Bouras, A.; Bozec, D.; Ivkov, R.; Hadjipanayis, C. Magnetic Hyperthermia Therapy for the Treatment of Glioblastoma: A Review of the Therapy’s History, Efficacy and Application in Humans. *Int. J. Hyperth.* **2018**, *34* (8), 1316–1328. <https://doi.org/10.1080/02656736.2018.1430867>.
- (169) Chertok, B.; David, A. E.; Yang, V. C. Brain Tumor Targeting of Magnetic Nanoparticles for Potential Drug Delivery: Effect of Administration Route and Magnetic Field Topography. *J. Control. Release* **2011**, *155* (3), 393–399. <https://doi.org/10.1016/j.jconrel.2011.06.033>.
- (170) Leterme, G.; Guigou, C.; Oudot, A.; Collin, B.; Boudon, J.; Millot, N.; Geissler, A.; Belharet, K.; Grayeli, A. B. Superparamagnetic Nanoparticle Delivery to the Cochlea Through Round Window by External Magnetic Field: Feasibility and Toxicity: <https://doi.org/10.1177/1553350619867217> **2019**, *26* (6), 646–655. <https://doi.org/10.1177/1553350619867217>.
- (171) Thomsen, L. B.; Thomsen, M. S.; Moos, T. Targeted Drug Delivery to the Brain Using Magnetic Nanoparticles. <http://dx.doi.org/10.4155/tde.15.56> **2015**, *6* (10), 1145–1155. <https://doi.org/10.4155/TDE.15.56>.
- (172) Roet, M.; Heschem, S. A.; Jahanshahi, A.; Rutten, B. P. F.; Anikeeva, P. O.; Temel, Y. Progress in Neuromodulation of the Brain: A Role for Magnetic Nanoparticles? *Prog. Neurobiol.* **2019**, *177*, 1–14. <https://doi.org/10.1016/j.pneurobio.2019.03.002>.
- (173) Khadjavi, A.; Stura, I.; Prato, M.; Minero, V. G.; Panariti, A.; Rivolta, I.; Gulino, G. R.; Bessone, F.; Giribaldi, G.; Quaglino, E.; Cavalli, R.; Cavallo, F.; Guiot, C. ‘In Vitro’, ‘In Vivo’ and ‘In Silico’ Investigation of the Anticancer Effectiveness of Oxygen-Loaded Chitosan-Shelled Nanodroplets as Potential Drug Vector. *Pharm. Res.* **2018**, *35* (4), 1–11. <https://doi.org/10.1007/S11095-018-2371-Z>.
- (174) Ansari, S. A. M. K.; Ficiarà, E.; Ruffinatti, F. A.; Stura, I.; Argenziano, M.; Abollino, O.; Cavalli, R.; Guiot, C.; D’Agata, F. Magnetic Iron Oxide Nanoparticles: Synthesis, Characterization and Functionalization for Biomedical Applications in the Central Nervous System. *Materials (Basel)*. **2019**, *12* (3), 465. <https://doi.org/10.3390/ma12030465>.
- (175) Jiang, Z.; Tian, Y.; Shan, D.; Wang, Y.; Gerhard, E.; Xia, J.; Huang, R.; He, Y.; Li, A.; Tang, J.; Ruan, H.; Li, Y.; Li, J.; Yang, J.; Wu, A. PH Protective Y 1 Receptor Ligand Functionalized Antiphagocytosis BPLP-WPU Micelles for Enhanced Tumor Imaging and Therapy with Prolonged Survival Time. *Biomaterials* **2018**, *170*, 70–81.

- <https://doi.org/10.1016/j.biomaterials.2018.04.002>.
- (176) Bramini, M.; Ye, D.; Hallerbach, A.; Nic Raghnaill, M.; Salvati, A.; Åberg, C.; Dawson, K. A. Imaging Approach to Mechanistic Study of Nanoparticle Interactions with the Blood-Brain Barrier. *ACS Nano* **2014**, *8* (5), 4304–4312. <https://doi.org/10.1021/nn5018523>.
- (177) Decuzzi, P.; Godin, B.; Tanaka, T.; Lee, S. Y.; Chiappini, C.; Liu, X.; Ferrari, M. Size and Shape Effects in the Biodistribution of Intravascularly Injected Particles. *J. Control. Release* **2010**, *141* (3), 320–327. <https://doi.org/10.1016/j.jconrel.2009.10.014>.
- (178) Saraiva, C.; Praça, C.; Ferreira, R.; Santos, T.; Ferreira, L.; Bernardino, L. Nanoparticle-Mediated Brain Drug Delivery: Overcoming Blood-Brain Barrier to Treat Neurodegenerative Diseases. *J. Control. Release* **2016**, *235*, 34–47. <https://doi.org/10.1016/j.jconrel.2016.05.044>.
- (179) Cavalli, R.; Soster, M.; Argenziano, M. Nanobubbles: A Promising Efficient Tool for Therapeutic Delivery. *Ther. Deliv.* **2016**, *7* (2), 117–138. <https://doi.org/10.4155/tde.15.92>.
- (180) Cavalli, R.; Bisazza, A.; Trotta, M.; Argenziano, M.; Civra, A.; Donalisio, M.; Lembo, D. New Chitosan Nanobubbles for Ultrasound-Mediated Gene Delivery: Preparation and in Vitro Characterization. *Int. J. Nanomedicine* **2012**, *7*, 3309–3318. <https://doi.org/10.2147/IJN.S30912>.
- (181) Cavalli, R.; Argenziano, M.; Vigna, E.; Giustetto, P.; Torres, E.; Aime, S.; Terreno, E. Preparation and in Vitro Characterization of Chitosan Nanobubbles as Theranostic Agents. *Colloids Surfaces B Biointerfaces* **2015**, *129*, 39–46. <https://doi.org/10.1016/j.colsurfb.2015.03.023>.
- (182) Argenziano, M.; Banche, G.; Luganini, A.; Finesso, N.; Allizond, V.; Gulino, G. R.; Khadjavi, A.; Spagnolo, R.; Tullio, V.; Giribaldi, G.; Guiot, C.; Cuffini, A. M.; Prato, M.; Cavalli, R. Vancomycin-Loaded Nanobubbles: A New Platform for Controlled Antibiotic Delivery against Methicillin-Resistant Staphylococcus Aureus Infections. *Int. J. Pharm.* **2017**, *523* (1), 176–188. <https://doi.org/10.1016/j.ijpharm.2017.03.033>.
- (183) Marano, F.; Frairia, R.; Rinella, L.; Argenziano, M.; Bussolati, B.; Grange, C.; Mastrocola, R.; Castellano, I.; Berta, L.; Cavalli, R.; Catalano, M. G. Combining Doxorubicin-Nanobubbles and Shockwaves for Anaplastic Thyroid Cancer Treatment: Preclinical Study in a Xenograft Mouse Model. *Endocr. Relat. Cancer* **2017**, *24* (6), 275–286. <https://doi.org/10.1530/ERC-17-0045>.
- (184) Marano, F.; Rinella, L.; Argenziano, M.; Cavalli, R.; Sassi, F.; D'Amelio, P.; Battaglia, A.; Gontero, P.; Bosco, O.; Peluso, R.; Fortunati, N.; Frairia, R.; Catalano, M. G. Targeting Taxanes to Castration-Resistant Prostate Cancer Cells by Nanobubbles and Extracorporeal Shock Waves. *PLoS One* **2016**, *11* (12), e0168553. <https://doi.org/10.1371/journal.pone.0168553>.
- (185) Marano, F.; Argenziano, M.; Frairia, R.; Adamini, A.; Bosco, O.; Rinella, L.; Fortunati, N.; Cavalli, R.; Catalano, M. G. Doxorubicin-Loaded Nanobubbles Combined with Extracorporeal Shock Waves: Basis for a New Drug Delivery Tool in Anaplastic Thyroid Cancer. *Thyroid* **2016**, *26* (5), 705–716. <https://doi.org/10.1089/thy.2015.0342>.

- (186) Dobrovolskaia, M. A.; Clogston, J. D.; Neun, B. W.; Hall, J. B.; Patri, A. K.; McNeil, S. E. Method for Analysis of Nanoparticle Hemolytic Properties in Vitro. *Nano Lett.* **2008**, *8* (8), 2180–2187. <https://doi.org/10.1021/nl0805615>.
- (187) Dobrovolskaia, M. A.; Aggarwal, P.; Hall, J. B.; McNeil, S. E. Preclinical Studies to Understand Nanoparticle Interaction with the Immune System and Its Potential Effects on Nanoparticle Biodistribution. *Mol. Pharm.* **2008**, *5* (4), 487–495. <https://doi.org/10.1021/mp800032f>.
- (188) Kripfgans, O. D.; Fabiilli, M. L.; Carson, P. L.; Fowlkes, J. B. On the Acoustic Vaporization of Micrometer-Sized Droplets. *J. Acoust. Soc. Am.* **2004**, *116* (1), 272–281. <https://doi.org/10.1121/1.1755236>.
- (189) Luo, B.; Zhang, H.; Liu, X.; Rao, R.; Wu, Y.; Liu, W. Novel DiR and SPIO Nanoparticles Embedded PEG-PLGA Nanobubbles as a Multimodal Imaging Contrast Agent. *Biomed. Mater. Eng.* **2015**, *26*, S911–S916. <https://doi.org/10.3233/BME-151384>.
- (190) Householder, K. T.; Dharmaraj, S.; Sandberg, D. I.; Wechsler-Reya, R. J.; Sirianni, R. W. Fate of Nanoparticles in the Central Nervous System after Intrathecal Injection in Healthy Mice. *Sci. Rep.* **2019**, *9* (1). <https://doi.org/10.1038/s41598-019-49028-w>.
- (191) Bottros, M. M.; Christo, P. J. Current Perspectives on Intrathecal Drug Delivery. *J. Pain Res.* **2014**, *7*, 615–626. <https://doi.org/10.2147/JPR.S37591>.
- (192) Datta, N. R.; Rogers, S.; Ordóñez, S. G.; Puric, E.; Bodis, S. Hyperthermia and Radiotherapy in the Management of Head and Neck Cancers: A Systematic Review and Meta-Analysis. *Int. J. Hyperth.* **2016**, *32* (1), 31–40. <https://doi.org/10.3109/02656736.2015.1099746>.
- (193) Gao, S.; Zheng, M.; Ren, X.; Tang, Y.; Liang, X. Local Hyperthermia in Head and Neck Cancer: Mechanism, Application and Advance. *Oncotarget* **2016**, *7* (35), 57367–57378. <https://doi.org/10.18632/oncotarget.10350>.
- (194) Lambert, A.; Schwarz, L.; Borbath, I.; Henry, A.; Van Laethem, J. L.; Malka, D.; Ducreux, M.; Conroy, T. An Update on Treatment Options for Pancreatic Adenocarcinoma. *Ther. Adv. Med. Oncol.* **2019**, *11*. <https://doi.org/10.1177/1758835919875568>.
- (195) Ferraris, C.; Cavalli, R.; Panciani, P. P.; Battaglia, L. Overcoming the Blood–Brain Barrier: Successes and Challenges in Developing Nanoparticle-Mediated Drug Delivery Systems for the Treatment of Brain Tumours. *Int. J. Nanomedicine* **2020**, *15*, 2999–3022. <https://doi.org/10.2147/IJN.S231479>.
- (196) Cerna, T.; Stiborova, M.; Adam, V.; Kizek, R.; Eckschlager, T. Nanocarrier Drugs in the Treatment of Brain Tumors. *J. Cancer Metastasis Treat.* **2016**, *2* (10), 407. <https://doi.org/10.20517/2394-4722.2015.95>.
- (197) Guiot, C.; Zullino, S.; Priano, L.; Cavalli, R. The Physics of Drug-Delivery across the Blood-Brain Barrier. *Ther. Deliv.* **2016**, *7* (3), 153–156. <https://doi.org/10.4155/tde-2016-0001>.
- (198) Van Liew, H. D.; Burkard, M. E. Relationship of Oxygen Content to PO<sub>2</sub> for Stabilized Bubbles in the Circulation: Theory. *J. Appl. Physiol.* **1996**, *81* (1), 500–508. <https://doi.org/10.1152/jappl.1996.81.1.500>.

- (199) Burkard, M. E.; Van Liew, H. D. Oxygen Transport to Tissue by Persistent Bubbles: Theory and Simulations. *J. Appl. Physiol.* **1994**, *77* (6), 2874–2878. <https://doi.org/10.1152/jappl.1994.77.6.2874>.
- (200) Zhao, J.; Liu, C. S.; Yuan, Y.; Tao, X. Y.; Shan, X. Q.; Sheng, Y.; Wu, F. Preparation of Hemoglobin-Loaded Nano-Sized Particles with Porous Structure as Oxygen Carriers. *Biomaterials* **2007**, *28* (7), 1414–1422. <https://doi.org/10.1016/j.biomaterials.2006.10.012>.
- (201) Porter, T.; Kricsfeld, D.; Cheatham, S.; Li, S. Effect of Blood and Microbubble Oxygen and Nitrogen Content on Perfluorocarbon-Filled Dextrose Albumin Microbubble Size and Efficacy: In Vitro and In Vivo Studies. *J. Am. Soc. Echocardiogr.* **1998**, *11* (5), 421–425. [https://doi.org/10.1016/S0894-7317\(98\)70020-3](https://doi.org/10.1016/S0894-7317(98)70020-3).
- (202) Unger, E. C.; Porter, T.; Culp, W.; Labell, R.; Matsunaga, T.; Zutshi, R. Therapeutic Applications of Lipid-Coated Microbubbles. *Adv. Drug Deliv. Rev.* **2004**, *56* (9), 1291–1314. <https://doi.org/10.1016/j.addr.2003.12.006>.
- (203) Unger, E. C.; Matsunaga, T. O.; McCreery, T.; Schumann, P.; Sweitzer, R.; Quigley, R. Therapeutic Applications of Microbubbles. *Eur. J. Radiol.* **2002**, *42* (2), 160–168. [https://doi.org/10.1016/S0720-048X\(01\)00455-7](https://doi.org/10.1016/S0720-048X(01)00455-7).
- (204) Wolfson, M. R.; Shaffer, T. H. Pulmonary Applications of Perfluorochemical Liquids: Ventilation and Beyond. *Paediatr. Respir. Rev.* **2005**, *6* (2), 117–127. <https://doi.org/10.1016/j.prrv.2005.03.010>.
- (205) Kong, S. D.; Lee, J.; Ramachandran, S.; Eliceiri, B. P.; Shubayev, V. I.; Lal, R.; Jin, S. Magnetic Targeting of Nanoparticles across the Intact Blood-Brain Barrier. *J. Control. Release* **2012**, *164* (1), 49–57. <https://doi.org/10.1016/j.jconrel.2012.09.021>.
- (206) Cedervall, T.; Lynch, I.; Lindman, S.; Berggård, T.; Thulin, E.; Nilsson, H.; Dawson, K. A.; Linse, S. Understanding the Nanoparticle-Protein Corona Using Methods to Quantify Exchange Rates and Affinities of Proteins for Nanoparticles. *Proc. Natl. Acad. Sci. U. S. A.* **2007**, *104* (7), 2050–2055. <https://doi.org/10.1073/pnas.0608582104>.
- (207) Pedziwiatr-Werbicka, E.; Horodecka, K.; Shcharbin, D.; Bryszewska, M. Nanoparticles in Combating Cancer: Opportunities and Limitations: A Brief Review. *Curr. Med. Chem.* **2020**, *28* (2), 346–359. <https://doi.org/10.2174/0929867327666200130101605>.
- (208) Zhang, T. T.; Li, W.; Meng, G.; Wang, P.; Liao, W. Strategies for Transporting Nanoparticles across the Blood-Brain Barrier. *Biomater. Sci.* **2016**, *4* (2), 219–229. <https://doi.org/10.1039/c5bm00383k>.
- (209) Home - Focused Ultrasound Foundation <https://www.fusfoundation.org/> (accessed Oct 7, 2021).
- (210) Yang, C.; Xiao, H.; Sun, Y.; Zhu, L.; Gao, Y.; Kwok, S.; Wang, Z.; Tang, Y. Lipid Microbubbles as Ultrasound-Stimulated Oxygen Carriers for Controllable Oxygen Release for Tumor Reoxygenation. *Ultrasound Med. Biol.* **2018**, *44* (2), 416–425. <https://doi.org/10.1016/j.ultrasmedbio.2017.08.1883>.
- (211) Estelrich, J.; Escribano, E.; Queralt, J.; Busquets, M. A. Iron Oxide Nanoparticles for Magnetically-Guided and Magnetically-Responsive Drug Delivery. *Int. J. Mol. Sci.* **2015**,

- 16 (4), 8070–8101. <https://doi.org/10.3390/ijms16048070>.
- (212) D'Agata, F.; Ruffinatti, F. A.; Boschi, S.; Stura, I.; Rainero, I.; Abollino, O.; Cavalli, R.; Guiot, C. Magnetic Nanoparticles in the Central Nervous System: Targeting Principles, Applications and Safety Issues. *Molecules* **2018**, *23* (1). <https://doi.org/10.3390/molecules23010009>.
- (213) Novoselova, M. V.; German, S. V.; Sineeveva, O. A.; Kulikov, O. A.; Minaeva, O. V.; Brodovskaya, E. P.; Ageev, V. P.; Zharkov, M. N.; Pyataev, N. A.; Sukhorukov, G. B.; Gorin, D. A. Submicron-Sized Nanocomposite Magnetic-Sensitive Carriers: Controllable Organ Distribution and Biological Effects. *Polymers (Basel)*. **2019**, *11* (6). <https://doi.org/10.3390/POLYM11061082>.
- (214) Owens, D. E.; Peppas, N. A. Opsonization, Biodistribution, and Pharmacokinetics of Polymeric Nanoparticles. *Int. J. Pharm.* **2006**, *307* (1), 93–102. <https://doi.org/10.1016/j.ijpharm.2005.10.010>.
- (215) Liu, X.; Zhang, Y.; Wang, Y.; Zhu, W.; Li, G.; Ma, X.; Zhang, Y.; Chen, S.; Tiwari, S.; Shi, K.; Zhang, S.; Fan, H. M.; Zhao, Y. X.; Liang, X. J. Comprehensive Understanding of Magnetic Hyperthermia for Improving Antitumor Therapeutic Efficacy. *Theranostics* **2020**, *10* (8), 3793–3815. <https://doi.org/10.7150/thno.40805>.
- (216) Cavalli, R.; Bisazza, A.; Giustetto, P.; Civra, A.; Lembo, D.; Trotta, G.; Guiot, C.; Trotta, M. Preparation and Characterization of Dextran Nanobubbles for Oxygen Delivery. *Int. J. Pharm.* **2009**, *381* (2), 160–165. <https://doi.org/10.1016/j.ijpharm.2009.07.010>.
- (217) Cavalli, R.; Bisazza, A.; Rolfo, A.; Balbis, S.; Madonnaripa, D.; Caniggia, I.; Guiot, C. Ultrasound-Mediated Oxygen Delivery from Chitosan Nanobubbles. *Int. J. Pharm.* **2009**, *378* (1–2), 215–217. <https://doi.org/10.1016/j.ijpharm.2009.05.058>.
- (218) Prato, M.; Magnetto, C.; Jose, J.; Khadjavi, A.; Cavallo, F.; Quaglino, E.; Panariti, A.; Rivolta, I.; Benintende, E.; Varetto, G.; Argenziano, M.; Troia, A.; Cavalli, R.; Guiot, C. 2H,3H-Decafluoropentane-Based Nanodroplets: New Perspectives for Oxygen Delivery to Hypoxic Cutaneous Tissues. *PLoS One* **2015**, *10* (3), e0119769. <https://doi.org/10.1371/journal.pone.0119769>.
- (219) Khadjavi, A.; Stura, I.; Prato, M.; Minero, V. G.; Panariti, A.; Rivolta, I.; Gulino, G. R.; Bessone, F.; Giribaldi, G.; Quaglino, E.; Cavalli, R.; Cavallo, F.; Guiot, C. 'In Vitro', 'In Vivo' and 'In Silico' Investigation of the Anticancer Effectiveness of Oxygen-Loaded Chitosan-Shelled Nanodroplets as Potential Drug Vector. *Pharm. Res.* **2018**, *35* (4), 1–11. <https://doi.org/10.1007/s11095-018-2371-z>.
- (220) Bessone, F.; Argenziano, M.; Grillo, G.; Ferrara, B.; Pizzimenti, S.; Barrera, G.; Cravotto, G.; Guiot, C.; Stura, I.; Cavalli, R.; Dianzani, C. Low-Dose Curcuminoid-Loaded in Dextran Nanobubbles Can Prevent Metastatic Spreading in Prostate Cancer Cells. *Nanotechnology* **2019**, *30* (21), 214004. <https://doi.org/10.1088/1361-6528/aaff96>.
- (221) Zullino, S.; Argenziano, M.; Ansari, S.; Ciprian, R.; Nasi, L.; Albertini, F.; Cavalli, R.; Guiot, C. Superparamagnetic Oxygen-Loaded Nanobubbles to Enhance Tumor Oxygenation during Hyperthermia. *Front. Pharmacol.* **2019**, *10*, 1001. <https://doi.org/10.3389/fphar.2019.01001>.



- (222) Khan, M. S.; Hwang, J.; Lee, K.; Choi, Y.; Kim, K.; Koo, H. J.; Hong, J. W.; Choi, J. Oxygen-Carrying Micro/Nanobubbles: Composition, Synthesis Techniques and Potential Prospects in Photo-Triggered Theranostics. *Molecules* **2018**, *23* (9). <https://doi.org/10.3390/molecules23092210>.
- (223) Ramaswamy, B.; Kulkarni, S. D.; Villar, P. S.; Smith, R. S.; Eberly, C.; Araneda, R. C.; Depireux, D. A.; Shapiro, B. Movement of Magnetic Nanoparticles in Brain Tissue: Mechanisms and Impact on Normal Neuronal Function. *Nanomedicine Nanotechnology, Biol. Med.* **2015**, *11* (7), 1821–1829. <https://doi.org/10.1016/j.nano.2015.06.003>.
- (224) Shamloo, A.; Pedram, M. Z.; Heidari, H.; Alasty, A. Computing the Blood Brain Barrier (BBB) Diffusion Coefficient: A Molecular Dynamics Approach. *J. Magn. Magn. Mater.* **2016**, *410*, 187–197. <https://doi.org/10.1016/j.jmmm.2016.03.030>.
- (225) KT, H.; S, D.; DI, S.; RJ, W.-R.; RW, S. Fate of Nanoparticles in the Central Nervous System after Intrathecal Injection in Healthy Mice. *Sci. Rep.* **2019**, *9* (1). <https://doi.org/10.1038/S41598-019-49028-W>.
- (226) Sandberg, D. I.; Rytting, M.; Zaky, W.; Kerr, M.; Ketonen, L.; Kundu, U.; Moore, B. D.; Yang, G.; Hou, P.; Sitton, C.; Cooper, L. J.; Gopalakrishnan, V.; Lee, D. A.; Thall, P. F.; Khatua, S. Methotrexate Administration Directly into the Fourth Ventricle in Children with Malignant Fourth Ventricular Brain Tumors: A Pilot Clinical Trial. *J. Neuro-Oncology* **2015**, *1251* **2015**, *125* (1), 133–141. <https://doi.org/10.1007/S11060-015-1878-Y>.
- (227) Soni, S.; Ruhela, R. K.; Medhi, B. Nanomedicine in Central Nervous System (CNS) Disorders: A Present and Future Prospective. *Adv. Pharm. Bull.* **2016**, *6* (3), 319–335. <https://doi.org/10.15171/apb.2016.044>.
- (228) Xu, J.; Jia, Z.; Knutson, M. D.; Leeuwenburgh, C. Impaired Iron Status in Aging Research. *Int. J. Mol. Sci.* **2012**, *13* (2), 2368–2386. <https://doi.org/10.3390/ijms13022368>.
- (229) Liu, J. L.; Fan, Y. G.; Yang, Z. S.; Wang, Z. Y.; Guo, C. Iron and Alzheimer's Disease: From Pathogenesis to Therapeutic Implications. *Front. Neurosci.* **2018**, *12* (SEP). <https://doi.org/10.3389/fnins.2018.00632>.
- (230) Youdim, M. B. H.; Ben-Shachar, D.; Riederer, P. The Possible Role of Iron in the Etiopathology of Parkinson's Disease. *Mov. Disord.* **1993**, *8* (1), 1–12. <https://doi.org/10.1002/mds.870080102>.
- (231) Kell, D. B. Iron Behaving Badly: Inappropriate Iron Chelation as a Major Contributor to the Aetiology of Vascular and Other Progressive Inflammatory and Degenerative Diseases. *BMC Med. Genomics* **2009**, *2* (1), 1–79. <https://doi.org/10.1186/1755-8794-2-2>.
- (232) GUTTERIDGE, J. M. C. Hydroxyl Radicals, Iron, Oxidative Stress, and Neurodegeneration. *Ann. N. Y. Acad. Sci.* **1994**, *738* (1), 201–213. <https://doi.org/10.1111/j.1749-6632.1994.tb21805.x>.
- (233) Hentze, M. W.; Muckenthaler, M. U.; Andrews, N. C. Balancing Acts: Molecular Control of Mammalian Iron Metabolism. *Cell* **2004**, *117* (3), 285–297.

- [https://doi.org/10.1016/S0092-8674\(04\)00343-5](https://doi.org/10.1016/S0092-8674(04)00343-5).
- (234) Sofic, E.; Riederer, P.; Heinsen, H.; Beckmann, H.; Reynolds, G. P.; Hebenstreit, G.; Youdim, M. B. H. Increased Iron (III) and Total Iron Content in Post Mortem Substantia Nigra of Parkinsonian Brain. *J. Neural Transm.* **1988**, *74* (3), 199–205. <https://doi.org/10.1007/BF01244786>.
- (235) Boddaert, N.; Sang, K. H. L. Q.; Rötig, A.; Leroy-Willig, A.; Gallet, S.; Brunelle, F.; Sidi, D.; Thalabard, J. C.; Munnich, A.; Cabantchik, Z. I. Selective Iron Chelation in Friedreich Ataxia: Biologic and Clinical Implications. *Blood* **2007**, *110* (1), 401–408. <https://doi.org/10.1182/blood-2006-12-065433>.
- (236) Guiot, C.; Zullino, S.; Priano, L.; Cavalli, R. The Physics of Drug-Delivery across the Blood-Brain Barrier. *Ther. Deliv.* **2016**, *7* (3), 153–156. <https://doi.org/10.4155/tde-2016-0001>.
- (237) D'Agata, F.; Ruffinatti, F. A.; Boschi, S.; Stura, I.; Rainero, I.; Abollino, O.; Cavalli, R.; Guiot, C. Magnetic Nanoparticles in the Central Nervous System: Targeting Principles, Applications and Safety Issues. *Molecules* **2018**, *23* (1), 1–25. <https://doi.org/10.3390/molecules23010009>.
- (238) Zullino, S.; Argenziano, M.; Ansari, S.; Ciprian, R.; Nasi, L.; Albertini, F.; Cavalli, R.; Guiot, C. Superparamagnetic Oxygen-Loaded Nanobubbles to Enhance Tumor Oxygenation during Hyperthermia. *Front. Pharmacol.* **2019**, *10*, 1001. <https://doi.org/10.3389/fphar.2019.01001>.
- (239) Huang, H. Y.; Liu, H. L.; Hsu, P. H.; Chiang, C. S.; Tsai, C. H.; Chi, H. S.; Chen, S. Y.; Chen, Y. Y. A Multitheragnostic Nanobubble System to Induce Blood-Brain Barrier Disruption with Magnetically Guided Focused Ultrasound. *Adv. Mater.* **2015**, *27* (4), 655–661. <https://doi.org/10.1002/adma.201403889>.
- (240) Sintov, A. C.; Velasco-Aguirre, C.; Gallardo-Toledo, E.; Araya, E.; Kogan, M. J. Metal Nanoparticles as Targeted Carriers Circumventing the Blood–Brain Barrier. *Int. Rev. Neurobiol.* **2016**, *130*, 199–227. <https://doi.org/10.1016/bs.irn.2016.06.007>.
- (241) Tam, V. H.; Sosa, C.; Liu, R.; Yao, N.; Priestley, R. D. Nanomedicine as a Non-Invasive Strategy for Drug Delivery across the Blood Brain Barrier. *Int. J. Pharm.* **2016**, *515* (1–2), 331–342. <https://doi.org/10.1016/j.ijpharm.2016.10.031>.
- (242) Yao, J.; Hsu, C.-H.; Li, Z.; Kim, T.; Hwang, L.-P.; Lin, Y.-C.; Lin, Y.-Y. Magnetic Resonance Nano-Theranostics for Glioblastoma Multiforme. *Curr. Pharm. Des.* **2015**, *21* (36), 5256–5266. <https://doi.org/10.2174/1381612821666150923103307>.
- (243) Chertok, B.; David, A. E.; Yang, V. C. Brain Tumor Targeting of Magnetic Nanoparticles for Potential Drug Delivery: Effect of Administration Route and Magnetic Field Topography. *J. Control. Release* **2011**, *155* (3), 393–399. <https://doi.org/10.1016/j.jconrel.2011.06.033>.
- (244) Leterme, G.; Guigou, C.; Oudot, A.; Collin, B.; Boudon, J.; Millot, N.; Geissler, A.; Belharet, K.; Bozorg Grayeli, A. Superparamagnetic Nanoparticle Delivery to the Cochlea Through Round Window by External Magnetic Field: Feasibility and Toxicity. *Surg. Innov.* **2019**, *26* (6), 646–655. <https://doi.org/10.1177/1553350619867217>.

- (245) Rossi, N. A. A.; Zou, Y.; Scott, M. D.; Kizhakkedathu, J. N. RAFT Synthesis of Acrylic Copolymers Containing Poly(Ethylene Glycol) and Dioxolane Functional Groups: Toward Well-Defined Aldehyde Containing Copolymers for Bioconjugation. *Macromolecules* **2008**, *41* (14), 5272–5282. <https://doi.org/10.1021/ma800606k>.
- (246) Karaagac, O.; Kockar, H. Effect of Synthesis Parameters on the Properties of Superparamagnetic Iron Oxide Nanoparticles. *J. Supercond. Nov. Magn.* **2012**, *25* (8), 2777–2781. <https://doi.org/10.1007/s10948-011-1264-8>.
- (247) Ficiarà, E.; Ansari, S. A.; Argenziano, M.; Cangemi, L.; Monge, C.; Cavalli, R.; D'Agata, F. Beyond Oncological Hyperthermia: Physically Drivable Magnetic Nanobubbles as Novel multipurpose Theranostic Carriers in the Central Nervous System. *Molecules* **2020**, *25* (9). <https://doi.org/10.3390/molecules25092104>.
- (248) Dhakar, N. K.; Caldera, F.; Bessone, F.; Cecone, C.; Rubin Pedrazzo, A.; Cavalli, R.; Dianzani, C.; Trotta, F. Evaluation of Solubility Enhancement, Antioxidant Activity, and Cytotoxicity Studies of Kynurenic Acid Loaded Cyclodextrin Nanosponge. *Carbohydr. Polym.* **2019**, *224* (August), 115168. <https://doi.org/10.1016/j.carbpol.2019.115168>.
- (249) Jayanti, S.; Moretti, R.; Tiribelli, C.; Gazzin, S. Bilirubin: A Promising Therapy for Parkinson's Disease. *Int. J. Mol. Sci.* **2021**, *22* (12). <https://doi.org/10.3390/ijms22126223>.

